Etude des propriétés structurelles locales des matériaux magnétorésistifs

Fabrizio Bardelli

UNIVERSITE GRENOBLE I - JOSEPH FOURIER

Thèse

pour obtenir le titre de

DOCTEUR de l'UNIVERSITE JOSEPH FOURIER

Spécialité Physique

preséntée et soutenue publiquement par

Fabrizio BARDELLI

Etude des propriétés structurelles locales des matériaux magnétorésistifs

Date de soutenance: 19 Décembre 2006

Composition du Jury:

Jean-René Regnard	Président
Alicia De Andrés	Rapporteur
Pierre Lagarde	Rapporteur
Francesco D'Acapito	Examinateur
Settimio Mobilio	Directeur de Thèse

Thèse préparée au sein du laboratoire: Gilda - CRG, Installation Européenne de Rayonnement Synchrotron -BP220 F-38043 Grenoble, France

Local structural properties of magnetoresistive materials

Fabrizio BARDELLI

PhD Thesis

December, 2006

University Joseph Fourier - Grenoble I

PHYSICS

Advisor : Prof. S.Mobilio

Laboratory : G.I.L.D.A - Collaboration Research Group
European Radiation of Synchrotron Facility

Contents

Introduction

L'objectif de cet étude est de donner une caractérisation complète de la structure locale de deux classes de composés : les manganites de lanthane droguées avec du sodium et les doubles perovskites de ferro-molybdène droguées avec du tungstène.
Les deux classes se comportent, en général comme de conducteurs dans leur phase ferromagnétique et, suivant variations de température ou de dopage, ils subissent une transition métal-isolant à laquelle il faut associer une transition ferromagnétique-paramagnétique(antiferromagnétique).
Ces matériaux sont devenus un défi pour les physiciens du état solide. Ils sont, en effet, le prototype de systèmes électroniques fortement mappés où les degrés de liberté du spin, charge orbitales et structurales jouent simultanément et où les exemplifications courantes, comme celle d'omettre les interactions électron-électron et électron-phonon, cessent d'être valides.
En particulier, les manganites sont utilisées depuis des années dans l'industrie des dispositifs magnétiques de stockage des donnés. Toutefois, le potentiel technologique de les deux classes, pourrait être pleinement exploité dans le champ émergent de la spintronique pour la réalisation de dispositifs électroniques basés sur le contrôle de l'orientation du spin des électrons.
Les manganites ont un diagramme de phases magnétiques et structurales incroyablement riche lié aux variations de paramètres macroscopiques tels la température, la pression et le dopage. Ils vont de phases ferromagnétique ou antiferromagnétique à phases paramagnétique mais ils arrivent aussi aux

plus exotiques phases d'ordre orbital et de charge.
La structure locale de film fins de manganite droguées avec du sodium a été étudiée en fonction de l'épaisseur des film. Les film fins offrent un système versatile et efficace pour accroître des nouvelles structures ; en effet, le stress induit par le substrat arrive à stabiliser les structures qui n'existent pas dans des conditions normales de pression et de température.
Les perovskites doubles ont des propriétés similaires aux manganites mais le mécanisme à la base du transport des charges est différent et il n'est pas encore complètement acquis. Il est fondé sur une strate fondamentale moitie-métallique et ferromagnétique complètement polarisé. Au contraire des manganites, la magnétorésistance reste élevée même au-dessus de la température ambiante (jusqu'à environ 450 K). Pour cette raison ils pourraient être des bonnes candidats pour des applications technologiques.
Des échantillons de poudre de perovskites double droguées avec tungstène ont été étudiées pour en caractériser la structure locale en fonction du dopage et pour chercher de comprendre la nature de la transition métal-isolant.
Une caractérisation complète de ces matériaux, en particulier du point de vue de la structure et de la microstructure, constitue un pas nécessaire pour la réalisation de dispositifs réels. En effet, il est tout à fait accepté que aussi bien dans les manganites, que dans les perovskites doubles, les propriétés de transport sont influencées d'une façon importante par la structure locale (longueur et angle de liaison) autour des sites clés occupés par des ions magnétiques. Pour cette raison la spectroscopie d'absorption de rayon X, en étant sensible à l'ordre locale autour de l'atome absorbeur, constitue la technique la plus adaptée pour l'étude de ces composés.
Lorsque il était possible mesurer les perovskites doubles en transmission, en mesurant le rapport entre l'intensité des rayon X incidente et celle transmit, pour les films fins nous avons du utiliser des méthodes indirectes comme la fluorescence ou les électrons (Total Electron Yield). Il a été nécessaire de

développer un détecteur d'électrons dont les caractéristiques devaient être les suivantes :

- la possibilité de travailler à des basses températures afin de pouvoir suivre l'évolution des propriétés structurales en fonction de la température et /ou limiter l'atténuation due à cette dernière.

- l'amplification du courant d'électron émis par les film les plus fins (50 Å). Ce résultat a été réalisé grâce au procédé de multiplication de charge des électrons Auger dans le gaz hélium.

- la capacité de réduire les pics de Bragg parasite qui proviennent du substrat cristallin non- dilué.

La réalisation de cet instrument s'est révélé un défi du point de vue technique et il a demandé une telle quantité de travail aussi bien sur la plan pratique que théorique qu'elle représente le troisième argument de cette thèse.
Les mesures d'absorption de rayon-X ont été effectuées à la ligne de lumière italienne pour la diffraction et l'absorption (GILDA-BM8) à l'Installation Européenne de Rayonnement de Synchrotron (ESRF) de Grenoble (France).
Les échantillons de poudre de perovskites double drogués avec du tungstène ont été préparés par le groupe du Professeur D.D. Sarma à l'Unité de Chimie Structurale et du état solide de Bangalore (Indie) qui fait partie de l'Institut de Science Indien.
Les film fins de manganite drogués avec du sodium ont été réalisés par le Professeur P. Ghigna à l'UFR de chimie de l'Université de Pavie (Italie).

La thèse comporte six chapitres. Les premier et le deuxième décrivent les aspects théoriques et expérimentaux respectivement sur les manganites et sur les perovskites doubles. Dans le premier chapitre j'a décrit les propriétés structurales et les théories qui ont été développes dans les dernières quatre

décades pour expliquer le mécanisme du transport de charges dans le manganites. Cette concepts seront utile même pour comprendre les propriétés du perovskites doubles décrits dan le chapitre deux). Le troisième chapitre illustre les techniques utilisées pour étudier la structure locale. Les derniers chapitres reportent les résultats des expériences dans les trois principaux domaines décrits plus haut : dans le quatrième chapitre nous pouvons trouver des détails sur la technique TEY et le travail effectué pour mettre en œuvre le détecteur. Les chapitres cinq et six sont consacrés aux résultats des mesures effectuées sur les films fins de manganite et sur les perovskites double et sur leurs interprétation.

Introduction

The aim of this work is to give an exhaustive characterization of the local structure for two class of compounds: sodium doped lanthanum manganites and tungsten doped iron-molybdenum double-perovskites.
Both class of materials usually behave as conductors in the ferromagnetic phase and undergo a metal-to-insulator transition, associated with a ferromagnetic-to-paramagnetic(antiferromagnetic) transition, upon varying the temperature or the doping level. They have been extensively studied in the last decades due to the huge magnetoresistive effect they exhibit.
These materials have become a challenge for solid state physicist since they are the prototype of highly correlated electronic systems, where spin, charge, orbitals and structural degrees of freedom simultaneously play together to determine the physical properties. Furthermore, usual simplifications, such as the neglect of the electron-electron and electron-phonon interactions, cease to be valid.
Manganites, are already used in magnetic storage devices technology and they are potentially useful as magnetic sensors. Nevertheless, the full potential of these classes of compounds may be exploited in future spin-driven electronic devices, in the emerging field of spintronic.
Manganites have an incredibly rich phase diagram as a function of macroscopic parameters such as temperature, pressure and of doping level. They span from ferromagnetic/antiferromagnetic to paramagnetic magnetic phases but also to more exotic charge and orbital ordered phases.

In this work, the local structure of Na-doped manganites in the form of thin films has been studied as a function of the film thickness. Thin films method offer a powerful and versatile technique for growing new structures; in fact, substrate-induced strain effects can stabilize structures which do not exist under classical conditions of pressure and temperature.

Double-perovskites have properties similar to manganites but the mechanism at the basis of charge mobility is different and still not fully understood. Contrary to manganites, magnetoresistance remain large well above room temperature. For this reason they could be even more promising candidates for technological applications.

Bulk samples of a tungsten doped iron-molybdenum double perovskite series have been investigated mainly to characterize the local structure as a function of the doping level and to understand better the nature of the metal-to-insulator transition.

A comprehensive characterization of these materials, in particular from the point of view of the structure and the microstructure, is a necessary stage for the realization of practical devices. It is widely accepted that in manganites, as well as in double-perovskites, transport properties are strongly influenced by the local structure (bond lengths and angles) around key sites, occupied by magnetic ions. For this reason the X-ray absorption spectroscopy (XAS), being sensitive to the local order around the absorber atom, is the more suitable technique to study such compounds.

While it was possible to study double-perovskites in the standard transmission geometry, i.e. measuring the ratio between the incident and the transmitted intensity of the X-ray beam, for thin films indirect methods, as fluorescence or total electron yield (TEY), had to be used. After preliminary measurements it became clear that best results can be achieved using TEY. Therefore it was necessary to develop a TEY detector with the following main requirements:

- the possibility to work at low temperatures, in order to measure structural properties as a function of the temperature and/or to limit the thermal damping of the signal.

- the amplification of the very low signal coming from very thin films (50 Å), which was achieved by charge-multiplication of the Auger electrons in helium gas.

- the ability to reduce parasitic Bragg peaks coming from the non-dilute substrate.

The realization of this equipment was challenging from a technical point of view and it required such an extensive theoretical and technical work that it became the third argument of my work.
X-ray absorption measurements were done at the Italian beam line for diffraction and absorption (GILDA-BM08) at the European Synchrotron Radiation Facility (ESRF) of Grenoble (France).
The W doped double-perovskite powder samples were prepared by the group of Prof. D.D. Sarma at the Solid State and Structural Chemistry Unit of Bangalore (India), which belongs to the Indian Institute of science. The same group performed X-ray diffraction, resistivity and magnetization measurements on the same samples.
The Na-doped manganite thin films were prepared by the group of Prof. P.Ghigna at the Department of Physical Chemistry of the University of Pavia (Italy), which performed also a characterization of the macroscopic (resistivity and magnetization), microscopic (lattice structure) and chemical properties of the samples using several techniques (X-ray diffraction, Electron Micro-Probe Analysis, Atomic Force Microscope).

The thesis is composed of six chapters. Chapter one and two describe theoretical and experimental issues about manganites and double-perovskites,

respectively. In the first chapter I will describe the structure and report the theories developed in the last four decades to explain the charge transport of manganites. These concepts will be useful to understand the properties of double perovskites. The third chapter illustrates the techniques used to investigate the local structure and the experimental apparatus. The remaining chapters report the results obtained on the three main issues referred above: chapter four describes more in detail the TEY technique and the work done to realize the detector. Chapter five and six report the experimental results on manganites thin films and double perovskites and their discussion.

Chapter 1

Manganites

The term "manganite" refers to compounds having general formula $A\mathrm{MnO}_3$ and perovskite unit cell (which I will describe in the following). A huge negative magnetoresitance effect, called "Colossal Magneto-Resistance" (CMR), was discovered in manganites during the fifties [33, 91]. The magnetoresistance (MR) is a variation of the resistivity occurring, in some type of compounds, due to the application of an external magnetic field or to the appearance particular magnetic ordering (usually ferromagnetism). As will be discussed in the following, the mechanism at the origin of the MR can be very different from one material to another. The MR is usually defined as:

$$MR = \frac{\rho(H) - \rho(H_0)}{\rho(H_0)} \tag{1.1}$$

where $\rho(H)$ is the resistivity in the presence of a magnetic field of strength H and $\rho(H_0)$ the zero field resistivity. The value of the MR is negative if the resistivity drops down after the application of a magnetic field (or after the appearance of a particular magnetic ordering in the compound).
Even if the first theories proposed to explain CMR were developed soon after its discover [93, 18, 2], a satisfactory quantitative theory has been developed only in the nineties [49] and the debate on these materials seems to be still

far from its end.

The magnetoresistance (MR) effect measured in manganites is much larger ($\sim 100\%$) then that usually observed in metals ($\sim 2 \div 5\%$). Even if very small, this effect is always present in materials with a large field mean free path, like high purity materials with a very regular crystal lattice. In such conditions, an external magnetic field forces the electrons to move in circular orbits reducing their mean free path.

Larger MR (Giant Magneto-Resistance, GMR), of the order of 15-20%, is observed in metallic multi-layers. In this case MR is due to the spin-valve effect that occurs between polarized metallic layers. An electron forced to pass through a polarized metallic layer will experience a spin-dependent scattering. If the electron is initially polarized parallel to the polarization of the layer, the scattering probability is reduced, while, it is instead enhanced for an antiparallel electron-layer polarization. In this contest, an external magnetic field reduces(enhances) the electron scattering, by aligning the polarization of the metallic layer parallel(antiparallel) to that of the charge carriers. In the case of metallic multi-layers the value of the MR can reach some tens of percent, with the advantage that the effect is not limited to low temperatures.

In manganites MR arises from the competition between different ground states: metallic and semiconductor. The great potentiality comes from the very large MR effect and from the fact that it occurs at temperatures near, or even above, room temperature. In the past, and again in recent years, both theoreticians and experimentalists have been involved in a enormous effort in order to understand in detail the properties of manganites. In spite of this effort a complete and satisfactory knowledge on these systems has not yet been achieved. Actually, these materials have became a challenge for solid state physicist since they are the prototype of highly correlated electronic systems where spin, charge, orbitals and structural degrees of freedom simul-

taneously play together and where usual simplifications, such as the neglect of the electron-electron and electron-phonon interactions, are no more valid.

1.1 First experiments

Extensive studies on manganites began in the fifties after that van Santen and Jonker [33] discovered an evident correlation between the Curie temperature (T_c), the saturation magnetization and the resistivity in the $La_{1-x}Ca_xMnO_3$ series. The results of their experiments can be summarized in the following points:

1. After studying the correlations between the crystal structure and the Curie temperature and finding that different samples with the same lattice constant had different Curie temperatures, they concluded that a picture of simple exchange interaction could not explain the ferromagnetic transition temperature in manganites. From a structural point of view, we now know that the relevant parameter in determining T_c is not the distance between manganese ions, but the very local structure around Mn sites and the angle of the Mn-O-Mn bond.

2. The $x = 0.3$ polycrystalline sample was found to have the maximum Curie temperature. The magnetization value for such composition corresponds to a complete polarization of the $3d$ electrons, while, the conductivity for the same composition is about 300 $\Omega^{-1}\text{cm}^{-1}$, confirming the conducting nature of the sample;

3. Alternate current resistivity measurements reported frequency dependence and a MR that decreased with the applied voltage. These results can be explained by supposing a phase inhomogeneity. Following this scenario, a model in which metallic grains are surrounded by high resistivity material has been proposed [52]. Today it is believed that

inhomogeneity is intrinsic to manganites and plays a very important role in their physics.

4. They found a linear relationship between the magnetoresistance and the magnetization of the samples, concluding that magnetism and electrical conductivity were definitively two correlated phenomena.

5. They established that both, divalent element content and oxygen stoichiometry, determined the Mn^{4+} ions content in the samples.

Soon after, in 1955 Wollan and Koehler ([91]) published a complete neutron diffraction analysis on the $La_{1-x}Ca_xMnO_3$ series, unrevealing the magnetic order of the end compounds and being able to draw a very first magnetic order *vs* composition phase diagram. Simultaneous theoretical efforts (Jonker and van Santen, 1950 [33]) were done in order to account for the rapidly growing amount of experimental results. Theoretical studies were oriented in the direction to link the structural and magnetic properties in the framework of a new (at that time) magnetic interaction mechanism proposed by Zener [93] in 1951: the Double-Exchange mechanism (DE). This model states that an electron can hop between two magnetic ions through an oxygen atom, promoting, at the same time, the alignment of the spins on these ions; further, the hopping of the electron itself is favored by the spin alignment on the magnetic sites, in a cooperative process. This mechanism simply connects transport with magnetic properties. Jonker also found a link between the lattice structure and the saturation magnetization: the more the structure is close to the ideal cubic perovskite, the more the saturation magnetization reaches its maximum theoretical value, corresponding to a complete polarization of the magnetic orbitals. He came to the conclusion that the cubic structure, having more collinear (180^o) Mn-O-Mn bonds, ensures a larger exchange interaction.

Starting from the above experimental results, theoretical models were de-

veloped supposing a highly spin polarized conduction band. Nevertheless, these first theories lacked to take into account an essential ingredient: the influence of the lattice on the transport properties (i.e. the electron-phonon interaction) in spite of clear experimental evidences. During the seventies, thanks to works made also on other compounds, such as EuO [62], the concept of charge localization by the means of magnetic, dielectric or lattice polarons has been developed. Other key works regarding charge localization were carried out by Mott and Davis (1971) [53] and by Tanaka et al. (1982) [87]. Tanaka proposed a model based on charge localization by means of small magnetic or lattice polarons, which become conductive in the paramagnetic phase (above T_c) through thermal activated hopping retrieving the experimental observed behavior for the resistivity ($\propto \exp[E_0/kT]$). Nevertheless, the mechanism that provokes the localization of the charge carriers, and hence the formation of polarons, still remained unknown.

The reason of the failure of these first models is that, in order to understand the physics underlying manganites, it is necessary to consider together all the experimental results and the theoretical studies. Fundamental ingredients to achieve a satisfactory knowledge of manganites are the Double-Exchange theory by Zener (1951) [93], Anderson and Hasegawa (1955) [2] and de Gennes (1960) [18]; the interpretation of the magnetic structure, first discovered by Wollan and Koehler [91], given by Goodenough (1955) [29]; the ideas on magnetic and dielectric polarons by Kasuya (1959) [34] and Mott and Davis (1971) [53]; the small polarons theory by Holstein (1959) [30]; the narrow band model by Kubo and Ohata (1972) [39]; the Jahn-Teller effect, first taken in account by Reinen (1971) [69] and finally introduced in the theory by Millis (1994) [49]. Also important are the theories on phase segregation and intrinsic inhomogeneity of manganites proposed by Moreo et al. (1999) [52] and, of course, a detailed knowledge of the long and short range structural order. In next paragraphs I will discuss the macroscopic properties of

manganites reporting, more in detail, most of the above ideas.

1.2 Crystal structure

Manganites of general chemical formula $A\mathrm{MnO}_3$, where A is a metallic di or tri-valent ion, have a perovskite-like structure (fig. 1.1) that belongs to the $Pm3m$ space group. The unitary cell is ideally cubic with a lattice parameter (Mn-Mn) of ~ 3.90 Å. Mn ions are placed at the vertexes of the perovskite cube and are surrounded by oxygen octahedra sharing their vertexes. The A ion (which can be La, Ca, Sr...) is at the center of the cubic cell. As expected for an ideal cubic structure the Mn-O-Mn bond angle is 180^o degree and the Mn-O bond length is half the lattice constant.

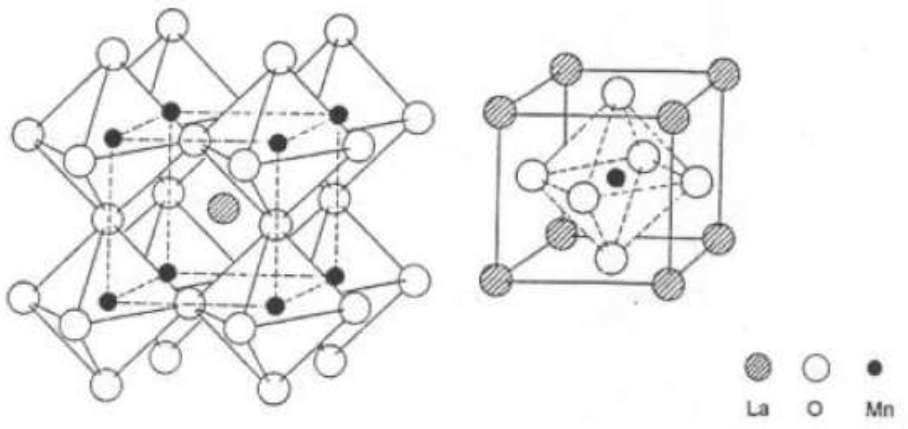

Figure 1.1: The ideal perovskite structure.

The actual perovskite structure differs from the ideal cubic structure due to a variety of different causes, resulting in a pseudocubic structure with different degrees of distortion. The most relevant causes are the size-mismatch and the Jahn-Teller effect.

The, so called, size-mismatch is due to the size of the central atom that is usually smaller than the free space available inside the cubic cell. We can

define a tolerance factor:

$$t = \frac{(r_{La,Ca} + r_O)}{\sqrt{2}(r_{Mn} + r_O)} \tag{1.2}$$

where r_i is the ionic radius of the i-th element. The value of t represents the entity of the distortion, being equal to 1 for the ideal structure. Since oxygen octahedra are stable structures, the system reduces the size-mismatch by tilting the octahedra with respect to the cell axis, rather than by changing the lattice parameter, as sketched in figure 1.2.

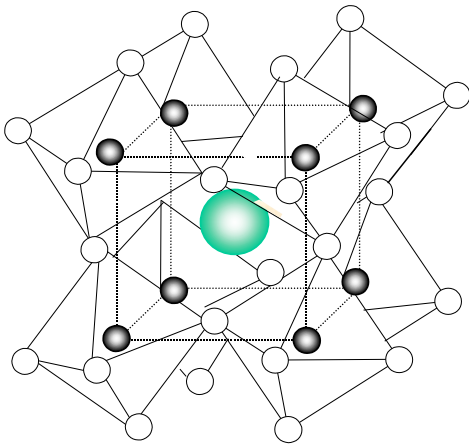

Figure 1.2: Different tilt configuration are possible for the oxygen octahedra. The one shown in the figure is the case in which the octahedra are tilted by the same angle alternatively clockwise and counterclockwise from one site to the other.

The Jahn-Teller effect is a common one for ions having partially filled and degenerate outer electronic states. In this case, a distortion of the local symmetry of the lattice, removes the degeneration so lowering the energy of the system. This is the case of the e_g and t_{2g} bands of the Mn^{3+} ion. These bands, which derive from the 3d orbitals in a cubic symmetry, are two and three-fold degenerate, respectively, and hence "unstable" in a perfect cubic geometry. The distortion of the octahedra splits the degenerate energy

levels by a quantity E_{JT}. Jahn-Teller distortion results in the elongation of the apical octahedra bonds with respect to the planar ones. The resulting distortion has an anisotropic character, as can be seen from the schematic sketch drawn in figure 1.3. On the other hand, since for Mn^{4+} the e_g band is empty, this effect does not acts on these ions, which, therefore, will not experience a JT-induced distortion of the lattice.

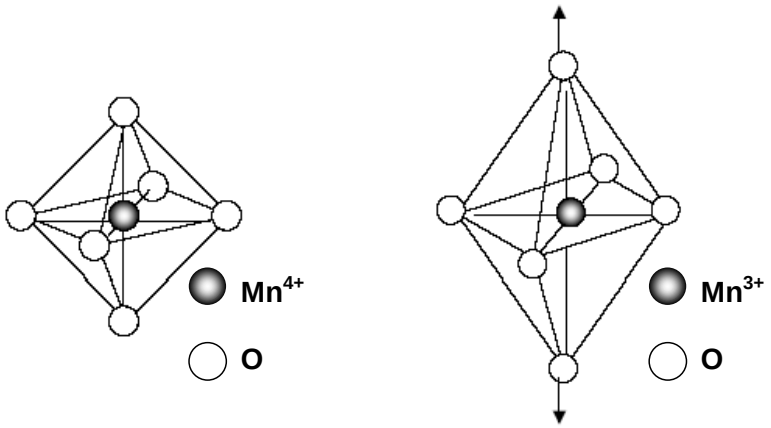

Figure 1.3: Figure shows how the JT effect acts on the oxygen octahedra: apical bonds are stretched up to ~ 2.15 Å, while, planar ones are splitted in 1.91 and 1.97 Å.

Because of these distortions, unitary cell changes from the ideal cubic cell to a less symmetric cells. Thus, depending of its symmetry, the system is more properly described by rhombohedral, orthorhombic or monoclinic cells.

1.2.1 Parent compounds

Since manganites have general chemical formula $A\mathrm{MnO_3}$, the valence state of the Mn ion, which can be 3+ or 4+, depends on wether the A cation is divalent or trivalent ($A^{3+/2+}$-$\mathrm{Mn}^{3+/4+}$-$\mathrm{O_3}^{2-}$). If the A cation is divalent (Ca, Sr, Ba, Pb...), the unitary cell is cubic (space group $Pm3m$), Mn ions have 4+ valence state and the Jahn-Teller distortion is not effective; therefore the structure is similar to the ideal cubic one described above with

the oxygen forming regular octahedra having six equal Mn-O distances (see table 1.1). On the contrary, if A is trivalent (generally chosen among the rare earths or La, Pr, Y...) Mn ions are in the 3+ valence state, that is, in the Jahn-Teller active configuration. The structure can be either orthorhombic, rhombohedral or monoclinic (*Pnma*, *R*-3*c*...). Oxygen octahedra experience a JT distortion, which results in reduced Mn-O-Mn bond angles ($\sim 155^o$). Diffraction and absorption data show that Mn-O bond distances splits from a unique distance of $\sim$ 1.95 Å for the regular octahedra, to $\sim$ 2.15 Å, $\sim$ 1.91 and $\sim$ 1.97 Å, for the apical bonds and planar distances of the distorted octahedra. The Mn-Mn bond length split in a length of 3.86 Å for the two Mn ions lying along the c axis (apical bonds) and of 3.97 Å for the orthogonal axes (planar bonds) (see table 1.1). Finally, the cell volume increases with respect to the Mn^{4+} compounds.

1.2.2 The solid solution $La_xA_{1-x}MnO_3$

Upon the substitution of the rare-earth trivalent central atom (A=La, Y, Pr) with a divalent alkaline-earth metal (B=Ca, Sr, Ba), we obtain the series of compounds $A_{1-x}B_xMnO_3$, whose end members are the $AMnO_3$ and $BMnO_3$ parent compounds:

$$\underset{0 \longrightarrow x}{LaMnO_3 \longrightarrow La_{1-x}Ca_xMnO_3} \underset{\longrightarrow 1}{\longrightarrow CaMnO_3}$$

where x represents the doping level. Accordingly to this substitution, an equal percentage of Mn^{3+} ions is formally replaced with Mn^{4+} , resulting in the injection of holes in the system. Thanks to the stability of the perovskite structure, it is possible to obtain a solid solution from one end member ($x = 0$) to the other ($x = 1$). In the intermediate members, due to the co-presence of divalent and trivalent central cations, Mn^{3+} and Mn^{4+} are

	^{a}LaMnO$_3$		^{b}LaMnO$_3$		CaMnO$_3$	
Atom pair	N	R(Å)	N	R(Å)	N	R(Å)
Mn-O	2	1.92	2	1.91	6	1.90
	2	1.97	2	1.97		
	2	2.15	2	2.17		
La/Ca-O	4	2.45	4	2.45	4	2.35
	4	2.70	4	2.67	4	2.57
	4	3.20	4	3.30	4	3.00
Mn-Ca/La	2	3.24	2	3.24	2	3.09
	4	3.39	4	3.38	4	3.23
	2	3.65	2	3.67	2	3.37
Mn-Mn	2	3.86	6	3.98	6	3.73
	4	3.97				

Table 1.1: Near-neighbor bond lengths (R) and coordination number (N) for LaMnO$_3$ and CaMnO$_3$ as given by diffraction studies. Data for individual bond lengths are averaged to account for the poorer resolution of XAFS data. The a sample is orthorhombic, while (b) is monoclinic sample.

simultaneously present (to ensure charge neutrality). As a consequence, the intermediate compounds, $A_{1-x}/B_x[\mathrm{Mn}^{3+}_{1-x}/\mathrm{Mn}^{4+}_x]\mathrm{O}_3$, have a mixed valence character. As will be discussed, this is a key feature in determining their macroscopic properties.

These specimens are also expected to have structural and transport properties intermediate between that of the parent compounds. At some doping level they are metallic and ferromagnetic at low temperatures and semiconducting and paramagnetic at high temperatures. Further, the metal-insulator transition (MIT) is associated to a transition of the magnetic ordering. Usually, the MIT temperature coincides with the Curie temperature T_c. Around T_c, a strong variation of the electrical resistivity, up to several orders of mag-

nitude, occurs upon application of a magnetic field of few Tesla. The lattice parameters and the volume of the unit cell of intermediate compounds usually display a sharp discontinuity at T_c, as evidenced by XRD (X-Ray diffraction) and NPD (Neutron powder diffraction) measurements.

The transport properties of these compounds can be successfully explained by introducing the concept of polaron that will be described in more detail in the last paragraphs of this chapter. Here we focus our attention on the relation between polarons and lattice structure.

Polarons in manganites have been interpreted as JT distortions associated with Mn^{3+} sites. In the simplest scenario, charge localization in the paramagnetic phase is due the formation of polarons, while, in the metallic phase, the enhanced charge mobility completely removes JT distortion. However, the real situation is somewhat more complex: the JT distortion is not fully removed in the metallic phase. This was interpreted [40] as due to a cross over from small (lower JT distortion) to large (higher distortion) polarons at the metal to insulator transition. In this regime complex phases could appear with the presence of both kind of polarons and segregation of microscopic phases into domains of itinerant large polarons and localized small polarons. By XAS measurements, Lanzara et al. [40] were able to quantify the polarons size drawing a picture in which the metallic state is characterized by homogeneously distributed large polarons (fig. 1.4, left panel), while the paramagnetic phase is characterized by the coexistence of small and large polarons (fig. 1.4, right panel). In this latter phase the size of the polarons is estimated to be equal to two Mn sites, while in the metallic phase it extends over four Mn sites.

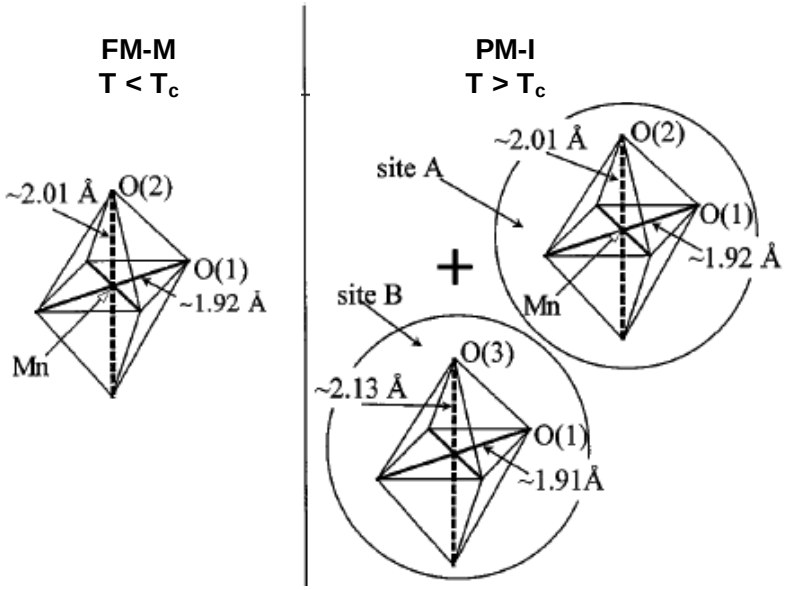

Figure 1.4: Pictorial view of the MnO_6 octahedral local distortions in the ferromagnetic metallic, FM-M (left panel), and paramagnetic insulating, PM-I (right panel) phase. (from [40])

1.3 Electronic structure

According to Hund's rule, the Mn atoms, which electronic configuration is [Ar] $3d^5 4s^2$, have the four 3d electrons with parallel spin, resulting in a non-zero magnetic moment. Due to the crystalline field originated by the surrounding oxygen octahedra, the 3d orbitals are splitted into two sublevels: the triple degenerate level, of symmetry t_{2g}, and the double degenerate level of symmetry e_g (see fig. 1.5). This situation stands for the Mn^{4+} ions, which do not experience Jahn-Teller (JT) effect. On the contrary, the JT induced distortion, acting on Mn^{3+} ions, further splits the energy levels removing the remaining degenerations, as reported in fig. 1.5.

In mixed valence compounds the average number of 3d electrons for manganese ion is $4 - x$, where x indicates the nominal occurrence of Mn^{4+} ions and $1 - x/$ the Mn^{3+} one. Three of these electrons fill up the t_{2g} levels, which

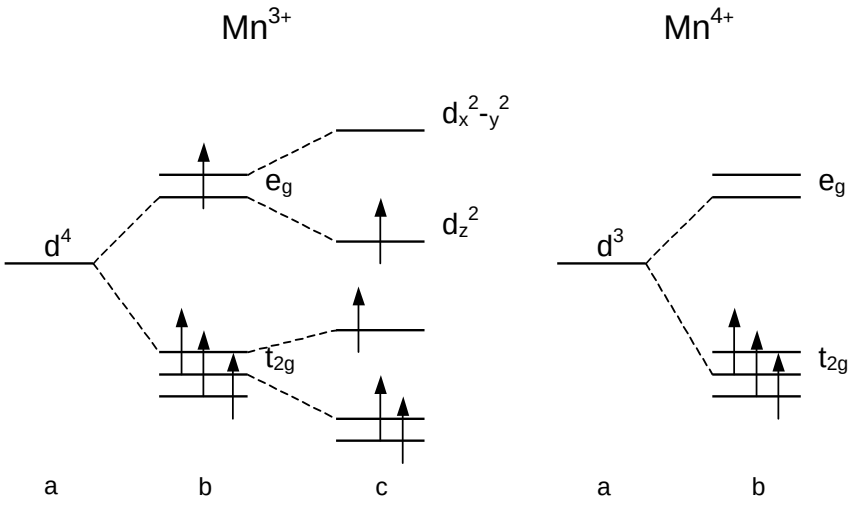

Figure 1.5: Left panel: a) $3d^4$ five-fold degenerate Mn^{3+} electronic levels; b) 3d levels splitting due to the crystal field; c) Further splitting due to the JT effect. Right panel: a) $3d^3$ Mn^{4+} levels; b) crystal field splitting of the 3d levels.

form a core having total spin state $S = 3/2$. The remaining $1 - x$ electrons occupy the e_g symmetry energy level (which has a bandwidth of ~ 2.5 eV). Due to the large Hund coupling strength, the spin of the e_g electrons is parallel to the spin of the t_{2g} core electrons.

In the Mn^{3+} -containing end compound ($LaMnO_3$), the Fermi level resides in the gap opened by the JT effect between the e_g sublevels, which contain only one, delocalized, electron. On the other hand, the Mn^{4+} containing-end compound have no electrons in the e_g levels. Both compounds are insulating, because they contain only trivalent or divalent Mn ions, corresponding to an entirely filled or a totally empty conduction band. On the contrary, intermediate (mixed-valence) compounds, which contain both Mn^{3+} and Mn^{4+} ions, have a partially filled e_g band (1.6) and, therefore, are conductive. As we will see, it is the hopping of the e_g electrons from a Mn^{3+} site to a Mn^{4+} one that gives rise to the conduction promoting, at the mean time, the ferromagnetic coupling of the Mn ions.

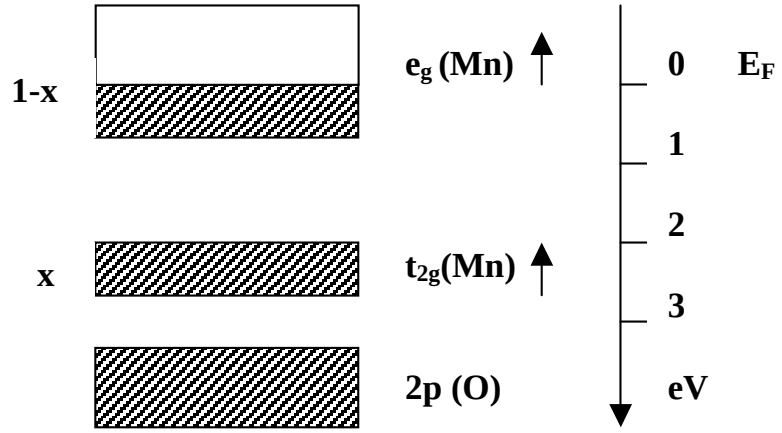

Figure 1.6: Schematic band structure of the intermediate compounds. x correspond to the concentration of Mn^{4+}/Ca^{2+} ions.

1.4 Magnetic structures

The first complete phase diagram on manganites have been obtained by Wollan and Koheler, on the $La_{1-x}Ca_xMnO_3$ solid solution, by neutron diffraction measurements (fig. 1.7). Later on, Goodenough theoretically reproduced the experimental phase diagram for a general manganite ($A_xB_{1-x}MnO_3$) following simple rules based on considerations on the chemical bonds and on their relation with the magnetic properties. He postulated the presence of a strong hybridization of the manganese d orbitals with the oxygen p ones, in contrast to the ionic model, which was prevailing at that time and that presumes atomic-like orbitals. Depending on the relative orbital orientation of adjacent ions, different bonds configurations can occur. Figure 1.8 shows the possible Mn-O-Mn bond configurations together with the associated magnetic order and resistivity.

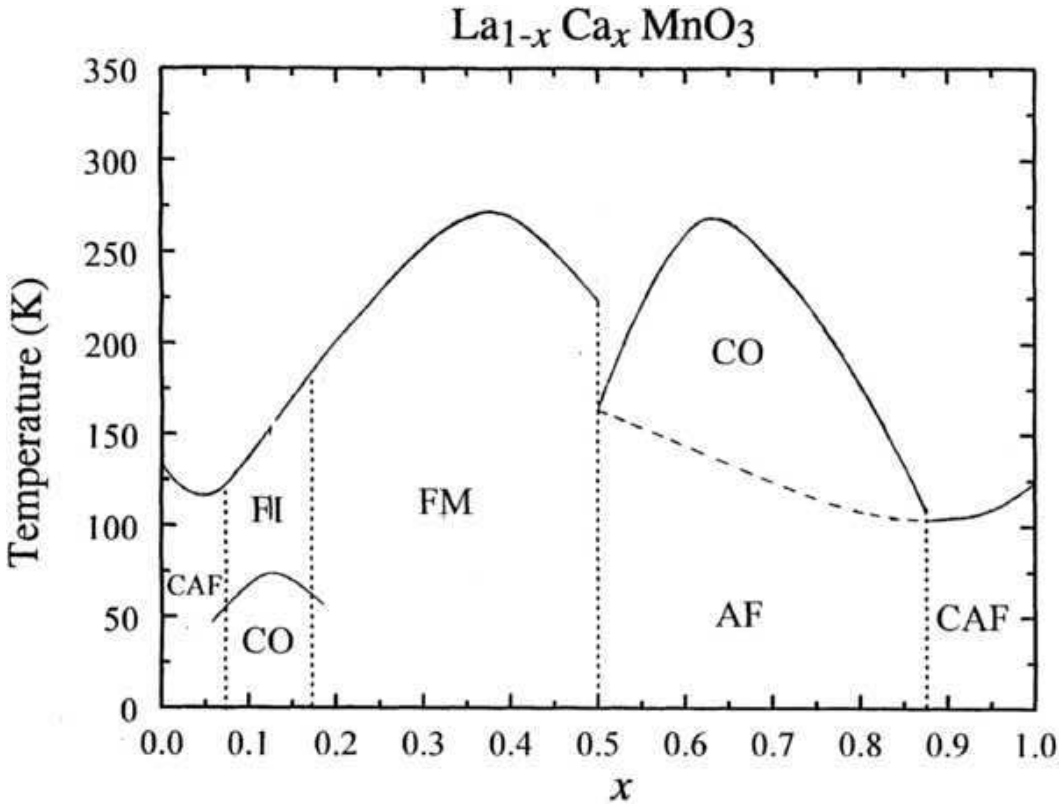

Figure 1.7: Magnetic phase diagram of the $La_{1-x}Ca_xMnO_3$ series as a function of composition and temperature. It is evident the richness of different magnetic arrangement and transport properties upon varying the composition and the temperature: CO = charge ordered, CAF = canted antiferromagnetic, FI = Ferromagnetic insulator, FM = ferromagnetic-metallic, AF = antiferromagnetic.

Case four, reported in figure 1.8, corresponds to the Double-Exchange bond type, which is typical of manganites. As will be discussed in the following, this bond type is at the origin of the conductivity in manganites. Table 1.4 and figure 1.9 report the magnetic arrangements and the transport properties, predicted by Goodenough [29], as a function of the composition x, together with the correspondent magnetic structures. The magnetic structures, originally labeled A, C, G and CE by Wollan and Koheler [91], are reported in figures 1.10, 1.11, 1.12 and 1.13 below. From table 1.4 and figures

Case	Mn-Mn separation	Transition temperatures	Resistivity	Schematic electron-spin configurations
Ordered lattices				
1	Smallest	$T_0 > T_c$	High	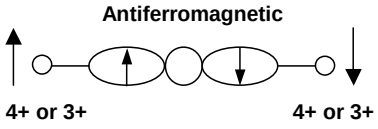
2	Large	$T_0 > T_c$	High	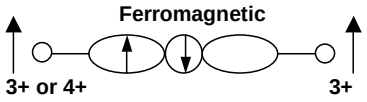
3	Largest	$T_c \approx 0$	High	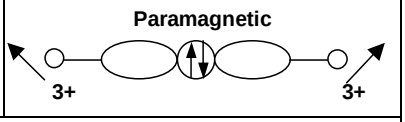
Disordered lattices				
4	Small	$T_0 = T_c$	Low	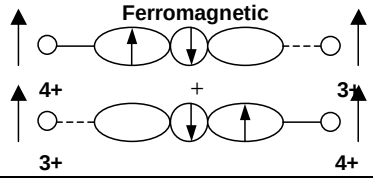

Figure 1.8: Possible Mn-O-Mn bond configurations together with the associated magnetic order and resistivity. T_0 and T_c are the bond ordering and magnetic ordering transition temperatures, respectively.

1.9 and 1.8, it can be deduced that low electrical resistivity accompanies the Double-Exchange phenomenon, while, high electrical resistivity is associated with other exchange mechanisms, even if there is ferromagnetic coupling of manganese magnetic moments.

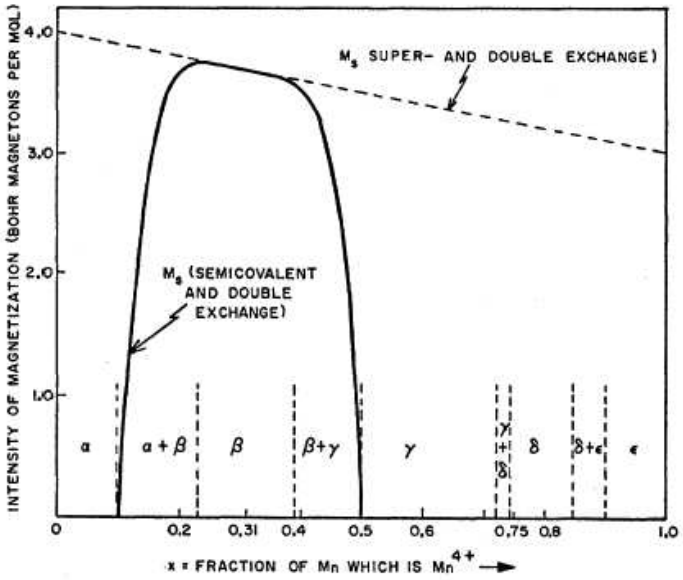

Figure 1.9: Predicted intensity magnetization and phase diagram for a generic system LaBMnO$_3$ according to Goodenough (from [29]).

1.5 Early transport theories

As already pointed out, manganites initially drawn researcher's attention because of the large magnetoresistance effect (CMR) that occurs in the range $0.2 < x < 0.5$ in the $La_{1-x}Ca_xMnO_3$ series (figure 1.14). At both end of the compositional range, manganites behave like antiferromagnetic insula-

x range	Type	Transport	Magnetic order
$0 \leq x \leq 0.1$	α	insulating	A-type antiferromagnetic
$0.2 \leq x \leq 0.4$	β	conducting	ferromagnetic
$0.5 \leq x \leq 0.75$	δ	insulating	CE-type antiferromagnetic
$0.75 \leq x \leq 0.85$	γ	insulating	C-type antiferromagnetic
$0.9 \leq x \leq 1.0$	ε	insulating	G-type antiferromagnetic

Table 1.2: Magnetic structures and macroscopic properties as a function of the doping x. (from [29])

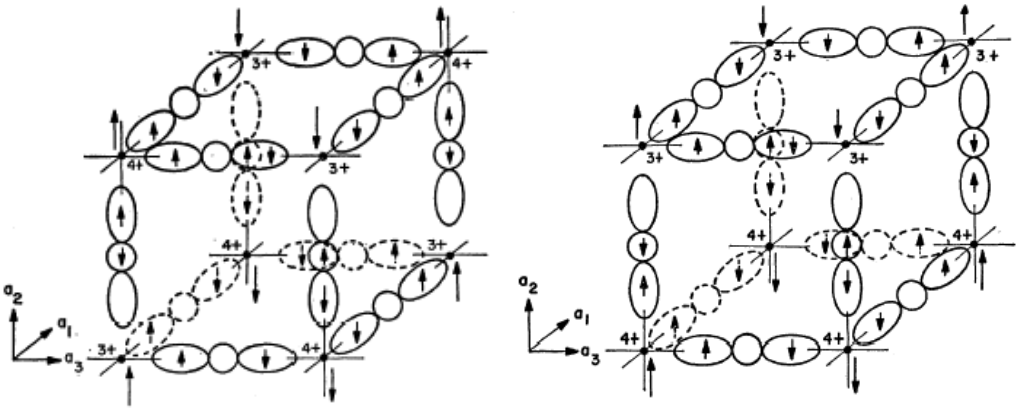

Figure 1.10: Type C has two possible magnetic structures, (a) and (b), having a slightly different energy.

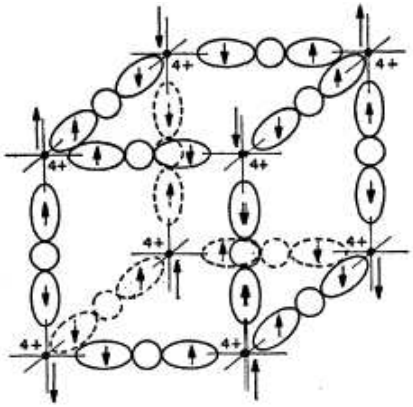

Figure 1.11: Magnetic lattice type G $(x = 1)$.

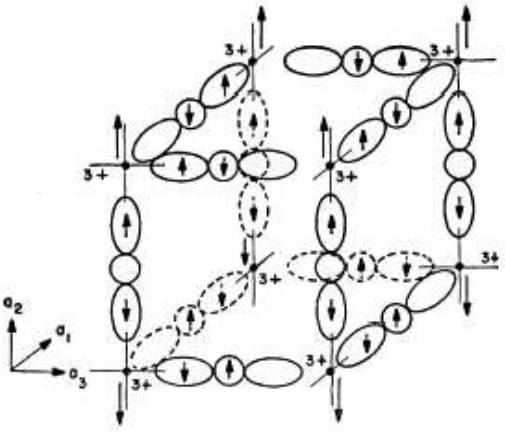

Figure 1.12: Magnetic lattice type A $(x = 0)$.

tors, whereas, upon substitution of only 10% of calcium in pure $LaMnO_3$ end compound, the room temperature conductivity is increased by two orders of magnitude. This indicates that the 10% extra holes, which have been added, are free to move from one Mn ion to another and are able to carry a current. These carriers have also effect on the magnetic properties: at low temperatures there is a non-zero spontaneous magnetization indicating that some sort of ferromagnetic coupling is present. Since Mn^{3+} ions are suffi-

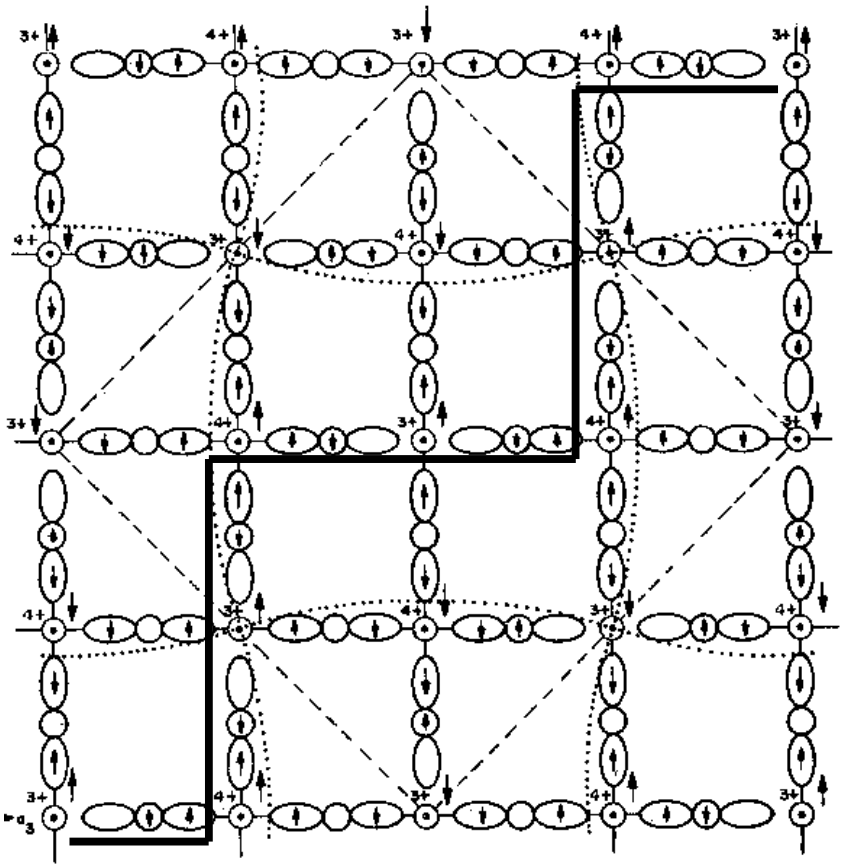

Figure 1.13: Magnetic lattice for $x = 0.5$; type CE. Successive [100] planes are alternatively parallel and antiparallel to this plane with identical bond configurations. Row of Mn ions along a_2 axis are alternatively all Mn^{3+} and all Mn^{4+} with $Mn - O - Mn$ bonds corresponding to case 1 of table 1.8. This magnetic arrangement has a lower energy than that of the two possible C type arrangements. Dotted lines underline the cooperative ions displacement from their equilibrium position in the lattice. Continuous and dashed lines put in evidence the ferromagnetic chains.

ciently far apart to have an appreciable overlapping of their wave functions, Zener explained ferromagnetism as due to an indirect coupling of incomplete d-shells via the conducting electrons.

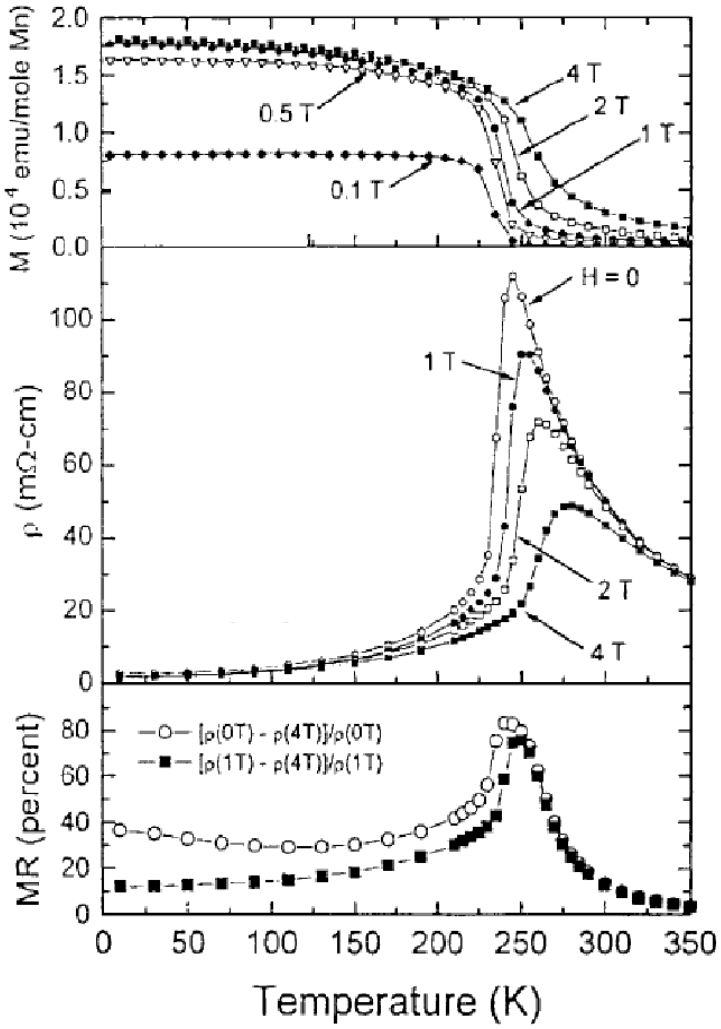

Figure 1.14: Magnetization (M), resistivity (ρ), and magnetoresistance (MR), as a function of temperature and external applied magnetic field for the $x = 0.25$ compound.

1.5.1 The Double-Exchange model

Zener proposed the Double-Exchange model to account for two phenomena experimentally observed by Jonker and van Santen:

1. The ferromagnetic to paramagnetic (FM-PM) transition is associated with a metal to insulator (M-I) transition.

2. The application of an external magnetic field, near the transition temperature, induces a large decrease of the resistivity.

In Zener's model, the electronic transport is ensured by the transfer of the charge carriers between Mn^{3+} and Mn^{4+} cations through the O^{2-} anion (fig. 1.15). Two antagonist mechanism come into play: the ferromagnetic (FM) ordering, which favors the hopping of the charge carriers, and the thermal disorder which destroys the FM order and is responsible for the FM-PM transition. On the other hand, the application of an external magnetic field, which promotes FM order, favors the metallic behavior even at temperatures higher than the Curie temperature. As already discussed, in Mn^{3+} t_{2g} electrons form a polarized core with a spin value of $S = 3/2$, while the $S = 1/2$, e_g, outer electrons are delocalized. Since the magnetic ions (Mn) wave functions do not overlap, direct exchange interaction, which would give rise to AFM coupling, is inhibited. Zener made three fundamental assumptions:

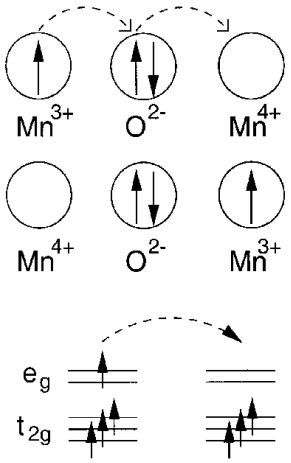

Figure 1.15: Schematic representation of the double exchange model. An electron (dashed line) hops from the Mn^{3+} to the Mn^{4+} ion so that the two ions change valence. The electron also carries with it-self the information on the magnetic state of the host site. Further, the hopping of the electron is favored in the case the manganese ions have parallel core spin.

1. intra-atomic exchange is so strong that the only relevant electronic configurations of carriers are those with spin parallel to the local ionic core spin;

2. the carriers do not change their spin orientation when moving. This means that they can hop from one ion to the next, *only* if the spins of the two ions are parallel;

3. when hopping is allowed, the ground state energy is lowered because the carriers participate in the binding.

This indirect coupling via conduction electrons will therefore lower the energy of the system when the spins of the d-shells are all parallel. This mechanism is basically different from the usual (direct or indirect) exchange. Direct coupling between incomplete d-shells always tend to align their spins in an antiparallel manner. Moreover the coupling is shared between the carriers and cannot be written as a sum of terms relating the ionic spins.
I will now expose more in detail the model proposed by Zener in its original form.
In doped manganites oxides, the two configurations:

$$1) \quad Mn^{3+}\, O^{2-}\, Mn^{4+} \;\rightarrow\; (\psi_1) \tag{1.3}$$

$$2) \quad Mn^{4+}\, O^{2-}\, Mn^{3+} \;\rightarrow\; (\psi_2) \tag{1.4}$$

are degenerate and are connected by so-called double-exchange matrix. More exact wave functions are given by the linear combinations:

$$\psi_{\pm} = N_{\pm}(\psi_1 \pm \psi_2) \tag{1.5}$$

If we denote the energy difference of these linear combinations by 2ε, by considering the time evolution of one of the two linear combination, we have:

$$\begin{aligned} \psi_+(t) &= exp^{-iE_2t/\hbar}\psi_1(0) + exp^{-iE_1t/\hbar}\psi_2(0) = \\ &= exp^{-iE_2t/\hbar}[\psi_1(0) + \ exp^{i2\varepsilon t/\hbar}\psi_2(0)] \end{aligned} \tag{1.6}$$

where E_1 and E_2 are the energies associated to the autostates ψ_1 and ψ_2 and $E_2 - E_1 = 2\varepsilon$. When T= $\pi/2\varepsilon$, ψ_+ reverts to ψ_-. Thus, the conduction electron will resonate the frequency:

$$\omega = 2\varepsilon/\hbar \tag{1.7}$$

between the states ψ_1 and ψ_2. The exchange energy ε is given explicitly by the integral:

$$J = \int \overline{\psi_1}(H - E_0)\psi_2 d\tau \tag{1.8}$$

The wave functions ψ_1 and ψ_2 can be written as:

$$\psi_1 = (\psi_d^1\psi_p)$$

$$\psi_2 = (\psi_d^2\psi_p)$$

where ψ_d represents the Mn 3d electronic wave function and ψ_p the wave function relative to the 2p oxygen orbital. The exchange integral then become:

$$J = \int \overline{\psi_d^1\psi_p}(H - E_0)\psi_d^2\psi_p d\tau \tag{1.9}$$

This matrix element describes the transfer of an electron from Mn^{3+} to the central O^{2-} and the *simultaneous* transfer from O^{2-} to Mn^{4+} (from here, the name double-exchange, DE). Zener underlines how this mechanism differs from the usual super-exchange due to the intrinsic degeneration of the states ψ^1 and ψ^2, while, in super-exchange the degenerate states are only

the excited ones. The coupling of degenerate states removes the degeneracy and the system resonates between ψ^1 and ψ^2 leading to a conducting ferromagnetic ground state. Because of the strong intra-atomic Hund coupling, the exchange integral has a non-negligible value only when the core magnetic moments of the Mn ions, between which the electron hops, are ferromagnetically aligned (parallel). On the contrary, when the Mn ions are not ferromagnetically ordered, certain energy is necessary to rotate the spin of the e_g mobile electron in order to align its spin with the Mn ion it is hopping to. The same mechanism that leads to electrical conduction also provide a coupling that leads to ferromagnetism. DE occurs only when spins of Mn ions points in the same direction and, since a stationary state is represented by one of the two linear combinations 1.5, depending upon the sign of the exchange integral 1.9, the DE raises the energy associated with ψ^1 and lowers that associated with ψ^2 or viceversa. Thus, the energy of one of these two stationary states is lowered by the DE. At low temperatures, regardless of the sign of the exchange integral, the energy of the system will be lowered by a parallel alignment of the spins, i.e., by FM.
Summarizing, the electronic transfer is favored by the FM arrangement, which is itself favored by the electronic transfer in a cooperative fashion.

Zener also established a quantitative relation between electrical conductivity and ferromagnetism. The magnitude of the exchange energy, ε, determines, through equation 1.7, the rate at which an electron jumps from a Mn^{3+} ion to an adjacent Mn^{4+} across a O^{2-} ion. We can define the diffusion coefficient of the Mn^{4+} ion by:

$$D = \frac{a^2 \varepsilon}{h} \tag{1.10}$$

where a is the lattice parameter. From the Einstein relation, $\sigma = ne^2 D/kT$, between the electrical conductivity, σ, the diffusion coefficient, D, and the

number of Mn^{4+} ions per unit volume n, we obtain:

$$\sigma = \frac{xe^2\varepsilon}{ahkT} \tag{1.11}$$

Here x is the fraction of the Mn ions with 4+ charge. The Curie temperature, T_c, is given approximately by $kT_c \sim \varepsilon$. On elimination of the unknown exchange energy ε between equations 1.10 and 1.11 we obtain:

$$\sigma = \frac{(xe^2/ah)}{(T/T_c)} \tag{1.12}$$

which is the relation between conductivity and ferromagnetism that we was searching for. These simple relations provided a qualitative description of the data then available.

Later on, Anderson and Hasegawa revisited Zener's argument, treating the core spin of each Mn ion classically and the mobile electron quantum mechanically. Designating the intra-atomic (Hund's) exchange energy by J and the transfer matrix element by b, Anderson and Hasegawa found that Zener's levels splitting is proportional to $\cos(\theta/2)$, where θ is the classical angle between the core spins. In their model, the effective transfer integral becomes:

$$t_{eff} = b\,cos\left(\frac{\theta}{2}\right) \tag{1.13}$$

The energy is lower when the itinerant electron's spin is parallel to the total spin of the Mn cores.

In 1960, de Gennes [18] anticipates current research by considering self-trapping of a carrier by distortion of the spin lattice, an entity we would now refer to as a magnetic polaron. He demonstrates that at small values of x, local distortions of the antiferromagnetic structure always tend to trap the doped-in charge carrier.

In 1972, Kubo and Ohata [39] considered a fully quantum mechanical version of a double exchange magnet. They introduced the now standard Hamiltonian:

$$H = -J \sum_{i,\sigma,\sigma'} (\vec{S}_i \cdot \sigma_{\sigma,\sigma'}) c^+_{i,\sigma} c_{i,\sigma'} + \sum_{i,j,\sigma} t_{ij} c^+_{i,\sigma} c_{j,\sigma} \tag{1.14}$$

where $c^+_{i\sigma}$, and $c^-_{i\sigma}$ are creation and annihilation operators for an e_g electron with spin σ on a Mn site and t_{ij} is the transfer-matrix element. The spin due to t_{2g} electrons is S_i; σ is the Pauli matrix, and J is the intra-atomic exchange energy, typically referred to as the Hund's exchange energy.

1.6 More recent transport theories

Double-Exchange mechanism alone is not able to predict quantitatively neither the value of T_c, which is much higher than the measured one, nor the value and temperature dependence of the electrical resistivity above T_c, where charge localization is surely present. The nature of the charge-carrier localization mechanism is a crucial issue in the physics of these materials. Among the possible mechanisms for charge localization, lattice distortions due to the different ionic radii of Mn^{3+} and Mn^{4+} and to the tendency of Mn^{3+} to assume a Jahn-Teller distorted configuration have received a considerable attention.

In 1994 Millis and collaborators [49] showed for the first time that early models fail to describe manganites on quantitative basis. They introduced in the transport theory of the concept of charge localization by the means of electric or magnetic fields. The idea of self-trapped charge carrier was introduced for the first time by Landau in 1933 to explain the properties of alkaline metals. He considered the possibility that free charges could localize in potential wells produced by ions displaced from their equilibrium position. Charges can be excited out from the potential well they are trapped,

by photo-absorption or by thermal effects. Once free, they can hop from one site to another and the medium becomes conductive. In strong polar solids, due to Coulomb interaction, an unbalanced charge is accompanied in its motion by the polarization of the surrounding lattice. Crystal physical properties can be described by considering the quasi-particle formed by the charge itself, plus the "cloud" of virtual phonons surrounding it. Such an entity is today called "polaron". Thus, a polaron is formed by a charge carrier and the local distortion it induces in the surrounding lattice. This distortion has both electrostatic and magnetic origin and is usually accompanied by a cooperative strain of the lattice. Materials that can stabilize polarons have a peculiar conductivity behavior due to the effective mass of the polarons, which is higher than electrons. This behavior is more evident at high temperatures as will be described in the following. As a matter of fact, in early experimental studies of manganites, high-temperature transport properties were believed to be dominated by non-intrinsic effects, like defects, crystalline disorder, grain boundaries, and impurities. Years later, with the preparation of good quality films by laser ablation on lattice-matched substrates and the growth of large single crystals, it became evident that the observed behavior is intrinsic and due to localization of charge carriers in polarons.

1.6.1 The role of the crystal lattice

In manganites, the localization is a consequence of a large electron-phonon interaction, enhanced by the Jahn-Teller activity of Mn^{3+}, and has an impact on the electric and thermal transport properties as well as on the lattice properties. The work of Millis and collaborators starts from the quantum version of the Double-Exchange (DE) Hamiltonian as formulated by Kubo and Ohata, to which, the electron-phonon interaction is added. The complete Hamiltonian that have been considered by Millis is:

$$H = H_{el} + H_{de} + H_{JT} + H_{ph} \tag{1.15}$$

where:

H_{el} describes the electronic transfer:

$$H_{el} = - \sum_{\langle ij \rangle, a, b, \alpha} t_{ij}^{ab} \, c_{ja\alpha}^{+} c_{ja\alpha} \tag{1.16}$$

i and j indicate the sites between which the electron hops; α and β represents the spins of the a and b orbitals; t_{ij} is the transfer matrix element (t_{eff}); c and c^{+} are the destruction and creation operators for a single electron.

H_{DE} is the double exchange Hamiltonian for the itinerant electrons:

$$H_{DE} = -J_H \sum_{i, a, b, \alpha, \beta} \vec{S}_c^{i} \cdot c_{ia\alpha}^{+} \vec{\sigma}_{\alpha\beta} \, c_{i\alpha\beta} \tag{1.17}$$

S_{ci} is the core spin of site i that is coupled to the itinerant electron through the Hund strength J_H; $\sigma_{\alpha\beta}$ are the Pauli matrixes that describes the spin of the itinerant electron.

H_{JT} represents the electron-phonon interaction:

$$H_{JT} = g \sum_{i, a, b, \alpha} \vec{r}_i \cdot d_{i,a,\alpha}^{+} \vec{\tau}_{ab} \, d_{ib\alpha} \tag{1.18}$$

where g is the electron-phonon coupling constant; $\overrightarrow{r_i}$ the vector that parameterize the distortion and t_{ab} the Pauli matrixes in the orbital space.

and H_{ph} describes the independent lattice vibrations (phonons):

$$H_{ph} = \frac{1}{2} \sum_{i} K r_i^2 \tag{1.19}$$

where K is the elastic constant of the harmonic oscillators. The hamiltonian is solved under the assumption of large magnetic coupling between the core spin and the itinerant electron ($S \times J_H \rightarrow \infty$). The competition between mobility and localization of the charge is quantified by the adimensional

parameter: $\lambda = E_{loc}/t_{eff}$ which represents the ratio between the energy due to the electron-phonon coupling (E_{loc}) and the transfer integral that determines the electronic mobility.
Three behaviors are distinguished by Millis below the Curie temperature:

- weak coupling, $\lambda << 1$: there is little lattice distortion even at low temperature and, as in metals, the resistivity $\rho(T)$ grows linearly by lowering the temperature;

- intermediate coupling $\lambda \sim 1$: there is a finite distortion even at $T = 0$ but the amplitude of the distortion is not sufficient to localize carriers having near the Fermi level. The resistivity grows on lowering the temperature but, differently from metals, doesn't tend to infinite when reaching $T = 0$;

- strong coupling, $\lambda >> 1$: here the distortion of the lattice due to the polarons formation is strong enough to open a gap in the spectral function. This induces an insulating behavior: the resistivity becomes infinite when the temperature approaches zero.

This model, which include electron-phonon coupling, is in better agreement with the experimental results as can be seen in figure 1.16.
To reach a better accord with the experimental data, more ingredients necessary. Some of these are: the on-site Coulombian interaction that enhances the localization of the carriers due the strong Hund coupling; the, so-called, "breathing mode" distortion of the oxygen octahedra, which, differently from the Jahn-Teller effect, acts on the planar bonds: the phonon and spin quantum fluctuations and the phonon correlations between adjacent Jahn-Teller distorted sites.

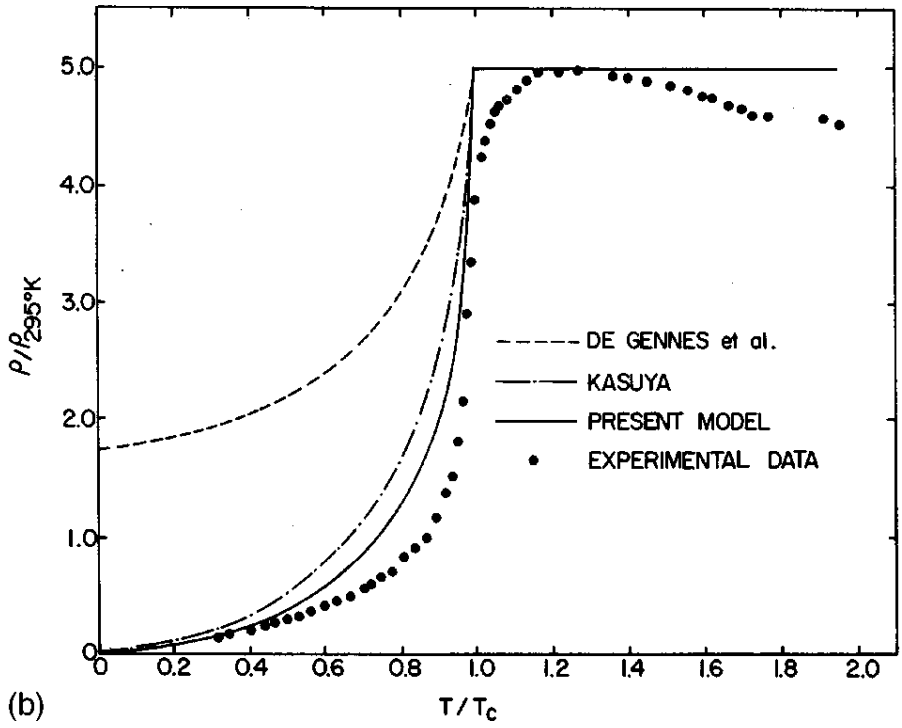

Figure 1.16: Comparison between simple DE models, DE+electron-phonon models and recent experimental data (from [34]).

1.6.2 Magnetic polarons

In 1960, Paul de Gennes considered the possibility that in magnetic materials the effect of charge localization is originated not only by the electron-phonon coupling (dielectric polarons) but also by magnetic polarons: a localized charge whose magnetic moment polarizes the surrounding ions spins as sketched in fig. 1.17.

A charge carrier moves through a crystal interacting with the magnetic moments of the lattice ions. This interaction has usually a ferromagnetic character, because the energy of the system is reduced by a parallel orientation of the spins. In 1979, Mott and Davis described this phenomenon quantitatively. They considered the Hund coupling between the conduction electron

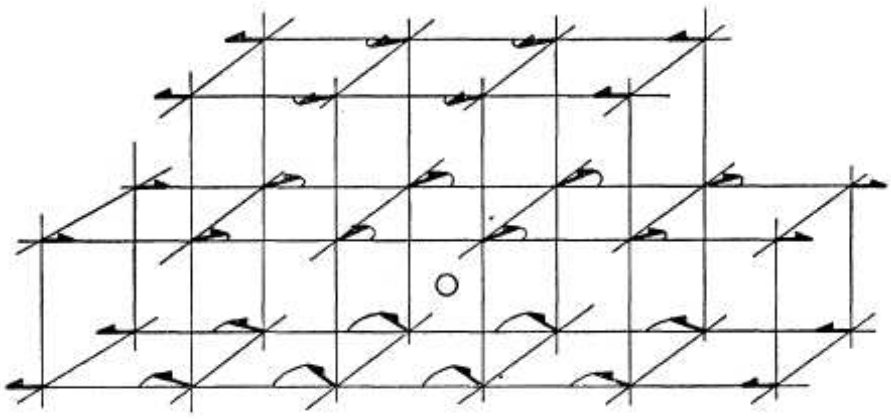

Figure 1.17: Local spin distortion in $LaMnO_3$. The bound hole is localized on eight Mn atoms (black circles) around the impurity center Ca^{2+} (open circle). Deflections are maximum close to impurity center and decrease slowly with distance. (from De Gennes [18])

and the on-site spin, J_H, and the interaction between spins of ions in different sites, J_s. They considered the case $J_H >> J_s$, as occurring in manganites. The charge localized in a region of radius r_p, polarizes the surrounding magnetic moments. The kinetic energy is thus:

$$E_c = \frac{\hbar^2 \pi^2}{2m^* r_p^2} \tag{1.20}$$

while the total energy of the charge, plus the ferromagnetic cluster it induces, is:

$$E_{tot} = \frac{\hbar^2 \pi^2}{2m^* r_p^2} + \frac{4\,\pi\, r_p^3\, J_s}{3a^3} - J_H \tag{1.21}$$

where the second term represents the energy required to brake an antiferromagnetic interaction and $-J_H$ the energy gained through the alignment of the spins of the ions with the conduction electron one. Minimizing with respect the radius r_p we obtain:

$$r_p^5 = \frac{\hbar^2 \pi\, a^3}{4m^*\, J_H} \tag{1.22}$$

and the total energy can be written as:

$$E = \frac{5\hbar^2\pi^2}{6m^*}\left(\frac{4m^*\,J_H}{\hbar^2\pi\,a^3}\right)^{2/5} - J_s \tag{1.23}$$

The magnetic polaron is only stabilized for a negative total energy. This condition is easily achieved in manganites, where $J_H >> J_s$.

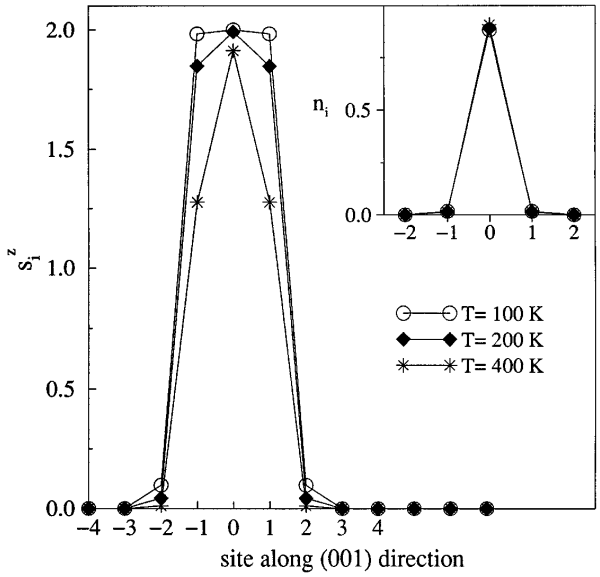

Figure 1.18: Distribution of the magnetization induced by a magnetic polaron on the surrounding lattice as a function of lattice site number for different temperatures. The inset shows the charge distribution.

However, polarons in manganites are believed to be mainly JT polarons, that is, dielectric polarons carrying with themselves the characteristic uniaxial JT distortion.

1.6.3 Polaronic transport properties

At high-temperature regime, magnetic correlations become negligible and the charge-lattice coupling is dominant. The transport properties of lattice polarons for strong electron-phonon coupling, in which charge carriers self-localize in energetically favorable lattice distortions, were first discussed in disordered materials (Holstein, 1959 [30]) and later extended to crystals (Mott and Davis, 1971). If the carrier, together with its associated crystalline distortion, is comparable in size to the cell parameter, it is called a small, or Holstein, polaron. The electron-phonon interaction has a short and a long range component. The short one is due to interaction between the charges and the on-site crystalline fields and gives rise to the formation of small polarons. The long range component is due to the Coulombian potential that couples the charge with the electric dipoles of a ionic solid. This contribution gives rise to the formation of large polarons, in witch the distortion spread over more lattice sites. Large polarons have an itinerant character due to their small effective mass ($m^* \sim 2 - 4$) and the lattice distortion extended over a wide spatial range. On the other hand, small polarons could move only by tunneling or thermally activated hopping between locally distorted lattice sites because of the large effective mass ($m^* \sim 10 - 100$) and the distortion of the lattice extended over a domain of one or few atomic sites.
Nevertheless, while metal to insulator transition in EuO can be successfully explained by supposing a transition from large to small polarons as the ferromagnet disorders, in manganites the situation is more complex. It has been experimentally demonstrated by the means of structural and transport measurements and using a variety of techniques, such as x-ray and neutron diffraction, absorption and resistivity measurements, that the presence of polarons is not only limited to the high temperature/paramagnetic phase. As anticipated when describing the crystallographic properties of manganites, there exist clear evidences that polarons cross the metal to insu-

lator transition and are present even well inside the metallic region. Studies on the thermal behavior of the conductivity confirm this result. In particular, Moreo et al. [52] proposed a model based on the co-presence of conducive-ferromagnetic clusters and insulating-paramagnetic ones in both phases. Clusters size changes when the transition is approached: ferromagnetic clusters reduce their size when the transition is crossed from ferromagnetic to paramagnetic, viceversa, paramagnetic clusters increase their size. The opposite occurs while the transition is crossed in the opposite direction. The application of an external magnetic field aligns the polarization of ferromagnetic clusters and increases their size. When FM clusters overlap one with another an overall metallic behavior is achieved. This can explain the great sensitivity of these materials to magnetic fields. At high temperatures the dominant transport mechanism is thermally activated hopping, with an activated mobility that follows the law:

$$\mu_p = \frac{x(x-1)\,e\,a^2}{h}\left(\frac{T_0}{T}\right)^s \exp\left[-\frac{W_H - t}{k_b T}\right] \tag{1.24}$$

where a is the hopping distance, x the polaron concentration, and W_H one-half of the polaron formation energy. There are two physical limits for these hopping processes, depending on the magnitude of the optical phonon frequency. If lattice distortions are slow compared to the charge carrier hopping frequencies, the hopping is adiabatic, otherwise it is non-adiabatic. In the adiabatic limit, $s = 1$ and $k_B T0 = \hbar\omega_0$, where ω_0 is the optical phonon frequency while in the non-adiabatic limit, we have $s = 3/2$ and $k_B T_0 = (pJ^4/4W_H)^{1/3}$. The polaronic transport in manganites is usually considered adiabatic, in this case the conductivity is given by:

$$\sigma = \frac{x(x-1)\,e^2\,T_0}{\hbar\,a\,T}\ \exp\left[-\frac{\varepsilon_0 + W_H - t}{k_b T}\right] = \frac{\sigma_0\,T_0}{T}\ \exp\left[-\frac{E_\sigma}{k_b T}\right] \qquad (1.25)$$

The temperature dependence observed in the high temperature resistivity of manganites follows this adiabatic prediction very well, from temperatures close to T_c up to 1200 K. At high enough temperature magnetic correlations can be completely ignored, since charge-lattice and charge-charge interactions dominate. In this regime on-site Coulomb repulsion has been observed in support of the small polaron picture. Small grain polycrystalline samples, very thin and unannealed films, on the other hand, have been reported to show variable-range-hopping-type localization and non-adiabatic small polaron transport.

Chapter 2

Double perovskites

2.1 Introduction

In this chapter I will first describe the iron-molybdenum based double perovskite compound of chemical formula Sr_2FeMoO_6 ; this system will be the starting point to understand the properties of the doped double perovskite compounds studied in this thesis work: the $Sr_2FeMo_xW_{1-x}O_6$ series. Like manganites, double perovskite compounds present a large magnetoresistance effect. But in contrast to manganites, the Curie temperature (T_c) is well above room temperature (> 400 K). Moreover, the magnetic field required to achieve a significant magnetoresistance effect is much lower than in manganites. These two properties make these compounds good candidates for a widespread technological use in the emerging field of spin driven devices, the so called *spintronics*.

In this thesis, such compounds have been studied from a structural point of view. An X-ray based spectroscopic technique (EXAFS, see chapter three) has been exploited to study the local structure around each atomic site (with the exception of the oxygen site). What we expected from this investigation is a link between the local microscopic lattice structure and the macroscopic

physical properties.

In this chapter I will first introduce the crystallographic structures found using diffraction techniques. These structures will be used as reference structures to which our results will be compared.

I will then discuss the most recent theories developed to explain the magnetic structure and the electronic transport, whose understanding requires, as in manganites, a detailed knowledge of their electronic and structural properties. Early theories developed to explain magnetotransport in manganites, and reported in the previous chapter, are essential to understand the physics underlying double perovskites. In fact, even if there are fundamental differences between manganites and double perovskites, the theories stated for the former can be taken as a starting point for understanding the latter. Once the origin of the peculiar magnetic structure of the undoped compound (Sr_2FeMoO_6) has become clear, I will introduce the issue regarding the double perovskite W doped series: $Sr_2FeMo_xW_{1-x}O_6$.

In this chapter I will also report and discuss measurements performed with a variety of techniques and the theories proposed to explain them. These will basis for the interpretation of our data, exposed in the last chapter.

2.2 The Sr_2FeMoO_6 compound

2.2.1 Crystallographic structure

Sr_2FeMoO_6 is a double perovskite, belonging to the $A_2BB'O_6$ family. The unitary cell is doubled, with respect to conventional perovskites, in the sense that Fe and Mo atoms alternate on the B and B' sites respectively, each sublattice having a perovskite structure. The ideal cubic double perovskite structure can be described as an interpenetration of two FCC sublattices. Ordered Fe (and Mo) octahedra are centered at the cube corners and are connected to each other through oxygen atoms, which occupy the corners of

the octahedra and are located on the edges of the unit cell (see figure 2.1). Sr atoms are placed at the center of the cube.

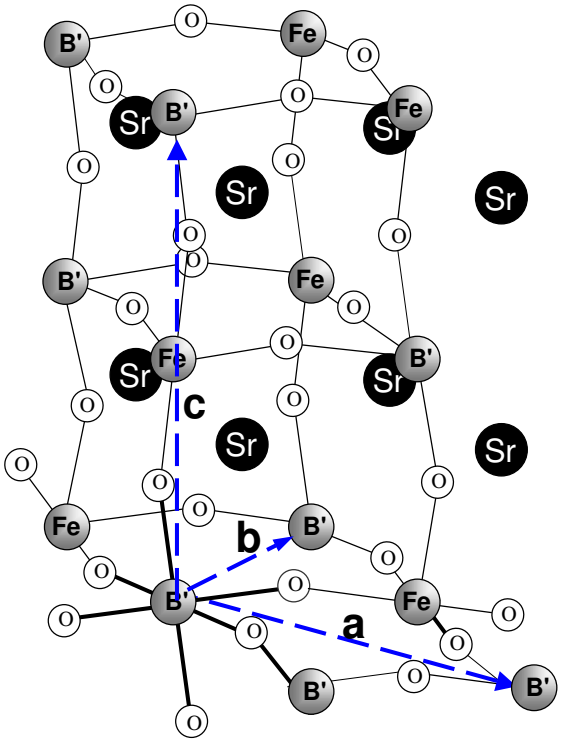

Figure 2.1: Schematic view of a generic $Sr_2FeB'O_6$ double perovskite unitary cell. The arrows represent the lattice vectors a, b and c

The crystallographic structure was suggested to be either tetragonal ($a = b \neq c$) with
$\sqrt{2}a_p$ $\sqrt{2}a_p$ $2a_p$ (where a_p is the lattice parameter) or pseudocubic [54, 56] ($2a_p$ $2a_p$) $2a_p$. More recently, a cubic $Fm3m$ ($a = b = c$) structure has been proposed [27].
Many groups performed neutron or X-rays diffraction measurements on Sr_2FeMoO_6 at different temperatures [15, 27, 54, 56]. Refinements of this data converge on a tetragonal structure, according to a $I4/m$ space group, at room temperature, while, rising the temperature, the system undergoes a structural phase transition from tetragonal $I4/m$ to cubic $Fm3m$ at $\sim$ 400 K (which

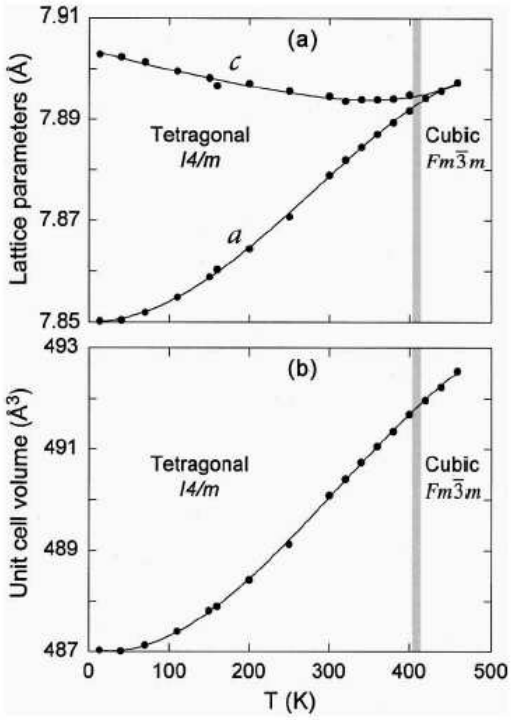

Figure 2.2: (a) Evolution of the lattice parameters, **a** and **c**, as a function of temperature. The parameter **a** is multiplied by $\sqrt{2}$ in the tetragonal region. (b) Plot of the unit cell volume (multiplied by 2 in the tetragonal region) as a function of temperature (from [15])

corresponds to the Curie temperature). Table 2.1 reports the structural parameters obtained by neutron diffraction data at 70 and 460 K while table 2.2 reports the lengths of some selected bonds at the same temperatures. Lowering the temperature, the structure evolve continuously (fig. 2.2) from the $Fm3m$ high temperature cubic structure, with the simultaneous development of a tetragonal strain ($c > a$) and the rotation of the FeO_6 and MoO_6 octahedra up to 5.6^0. The tetragonal distortion, occurring under the Curie temperature, seems to arise from the antiphase rotation of the oxygen octahedra with respect to the c-axes.

Space group	$Fm3m$	$I4/m$
T(K)	460	70
a(Å)	7.89737(3)	5.55215(2)
c(Å)		7.90134(5)
c/a		1.42311
Vol.(Å^3)	492.546	243.570(3)
Fe(0 0 0)	$n = 0.99(1)$	$n = 0.99(1)$
Mo(0 0 1/2)	$n = 0.94(1)$	$n = 0.94(1)$
Sr(1/2 0 1/4)		
O(1)(0 0 z)		
z	0.2524(6)	0.2542(8)
O(2)(x y 0)		
x		0.2767(6)
y		0.2266(6)

Table 2.1: Structural parameters of Sr_2FeMoO_6 as refined from neutron powder diffraction data. From Chmaissem et. al [15]. The table reports the lattice parameters (a) and (c) measured at above and below the phase transition temperature ($\sim$ 400 K) together with the cell volume and the crystallographic coordinates. The parameter (n) represents the occupancy.

Space group	$Fm3m$	$I4/m$
T(K)	460	70
Fe-O(1)x2	1.994(4)	2.009(6)
Fe-O(2)x4	1.994(4)	1.986(6)
Mo-O(1)x2	1.956(4)	1.942(6)
Mo-O(2)x4	1.956(4)	1.960(4)
Sr-O(1)x4	2.79396(3)	2.77628(8)
Sr-O(2)x4	2.79396(3)	2.6498(7)
Sr-O(2)x4	2.79396(3)	2.9269(8)

Table 2.2: Bond lengths for Sr_2FeMoO_6 calculated from the structural parameter reported in table 2.1.

2.2.2 Magnetoresistance

Many groups performed magnetoresistance measurements on [37, 77]. Fig. 2.3 shows a typical case (from reference [74]).

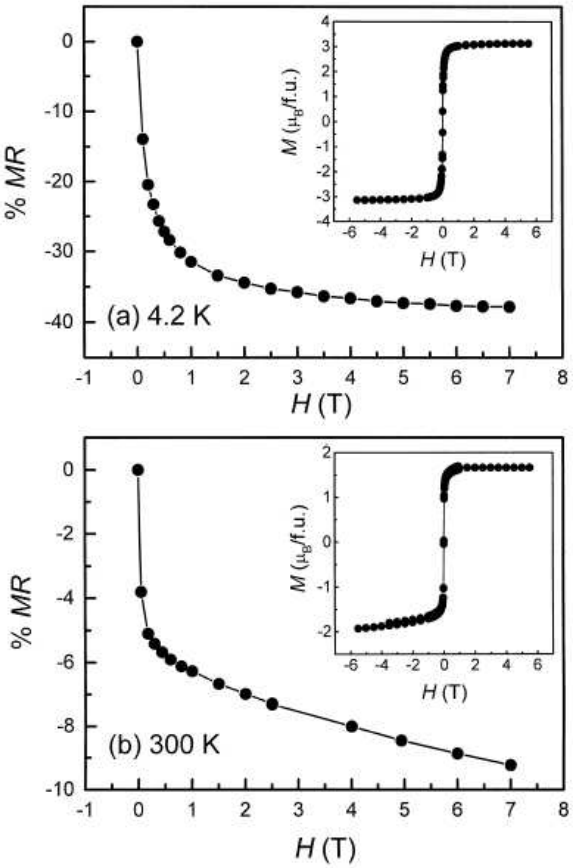

Figure 2.3: Percentage of MR measured at 4.2K (a) and 300K (b) as a function of an external magnetic field (from 0 to 7 T) on a Sr_2FeMoO_6 sample. The magnetoresistance, MR, is defined as: $MR(T,H) = 100[\rho(T,H) - \rho(T,0)]/\rho(T,0)$ where $\rho(T,H)$ is the resistivity measured at a temperature T and magnetic field H. The value of MR is normalized to the zero field value $\rho(T,0)$. The insets show the corresponding magnetization of the sample, which reaches the saturation for low magnetic field values (< 1 T) [74].

At both these temperatures, the sample is characterized by sharp, pronounced magnetoresistive response in the low-field regime, although the magnitude of the MR is considerably higher at low temperature. At 300 K, the MR exhibits a slower change beyond 1 Tesla, while above this value there is no sign of saturation up to the highest magnetic field (7 Tesla). The MR changes significantly, by about 6.5% at 4.2 K and 3% at 300 K, in the larger field region between 1 and 7 Tesla. The low-field response is most likely contributed by the spin scattering across different magnetic domains in poly-

crystalline samples. This conclusion is supported by the absence of a sharp low-field MR response in single crystalline bulk [88] and epitaxial [24] samples of Sr_2FeMoO_6 . In the insets of fig. 2.3 are also shown the magnetization of the sample at the corresponding temperatures as a function the external applied field. The magnetization reaches a saturation value of $3.1\mu_B$ at the lower temperature for a magnetic field value lower than 1 Tesla. At 300 K the saturation magnetization is reduced to a saturation value of $1.8\mu_B$ with the system still magnetic even at room temperature. Such low field MR and magnetization response are very interesting properties from a technological point of view because allows their use in normal conditions such as room temperature and low magnetic field.

2.2.3 Electronic structure

A key feature that determines the magnetic order of Sr_2FeMoO_6 is the half-metallic nature of its ground state, which derives from the electronic structure. The first attempt to determine the electronic structure was done by Kobayashi [37] by means of density of state (DOS) simulations, and later by Sarma [75] with more detailed calculations. Figure 2.4 reports DOS calculations from Sarma et al. showing: the total DOS, that of majority spin up and of the minority spin down states together with the DOS for the single elements.

From figure 2.4 it is evident the half-metallic ground state nature of this compound: a non-zero DOS is present at the Fermi level for the down-spin band, whereas, the up-spin band shows a gap at the Fermi level. The occupied up-spin band is mainly composed of Fe 3d electrons hybridized with oxygen 2p states (corresponding to the $3d^5$ configuration) and much less of the Mo 4d electrons that are located above the Fermi level. By contrast, the down-spin band is mainly occupied by oxygen 2p states and, at the Fermi level, by both the Mo 4d t_2g and Fe 3d t_2g electrons that are strongly hybridized with

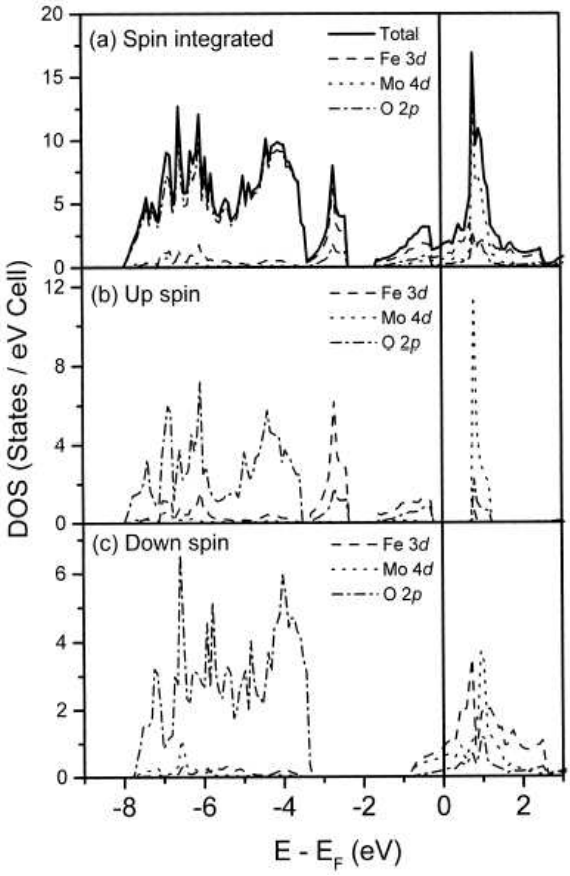

Figure 2.4: The figure shows the density of states (DOS) along with partial Fe d, Mo d and O p density of states. (a) Spin integrated densities. (b, c) The corresponding quantities for the up- and down-spin channels, respectively. (from ref. [75])

the oxygen 2p states. Such a half-metallic nature gives rise to 100% spin polarized charge carriers in the ground state. Considering the fairly high T_c, a high percentage of this spin polarization lasts even at room temperature: a polarization higher than 60% can be evaluated from the magnetization data reported in the next paragraph.

From a structural point of view, an interesting aspect of the calculations of Kobayashi [37] is the theoretical optimization of the oxygen positions. In fact, while for the lattice parameters he started from the experimentally ob-

element	atomic number	ionic radius	valence state	electronic configuration	spin state
Sr	38	1.32	+2	$4p^4$	1
Fe	26	0.92	+2	$3d^6$	2
		0.78	+3	$3d^5$	5/2
Mo	42	0.75	+5	$4d^1$	1/2
		0.73	+6	$4d^0$	0
W	74	0.76	+5	$5d^1$	1/2
		0.74	+6	$5d^0$	0
O	8	1.24	-2	$2p^4$	1

Table 2.3: Synoptic table containing relevant physical information on elements present in the studied compounds.

served values (table 2.2), the oxygen positions were optimized obtaining a bond length of 2.00 Å(in the ab plane) and 2.01 Å(c axis) for Fe-O and 1.94 Å(ab plane) and 1.95 Å(c axis) for Mo-O. These values are important as reference values for the local structure characterization of these compounds that is one of the aims of this work.

2.2.4 Magnetic structure

Fe and Mo are the relevant ions in determining the magnetic properties of Sr_2FeMoO_6 . Iron is a magnetic ion that can assume a valence state of 2+ or 3+ with a high-spin state of $S = 5/2$ and $S = 2$, respectively. To achieve the charge neutrality, Mo ion can assume a valence state of 5+ or 6+, corresponding to a spin state of $S = 1/2$ or $S = 0$, respectively. Table 2.2.4 summarizes the relevant data of the elements present in these compounds.
Kobayashi [37] claimed the magnetic coupling between Fe and Mo sublattices

to be ferrimagnetic (figure 2.5), resulting in a net magnetic moment of $4\mu_B$ per formula unit (that is, roughly, $5\mu_B$(Fe)$-1\mu_B$(Mo)).

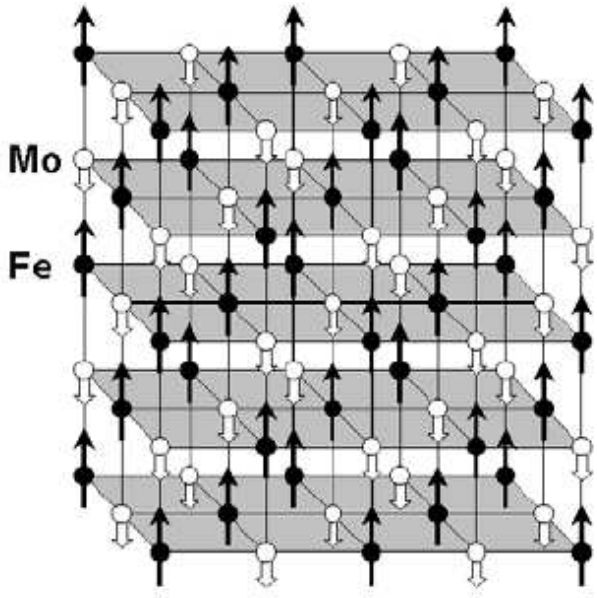

Figure 2.5: Schematic picture of the ferrimagnetic arrangement of Sr_2FeMoO_6 .

It is worth to note that the other potential valence state configuration, $Fe^{2+}-Mo^{6+}$, also yields to a net magnetic moment of $4\mu_B$ with Mo being non-magnetic. Since these two different valence states configurations are equivalent from a magnetic point of view, they cannot be distinguished by magnetic measurements. The actual valence state in the Sr_2FeMoO_6 compound is still a matter of debate. Mossbauer spectroscopy can help to determine the actual valence state for Fe and Mo ions. Early measurements [54] were interpreted in favor to the high spin ($S = 5/2$) Fe^{3+} configuration with a small reservation towards the possibility of the other high spin state (Fe^{2+} ($S = 2$). Consequently, Mo was assigned to the 5+ valence state corresponding to an $S = 1/2$ spin state. More recent Mossbauer studies [42], instead, retrieved an intermediate valence state (2.5+) for the Fe ion. On the other side, recent neutron diffraction experiments reported a value of

$\mu = 4.1 \pm 0.1\mu_B$ for the magnetic moment on the Fe site and $\mu = 0.0 \pm 0.1\mu_B$ for the Mo site. These experimental results can be combined by assuming a $Fe^{3+}-Mo^{5+}$ configuration and supposing the antiferromagnetically coupled electron of the Mo^{5+} ion to be completely itinerant. In this scenario, no net magnetization is present on the Mo site, in agreement with the experimentally observed value of the Mo magnetic moment; the itinerant electron decreases the spin of the Fe site from $S = 5/2$ to the experimentally observed value of $S = 2$. In this framework, Sr_2FeMoO_6 consists of Fe and Mo sublattices ferromagnetically coupled within each sublattice, while the two sublattices are supposed to be antiferromagnetically coupled resulting in a net $S = 2$ spin state. It is worth to note that the valence-fluctuation state picture, in which the Fe site is in the +2.5 intermediate state, formally corresponds to an higher spin state: $S = 2.25$. This spin value corresponds to a theoretical magnetic moment of $4.5\mu_B$ for the Fe iron and of $0.5\mu_B$ for that of Mo. This discrepancy can be explained by taking into account the Fe/Mo mis-site disorder as discussed more in detail in a following paragraph, that reduces the net magnetization.

Different mechanisms have been suggested to explain the observed magnetic structure. In close analogy to the case of manganites, it has often been suggested [74] that a double exchange mechanism is responsible for the ferromagnetic coupling between the Fe sites. In this scenario, the delocalized electron contributed by the Mo 4d configuration plays the role of the delocalized e_g electron in the manganites. However, there are important differences between the physics of manganites and double perovskites. In manganites, both the delocalized e_g electron and the localized t_{2g} electrons reside at the same site, namely the Mn sites (see figure 1.5, chapter 1). The spin of t_{2g} localized states are ferromagnetically coupled to the spin of the e_g delocalized electron due to the strong intra-atomic Hund's coupling strength, which originates from the exchange stabilization of the parallel spin arrangement. In the

case of Sr_2FeMoO_6 , instead, the delocalized electron at the Mo site and the localized electrons at the Fe sites reside at two different sites. Nevertheless, band structure results suggest that the mobile Mo 4d electrons have a finite Fe 3d character due to sizable hopping via the oxygen 2p orbitals. But, since the localized up-spin orbitals at the Fe site are already fully filled, in order to hop to the Fe site, the delocalized electron must be spin-down oriented. Since Hund's coupling, which is at the origin of the double exchange mechanism for manganites, only acts between parallel spin electrons, it cannot be invoked as responsible of the ferromagnetic alignment of the Fe atoms in the case of double perovskites. As a consequence of these arguments, coupling between the localized and the delocalized electrons must be antiferromagnetic and originating from the Hund coupling mechanism. In [14], the ferromagnetic Curie temperature (T_c) have been calculated within a double exchange type Hamiltonian, but assuming an antiferromagnetic coupling between the localized and delocalized spins. We stress here that any well-defined coupling (ferromagnetic, antiferromagnetic or other) between the delocalized electrons and the localized electrons at each Fe site will lead to a ferromagnetic ordering of the Fe sublattice. Thus, understanding the ferromagnetic ordering of Fe ions in Sr_2FeMoO_6 is nothing else than understanding the nature and origin of the coupling between the the mobile and the localized electrons in these compounds.

It has been proposed [59] that the antiferromagnetic coupling between the Fe and the Mo sites is due to a superexchange interaction. Nevertheless, a superexchange coupling of the Fe site to the delocalized and highly degenerate (five-fold degeneracy, ignoring crystal-field effects) Mo 4d states will, at best, be very weak, and therefore not compatible with the unusually high ordering temperature that implies a strong interaction. Moreover, it should be noted that superexchange interactions require a perfectly ordered double perovskite structure, ensuring Fe-O-Mo-O-Fe 180^0 interactions, to give rise

to a ferromagnetic coupling of the Fe sublattice. Another argument against the superexchange interaction is that this scenario would suggest that also Fe-O-Fe bonds, always present due to the chemical disorder always present in these compounds, would be antiferromagnetically coupled. Band structure calculations, performed by Sarma [75] using supercells to simulate mis-site disorder between Fe and Mo sites, show that Fe and Mo sites are invariably coupled antiferromagnetically, driving a ferromagnetic order in the Fe even in presence of Fe-O-Fe bonds in this system. These observations demonstrate that the superexchange interaction is not the driving force for the magnetic ordering in these compounds.

2.2.5 The kinetic driven mechanism

A well-defined spin ordering between the delocalized Mo electron and the localized Fe electrons implies the presence of a large spin splitting in the delocalized band derived from the Mo 4d and oxygen 2p states. This is surprising because that Mo is not a strongly correlated atom and, consequently, a magnetic moment at the Mo site is a rarity. As stated before, experimental evidences and band structure simulations show an antiferromagnetic coupling between Mo and Fe atoms, in contrast to the ferromagnetic coupling of manganites. The large magnetic transition temperature in Sr_2FeMoO_6 points to a strong interatomic exchange coupling between Fe and Mo ions, comparable, or even larger, than that between the Mn-Mn pairs in the manganites, in spite of the expected non-magnetic nature of Mo. Sarma et al. proposed a novel mechanism to explain the magnetic interaction between localized and conduction electrons, leading to such a strong polarization of the mobile charge carriers [75]. To establish an antiferromagnetic ordering between Fe and Mo ions, the ground state must have an opposite spin orientation of Mo and Fe ions. To find a mechanism that can give rise to such a ground state, they looked very closely to the energy levels of the Mo and Fe sites. Different

effects contribute to split their energy levels of:

- The exchange interaction, which is due to the relative spin orientation between electrons belonging to the same energy level;
- The crystal-field interaction, which arises from electric fields originating inside the crystal lattice. It depends on the ion neighborhood (chemical environment, coordination...);
- The hybridization, which origins from the overlap between electronic wave functions between neighbor sites;
- The hopping interaction, which is due to the hopping of a conduction band electron from a site to another; as the hybridization, it depends by the mixing of the electronic wave functions belonging to different sites.

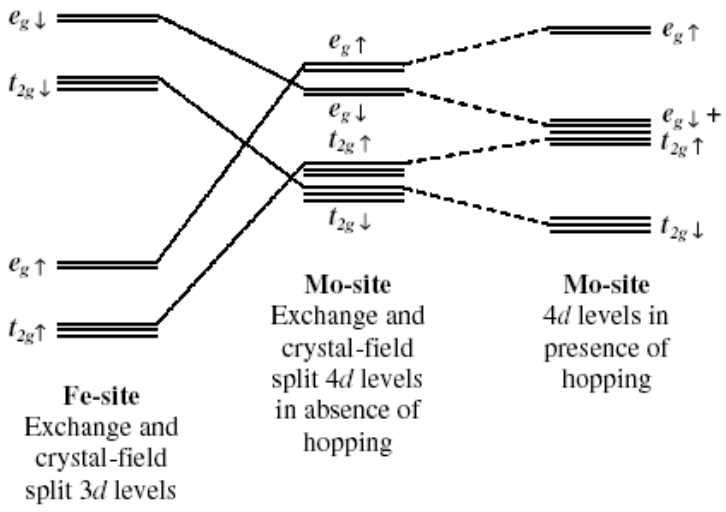

Figure 2.6: Schematic picture of the energy levels of the Mo and Fe sites in the presence of exchange, crystal field and hopping interactions.

The energy level scheme resulting from detailed band structure calculation performed by Sarma et al. is reported in figure 2.6 and is discussed in the

following:

- Fe site (figure 2.6, left): The octahedral symmetry of the Fe site produces crystal field interactions that split the 3d energy level orbitals into the t_{2g} three-fold degenerated states and the e_g two-fold degenerated states; the exchange interaction further splits each symmetry into up and down spin levels. In the case of Fe, the exchange splitting is much larger than the crystal splitting.

- Mo site (figure 2.6, center): The Mo 4d energy levels are strongly hybridized with the oxygen 2p levels returning the band states shown in the figure. As in the Fe case, both crystal field (coming from the octahedral symmetry) and exchange interaction act in splitting the energy levels into t_{2g} and e_g symmetries and up and down spin states, respectively. Nevertheless, contrary to the Fe case, the strength of the forces responsible for the energy splitting are reversed: in the case of Mo the crystal field is much greater than the exchange interaction.

Moreover, because the magnetic order results stable, it is necessary for the energy splitting between the ground state levels to be substantial. This peculiar band states configuration is achieved by considering the interactions coming from the hopping of the itinerant electron between Mo and Fe sites, as shown on the right side of Figure 2.6, resulting in a significant spin up-spin down level splitting if the Mo states. Hopping interactions couple the Fe localized states to the delocalized states derived from the Mo 4d - O 2p hybridization, leading to a substantial admixture between these two states. These interactions act between states of same symmetry shifting their energy levels. As shown in fig. 2.6, the delocalized $t_{2g} \uparrow$ states will be pushed up and the $t_{2g} \downarrow$ states will be pushed farther down by hybridization with the corresponding Fe states. This opposite shifts of the up and down spin conduction band states induce a spin-polarization of the mobile electrons due to a

pure hopping interaction between the localized electrons and the conduction states. This kinetic-energy driven mechanism leads to an antiferromagnetic coupling between the localized and the conduction electrons, since the energy is lowered by populating the down-spin conduction band with respect to the majority spin orientation of the localized electrons. Detailed calculations [75] have shown that the spin-polarization gap of the conduction band in Sr_2FeMoO_6 is as large as 1-1.5 eV, while, the strength of the antiferromagnetic coupling between the conduction band and the localized electrons at the Fe site is of the order of 18 meV, rather larger than that in the doped manganites, so explaining the high T_c for this compound. This mechanism is operative whenever the conduction band is placed within the energy gap formed by the large exchange splitting of the localized electrons at the transition metal site. When the band generated from Mo 4d - O 2p states is outside the gap, both up and down states are shifted in the same direction and the large energy gain between spin states via such an antiferromagnetic coupling is not possible[1]. This mechanism, proposed in ref. [75], can also explain the metallic ferromagnetic ground state of other related compounds such as Sr_2FeMoO_6 as well as the antiferromagnetic state of Sr_2CoMoO_6 and Sr_2MnMoO_6. The same mechanism has also been indicated as responsible for the magnetism in dilute magnetic semiconductors, like InMnO, where magnetic ions are randomly distributed in the bulk structure quite far away one from the other. As will be discussed in the next paragraph, this mechanism

[1]This is believed to be the case of Sr_2FeWO_6 , where the strong hybridization between the W 5d and the O 2p states drives the hybridized states above the t_{2g} level of Fe. Such an energy level scheme cannot stabilize the antiferromagnetic coupling between the electron in the delocalized states and the localized states; instead, it transfers the electron from the W 5d - O 2p hybridized state to the Fe 3d level, leading to an insulating compound with formally W and Fe states. In the absence of any mobile electrons, the Fe sites couples via superexchange to give rise to an antiferromagnetic insulating state in Sr_2FeWO_6 , in contrast to the metallic ferromagnetic state of Sr_2FeMoO_6 .

is very stable since is primarily governed by two parameters: the effective hopping strength and the charge transfer energy between localized and delocalized states, which are not influenced by chemical or structural disorder.

2.2.6 The effect of the mis-site disorder

Since the ionic sizes of Fe and Mo are similar (see table 2.2.4), there is always a finite concentration of mis-site disorder in Sr_2FeMoO_6 , which interchanges the positions of Fe and Mo sites in a random fashion. The most significant effect of the mis-site disorder in this system is to reduce the net magnetization of the sample. The chemical ordered samples, have usually an ordering degree of about 90% and exhibit a saturation magnetization of $3.1\mu_B$ per formula unit (f.u.) instead of the expected value of $4\mu_B$/f.u. Such a decrease of the magnetization has been ascribed to the finite concentration of mis-site disorder. However, the nature and origin of this decreased magnetization in the presence of disorder is still a matter of debate in the literature.
There are two distinct ways to reduce the net magnetization in Sr_2FeMoO_6 in the presence of mis-site disorders. One is that the disorder destroys the specific spin arrangement of Fe and Mo sublattices without any significant effect on the individual magnetic moments at these sites. This can be achieved by transforming the ferromagnetic coupling between some of the Fe sites to an antiferromagnetic coupling. This view has been preferred by most in recent times, under the assumption that Fe-O-Fe interactions, induced by the mis-site disorder in place of Fe-O-Mo, will be antiferromagnetically driven by the superexchange. Alternately, the magnetic moments at each individual site may decrease due to the different chemical environments induced by the disorder, without affecting the nature of the spin order within the Fe and Mo sublattices. The real situation may even be a combination of both these effects, with a simultaneous reduction in the magnetic moments at different sites as well as a change in the nature of the magnetic coupling between

different sites. Recently, extensive *ab initio* band structure calculations [78] with supercells to simulate mis-site disorders between Fe and Mo have clearly show that the Fe sites continue to be ferromagnetically coupled in every case, including where the bonding contains Fe-O-Fe units. It has also been shown that delocalized electrons, generated from the Mo and O states with some admixture of Fe states, invariably remain antiferromagnetically coupled to the localized Fe moments, in close analogy to the structure of the ordered system. This clearly shows that the magnetic interaction proposed by Sarma et al. always dominates over the superexchange interactions in these systems. Supercell calculations establish that the decrease in the magnetic moment in the presence of disorder arises solely from a change of the chemical environment and can be understood in terms of the local electronic structure around each of the inequivalent Fe.

2.3 The $Sr_2FeMo_xW_{1-x}O_6$ series

$Sr_2FeMo_xW_{1-x}O_6$ is a solid solution with x varying over the whole range spanning from the end compound Sr_2FeMoO_6 at $x = 1$, to the compound at the other end of the series: Sr_2FeWO_6 at $x = 0$. Even if it belongs to the same double perovskite family of Sr_2FeMoO_6 , Sr_2FeWO_6 shows different electrical transport and magnetic properties. It contains W^{6+} $5d^0$ and Fe^{2+} $3d^6$ species and, in the framework of the above described kinetic driven mechanism, the lack of the Mo $4d^1$ itinerant electron result in the absence of a ferromagnetic interaction between Fe pairs. In addition the cubic structure (space group: $Fm3m$), that ensures 180^0 bond interactions, promotes antiferromagnetic coupling between Fe^{2+} ions via Fe-O-W-O-Fe super-exchange interaction. As a result of these properties, in contrast to Sr_2FeMoO_6 , Sr_2FeWO_6 is insulating at all temperatures with an antiferromagnetic ordering below 37 K. As for mixed valence manganites, the $Sr_2FeMo_xW_{1-x}O_6$

doped series is expected to have intermediate properties between the two end compounds (Sr_2FeMoO_6 and Sr_2FeWO_6). Since Sr_2FeMoO_6 and Sr_2FeWO_6 have contrasting transport properties, it is expected that an alloy system of these compounds, such as $Sr_2FeMo_xW_{1-x}O_6$, would exhibit a metal to insulator transition (MIT) as a function of doping, probably associated to a magnetic transition. These two features make this series promising in order to optimize and control the technological potential of these materials. Further, as reported in fig. 2.7, this solid solution shows a reduction of the mis-site disorder present in the Sr_2FeMoO_6 end compound. In fact, due to the very similar ionic radius of Fe^{2+} and Mo ions (table 2.2.4), is difficult to prepare 100% ordered Sr_2FeMoO_6 . The introduction of W_{6+} ion, which has a very different radius from the Fe^{2+} one, increases the Fe/Mo ordering to a value that reaches 100% for $x \sim 0.6$. This results in a almost perfect ordering of the Fe and W/Mo sites, while a random mixing of W and Mo is maintained without any ordering throughout the whole composition. The increased Fe/Mo mis-site order, stabilizes the half metallic ferromagnetic (HMFM) state increasing the MR.

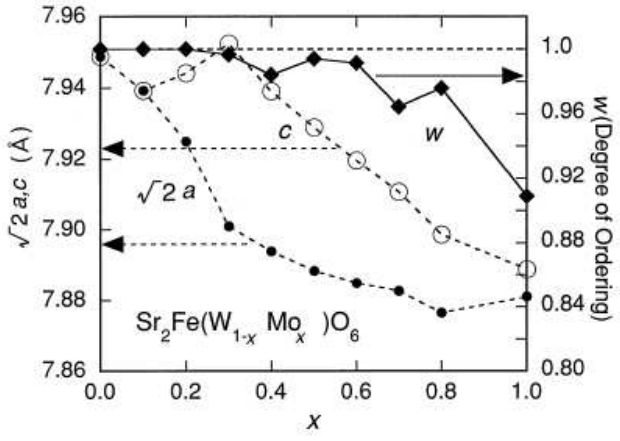

Figure 2.7: Lattice parameter and degree of ordering (w) between Fe and Mo/W in $Sr_2FeMo_xW_{1-x}O_6$ (from [38])

2.3.1 Crystallographic structure

Until the present moment, a structural characterization as a function of the Mo concentration, x, with x varying over the entire range ($0 \leq x \leq 1$), have been performed only using diffraction techniques [37, 21, 67] (X-ray diffraction, XRD, or neutron powder diffraction, NPD). It is worth to note here, and will be stressed more in detail in the next chapter, that structural information obtained with these techniques derive from long range order properties of the crystal lattice, which can be rather different from the short range ones (i.e. the local structure). In the following I will report the results obtained using these long range order techniques, to which our data, collected using a local probe technique such as the X-ray Absorption (XAS), (described in the next chapter) have to be compared.

The structure of the limiting compounds of the series, Sr_2FeMoO_6 and Sr_2FeWO_6 , have been studied extensively [15, 57]. In a XRD study [21], Sr_2FeWO_6 is reported to be almost cubic, while a tetragonal symmetry is found for the rest of the series $Sr_2FeMo_xW_{1-x}O_6$ ($0 < x \leq 1$).
A neutron diffraction study [73], which is more sensitive to the positions of the oxygen atoms, shows that Sr_2FeWO_6 adopts a monoclinic symmetry (space group $P21/n$) from 10 K to room temperature, while Sr_2FeMoO_6 is confirmed to be perfectly described by the tetragonal $I4/m$ space group. Therefore, a structural transition from tetragonal to monoclinic symmetry is expected at some x. Sanchez et al. [73] studied samples having $x = 1.0$, 0.8, 0.5, 0.2, 0.0 and found that, for $x \geq 0.5$, samples have a tetragonal symmetry. They have also shown that the diffractograms refinements improve if a magnetic phase is included in the model, accordingly with the ferromagnetic behavior of these samples. High W concentrations $x < 0.3$, could not be satisfactory fitted using a tetragonal space group and the structure have been successfully refined using the monoclinic, $P21/n$, space group.

Since the crystallographic structures found by Sanchez et al. have been used in this work as references structures, we will report them more in detail in the last chapter together with our results.

2.3.2 Resistivity

Resistivity measurements on the $Sr_2FeMo_xW_{1-x}O_6$ series have been performed both by Kobayashi et al. [38] and Sarma et al. [67] by the means of conventional DC four-probe method.

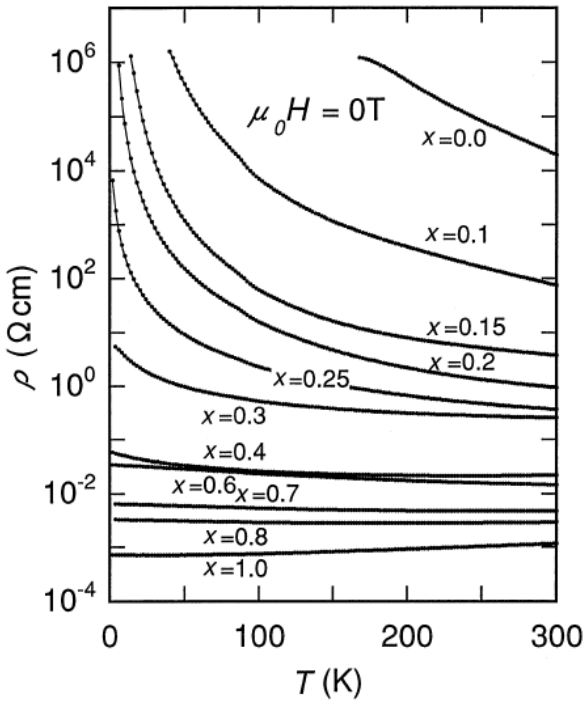

Figure 2.8: Temperature (T) dependence of the resistivity (ρ) of polycrystalline $Sr_2FeMo_xW_{1-x}O_6$ measured at zero magnetic field. (from [38])

Figure 2.8 reports electrical resistivity, on a logarithmic scale as a function of temperature: resistivity values decreases with increasing x over the whole Mo composition range. The plots show two different regimes: samples with

$x \geq 0.3$ have low resistivities, between 10^{-4} and 10^{-1} Ω/cm, and exhibit metallic behavior (even if only for $x = 1.0$ the metallic condition, dρ/dT> 0, is respected over the whole T-region). On the other hand, samples with a composition $x \leq 0.2$ are insulating or semiconducting with resistivity values between 10 and 10000 Ω/cm. The resistivity of the polycrystalline $x = 1$ sample is of the order of 10^{-4} Ω/cm, comparable to that of the single crystal. These results clearly establish a metal-insulator transition as a function of the composition in the range $0.3 > x_c > 0.2$, where x_c indicates the critical composition. Different groups reported slightly different values for the resistivity [67, 54, 35] and the critical composition. The latter has been reported to be $x_c = 0.4$ by [54]. Sarma have proposed that these discrepancies are due to grain boundary effects, which appear to depend substantially on the sample preparation, particularly on their sintering temperature. Sarma also noted a time dependence of the resistivity explaining it as an indication of a slow oxidation of grain surfaces that results in the introduction of an insulating grain boundary layer. He proposed a simple model to interpret the resistivity data. He remarked that a single conduction mechanism is not able to account resistivity data as a function of T for all the compositions. As a matter of fact, in insulating oxide materials the electronic transport at low temperature is mostly due to very low density of localized states, introduced by impurities and non-stoichiometry, within the band gap region of the stoichiometric compound. On the contrary, high temperature behavior is dominated by thermally activated charge carriers across the band gap. Considering both these two effects he modeled the conductivity dependence on temperature as:

$$\sigma(T) = \sigma_1 \exp[-E_g/2K_BT] + \sigma_2 \exp[-(T_0/T)^{1/4}] \tag{2.1}$$

where the first term represents the activated behavior (E_g being the energy band gap) while the second term accounts for the variable-range hopping

(VRH) within the localized low density of states in the midgap region. Using this model to fit the experimental conductivities it resulted that, for the $x = 0$ compound, the activated behavior largely dominates over the VHR contribution throughout the temperature range (except for the lowest temperatures), indicating only a small influence from defects states. On the contrary the conductivity of the $x = 0.2$ sample deviates very pronouncedly from the activated behavior, being in excellent agreement with a model described by a single VRH term. These considerations confirm that Mo doping the Sr_2FeWO_6 end compound introduces a significant density of states at the Fermi level. The transport behavior is consistent with the scenario in which Mo is in the Mo^{5+} state with the 4d density of states contributing electrons for the conduction, while the $5d^0$, states belonging to W, do not contribute at the Fermi level. This conclusion is in agreement with the Mossbauer data that, as discussed above, show that, for $x = 0.3$, Fe exist both in the 2+ and 3+ states, while for $x = 0$ it is found only in the 2+ state. Therefore, the conversion of Fe^{2+} to Fe^{3+} by Mo doping, in the $0 < x < 0.3$ range, must be due to the doping of Mo^{5+} substituting of W^{6+} species.

2.3.3 Magnetization

Figure 2.9 and 2.10 report the magnetization as a function of the magnetic field and of the temperature, respectively, performed by Kobayashi et al. and Sarma et al. [37, 67]. From the magnetization curves shown on fig. 2.9 it is again evident the different behavior for samples having $x \geq 0.3$ respect to samples with $x \leq 0.3$:

- At low Mo content (samples with $0 \leq x \leq 0.2$) magnetization is present only after 10% substitution of W with Mo, and increases steeply with increasing Mo level. The magnetization curves exhibit a spin-canting feature associated with a large coercive field which reaches the highest

value of 0.4 T for $x = 0.15$. The M-T curves (Fig. 2.10) show a cusp or broadened peak feature around 50K. In the case of Sr_2FeWO_6 ($x = 0$), corresponding to the antiferromagnetic transition at $T_N = 37K$. The Curie-Weiss trend for Sr_2FeWO_6 ($x = 0$) gives $S = 2.3$ provided that $g = 2.0$. This suggests a high spin configuration for Fe^{2+} ($S = 2$), being consistent with the result obtained by Mossbauer spectroscopy [21]. The cusp in the M-T curve in the composition range of $0.1 < x < 0.4$ suggests the remanence of antiferromagnetism even above $x = 0.3$.

- For higher Mo content, $0.3 \leq x \leq 1$, the coercive field diminishes to a minimum value of 0.008 T for the $x = 0.6$ sample, while, the magnetization nearly reaches its saturation at 1 T for all compounds with $x > 0.4$. The saturation magnetization is $3 \div 4\mu_B/$ f.u., in agreement with the net magnetic moment expected for the antiferromagnetic coupling between Fe^{3+} and $(W, Mo)^{5+}$ or Fe^{2+} and $(W, Mo)^{6+}$. The magnetization decreases slightly above $x = 0.8$, which is ascribed to a slight increase of the mis-site disorder on the Fe/Mo sites (see ordering factor in fig. 2.7).

From figure 2.10 it is evident that the ferromagnetic transition temperature, T_c, increases remarkably with increasing Mo content, x, exceeding room temperature for $x > 0.3$.

2.3.4 Comparison between conductivity and specific heat measurements

Fig. 2.11 (from reference [37]) shows the dependence of the magnetization as a function of x at 5 and 1T in comparison with the conductivity, σ.
As expected (fig. 2.11(a)), conductivity, is essentially zero for $0 < x < 0.2$. The insulating behavior in this region is consistent with the results of the electronic specific heat coefficient, γ (linear term coefficient of the specific

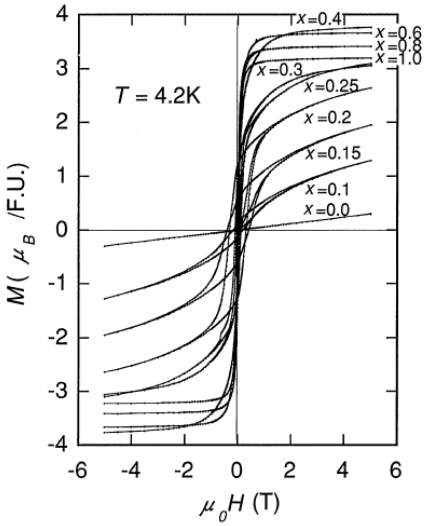

Figure 2.9: Magnetization (M-H) curves of $Sr_2FeMo_xW_{1-x}O_6$ at 4.2 K.

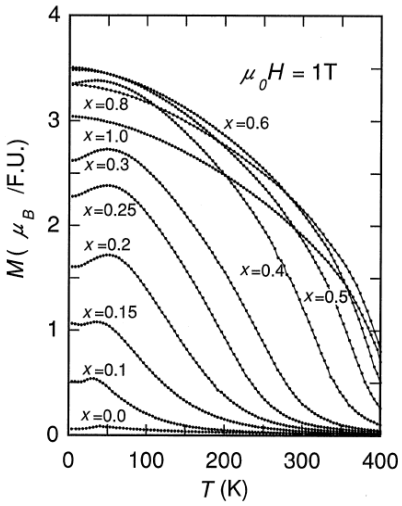

Figure 2.10: Temperature (T) dependence of the magnetization (M) of $Sr_2FeMo_xW_{1-x}O_6$ measured at 1T.

heat), shown in fig. 2.11(a). The value of γ is zero for $0 < x < 0.25$, confirming the absence of the density of states at the Fermi level. Above $x = 0.25$, γ increases gradually with x up to the value of 8 mJ/K mol for $x = 1$. The conductivity behavior confirms the insulator-metal transition to occur around $x \sim 0.25$; while the conductivity increases steeply in the range of $0.25 < x < 0.4$ by more than four orders of magnitude.

2.3.5 Magnetoresistance

Sr_2FeMoO_6 exhibit a large and sharp drop in resistance on application of a magnetic field even at room temperature. Negative magnetoresistance values measured by Sarma et al. [67] at room temperature as at 4.2 K are reported in table 2.3.5.

Figure 2.12 reports magnetoresistance for $x > 0.3$ samples ($x = 0.3, 0.6$ and 1.0). All these compounds exhibit a sharp drop in resistance at a very low

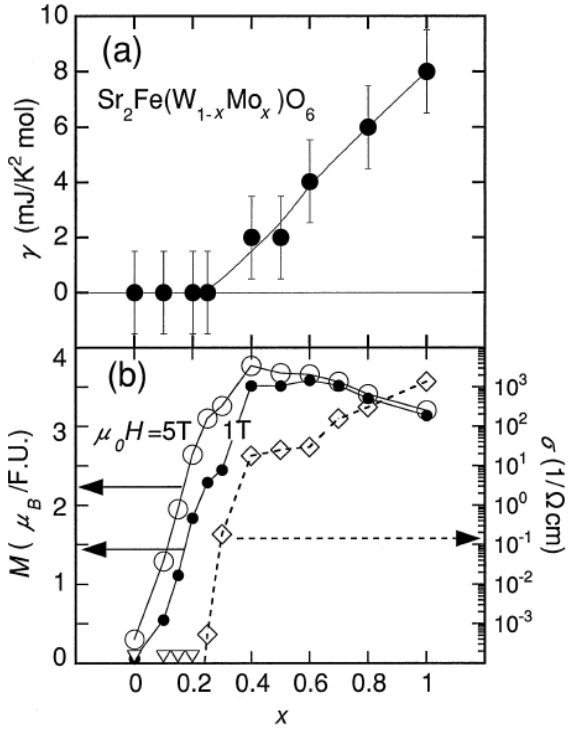

Figure 2.11: (a) Electronic specific-heat coefficient (γ) for $Sr_2FeMo_xW_{1-x}O_6$. (b) magnetization (M) at 1 and 5T, and conductivity (s) at 4.2K for $Sr_2FeMo_xW_{1-x}O_6$. σ is essentially zero for $x < 0.2$, represented by open triangles.

applied field (< 0.5 T). The low field magnetoresistance is due to the suppression of the intergrain spin dependent carrier scattering, when the grain magnetic moments order one with the other. In this situation, the conduction electron, which is a spin down electron, can tunnel from one grain to an adjacent one, when the spin of the second grain is not parallel to the first the tunneling is forbidden by the Pauli exclusion principle. As exposed above, the spin polarization increases with Fe/Mo cation ordering (fig. 2.9). In the $x > 0.3$ region, the magnetoresistance response increases as a consequence of the increased chemical ordering due to the W doping. As shown in table 2.3.5, this is not always the case; this effect is probably due to grain boundary effects (e.g. changes in grain boundary thickness or chemical composition

Sample	4.2K (5.5T)	300K (5T)
$x = 0.2$		1%
$x = 0.3$	8%	0.7%
$x = 0.6$	30%	8%
$x = 0.8$		3%
$x = 1.0$	37%	9%

Table 2.4: Percentage of MR measured at 4.2K at a magnetic field of 5.5T and at 300K at 5T. Here the MR is defined as: $MR = 100[\rho(T,H) - \rho(T,0)]/\rho(T,H)$ where T represents the temperature and H the magnetic field.

from sample to sample) present in the polycrystalline samples.

An extremely large magnetoresistance effect is observed also for the $x = 0.15$ sample, below the metal-insulator transition (fig. 2.12). As discussed above, this x region present a spin-canted magnetization curve with a maximal coercive field and semiconducting behavior (see fig. 2.9). Since, T_c is around 200 K for the $x = 0.15$ sample, MR is not observed at room temperature, while it is present at 16 K. At this temperature MR decreases not so steeply, as in $x \geq 0.3$ samples, on application of an external magnetic field, reaching a value as large as 195%[2] at 7 T. In this region ($x < 0.3$) the MR is believed to belong to the canted-spin feature.

2.3.6 Metal to insulator transition: valence transition versus percolation

The metal to insulator transition (MIT) was reported to occur at different values of the critical concentration, x_c. In an earlier work [54], x_c, was reported to be between 0.4 and 0.5, while more recent studies converge on a value of about 0.25 [37, 67]. As discussed before, it is now believed [67] that

[2]Here the magnetoresistance is defined as: $MR = 100[\rho(T,H_{peak}) - \rho(T,H)]/\rho(T,H)$ where H_{peak} is the magnetic field where the resistivity takes its maximal value.

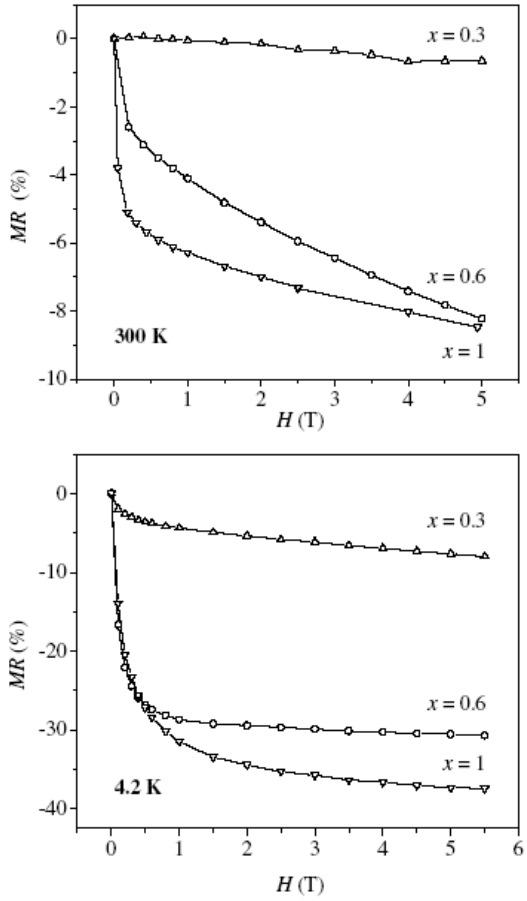

Figure 2.12: Percentage of magnetoresistance for $x = 0.3, 0.6$ and 1 at 300 K (upper panel) and 4.2 K (lower panel).

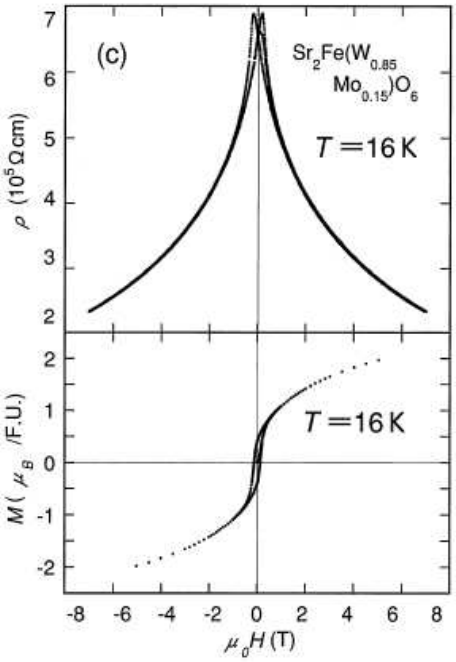

Figure 2.13: MR response for the $x = 0.15$ sample.

the large discrepancies found for x_c are due to grain boundary effects which strongly influence the transport properties in these compounds.
Kobayashi et al. [37], proposed two scenarios to explain the observed results:

Valence transition: At the critical concentration, a collective valence state transition, from the Fe^{2+} -$(W/Mo)^{6+}$ ($x < 0.3$) to the Fe^{3+} -$(W/Mo)^{5+}$ ($x > 0.3$) configuration occurs by substitution of W by Mo. In the high W doping region the valence state is Fe^{2+} -$(W/Mo)^{6+}$ and the 5d conducting

state of the Mo/W site is not occupied by electrons. In these valence states, an antiferromagnetic coupling between Fe^{2+} ions exists, as observed below 37 K in the Sr_2FeWO_6 end compound. Above $x \sim 0.25$, a valence transition (or valence fluctuation) takes place changing the valence state into the Fe^{3+} -$(W/Mo)^{5+}$ state; 5d Mo^{5+} derived states are occupied and the material becomes conductor.

Percolation: In the framework of a percolation process, the nominal valence states of W and Mo remains as 6+ and 5+, respectively, in the whole compositional range, implying that there is no valence transition of Mo and W ions at the critical concentration. Every W^6+ doping in place of Mo^5+ require the transformation of one Fe^{3+} to Fe^{2+} , for charge neutrality. Thus the system is viewed as an inhomogeneous distribution of metallic ferrimagnetic Sr_2FeMoO_6 and insulating Sr_2FeWO_6 clusters. In this model, the MIT is driven by the percolation threshold of the system at the critical composition. The system, in the large x-region (low W level), remains in the macroscopically metallic ferromagnetic state of Sr_2FeMoO_6 , with a distribution of small clusters of insulating and antiferromagnetic Sr_2FeWO_6 . With higher W doping, the insulating Sr_2FeWO_6 clusters grow in size eventually engulfing the metallic Sr_2FeMoO_6 clusters for $x < 0.3$ and giving rise to the observed MIT. A schematic view of the percolation progress is shown in figure 2.14.

As mentioned above, while the ferromagnetic moment emerges by minimal substitution Mo in place of W (i.e. for x as small as $x \sim 0.1$), the occurrence of the conductivity requires x to equal ~ 0.25. A confirmation of the percolation scenario comes from the fact that in $Sr_2FeMo_xW_{1-x}O_6$, the W/Mo-sites form a face centered cubic (FCC) lattice which percolation concentration x_P has been calculated to be 0.195 [80]; this value compares well with the value observed for the critical concentration ($x_c \sim 0.25$) in $Sr_2FeMo_xW_{1-x}O_6$.

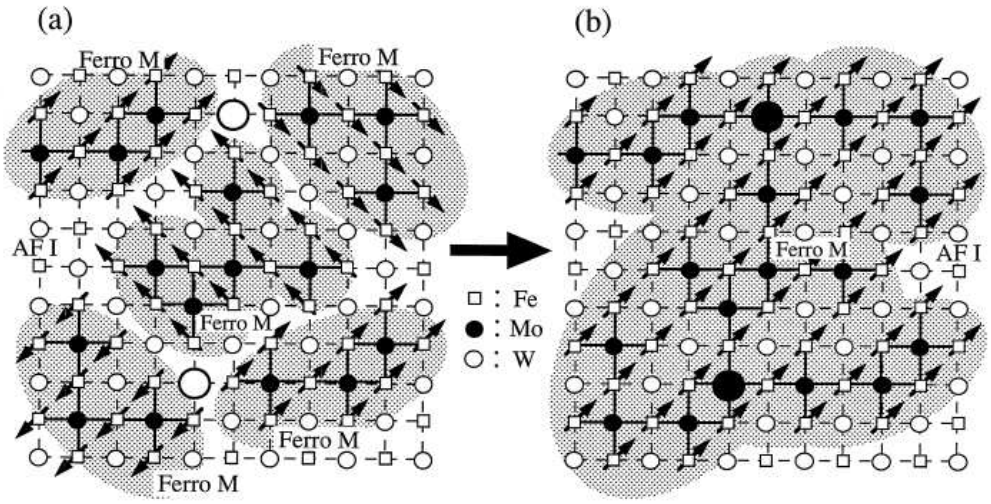

Figure 2.14: The figure illustrates this percolation process around the critical concentration $x \sim 0.25$. If only two W sites shown as large open circles in (a) are substituted by Mo ions, the ferromagnetic clusters represented as a shaded region connect with each other and grow critically in size as shown in (b). (from [38])

Fig. 2.14 illustrates this percolation process around the critical concentration $x \sim 0.25$. If only two W sites shown as large open circles in fig. 2.14(a) are substituted by Mo ions, the ferromagnetic clusters represented as a shaded region connect with each other and grow critically in size as shown in fig. 2.14(b). If one W/Mo-site (expressed by open (W) or filled (Mo) circle) is occupied by Mo ion ($4d^1$), Fe ions around this Mo site will couple ferromagnetically through antiferromagnetic coupling between Fe and Mo ions. On the other hand, the neighboring Fe ions intervened by the nonmagnetic W6+ ion show a weak antiferromagnetic coupling. The ferromagnetic minicluster grows in size by the substitution of W with Mo. In the composition range of $0 < x < 0.2$, the ferromagnetic Sr_2FeMoO_6 clusters are isolated from each other by the Sr_2FeWO_6 domain. On the other hand, in the region of $0.25 < x < 1.0$ beyond the critical percolation concentration, the ferromagnetic clusters become large enough to connect with each other, showing

metallic conductivity.

2.3.7 A more complicated scenario

Both the scenarios proposed by Kobayashi to explain the MIT cannot explain the experimental results for the entire concentration range. From magnetization data we have seen that the saturation magnetization (M_s) increases with the increase of the Mo/W ordering, reaching the maximum value of $4\mu_B$/f.u. for $x = 0.4$. The reduction of M_s at larger x from the theoretical value of $4.1\mu_B$/f.u. to the experimentally observed value of $3.1\mu_B$/f.u. is ascribed to the finite disorder of the samples; this interpretation is confirmed by Rietvield diffraction analysis, which suggests a 90% ordering.

The increase of the ordering at higher W content and the value of the theoretical moment of $4\mu_B$/f.u. seem to be a clear evidence of the presence of both Mo and W in the 5+ state, and of Fe only in the 3+ state for $x < 0.3$. This was confirmed by early Mossbauer data that pointed to a complete absence of the Fe^{2+} in the range $0 < x < 0.5$ while more recent Mossbauer [21] data are more in favor to an intermediate Fe valence state (+2.5). Sarma ascribed these discrepancies in the Mossbauer data to chemical inhomogeneities in samples prepared in different routes and confirmed the presence of the Fe^{3+} -$(Mo/W)^5$+ valence state in the range $0.3 \leq x \leq 1$ in contrast to the scenario which implies the presence of percolating path of $Sr_2FeMo^{5+}O_6$ clusters in a matrix of $Sr_2FeW^{6+}O_6$ antiferromagnetic insulating phase in the whole composition range.

Sarma underlined that we observe not only an increase of M_s with the W content (due to the increased chemical order), but also a full recover of the theoretical moment, proving the system to be homogeneous in the ferrimegnetic state. This is further evidenced by the fact that the conductivities of all the samples are similar for $x > 0.3$. The sudden decrease of the M_s value for $x < 0.3$, in conjunction with the Mossbauer data of [54], exhibiting

the existence of both Fe^{2+} and Fe^{3+} in this range, suggest that there is a valence transition across the critical composition, x_c. It would appear that W transforms into the 6+ state for $x < x_c$, while Mo continues to be in the 5+ state. Thus, charge neutrality requires the formation of Fe^{2+} and Fe^{3+} states. In this inhomogeneous phase, Sr_2FeWO_6 -like regions with the W^{6+} $5d^0$ configuration, being antiferromagnetic, do not contribute significantly to the saturation magnetization and, consequently, M_s decreases rapidly. On the other hand, the Sr_2FeMoO_6 -like phase with the Mo^{5+} $4d^1$ configuration continues to be in the ferrimagnetic state, thereby still retaining a large magnetization for $x = 0.2$. The scenario proposed by Sarma is in contrast with the percolation scenario of Kobayashi in which W is supposed to have the same valence state, 6+, over the entire composition range, but also with the valence transition scenario, which supposes a change of the Mo valence from 5+ to 6+. Another argument against the percolation scenario in the $x < 0.3$ range is that if the samples are thought as a simple mixture of Sr_2FeMoO_6 and Sr_2FeWO_6 even in this range of compositions, we would expect only 20% of the full magnetization value, i.e. $0.8\mu_B$/f.u., for the $x = 0.2$ compound, whereas the experimentally observed value is $2.6\mu_B$/f.u.

Sarma gives two possible explanation for this behavior. The first one is that Sr_2FeMoO_6 -like clusters tend to polarize the neighboring Sr_2FeWO_6 regions magnetically, enhancing the magnetization. The other is to assume a non-homogeneous composition of the sample, with the formation of separated Sr_2FeMoO_6 -like and Sr_2FeWO_6 -like regions of different compositions. For example, the $x = 0.2$ sample can also be thought of as a combination of equal amounts (50%) of ferrimagnetic $x = 0.3$ and antiferromagnetic $x = 0.1$ compounds. In this case, it is easy to see that the sample will appear to have half of the M_s (i.e. $2.0\mu_B$/f.u.) corresponding to $x = 0.3$ sample, which is in better agreement with the experimentally observed value.

As seen, the situation appear to be very complicated and more work is required to establish the microscopic composition in this system. Our data on the local structure around magnetic and non-magnetic ions present in $Sr_2FeMo_xW_{1-x}O_6$, should help to clarify this situation. From a structural point of view, this can be done by identifying the role of the various atoms in the MIT through possible changes in the local order arising crossing the critical concentration.

Chapter 3

Experimental

3.1 The GILDA station

All the measurements were performed on the General purpose Italian beam Line for Diffraction and Absorption (GILDA) experimental station, which is the Italian beamline at the European Synchrotron Radiation Facility (ESRF)in Grenoble. The beamline, financed by three Italian public research, CNR, INFM, and INFN, was built to provide to the Italian scientific community a third generation synchrotron radiation source of high brilliance and intensity. The design provides a high resolution ($\Delta E/E \approx 10^{-4}$) and high flux ($10^{11}$ph/s) source of x-ray in the 5-50 KeV energy range with a less then one square millimeter (1mm$\times$100μm) spot size on the sample for experiments of X-ray absorption (XAS) and X-ray diffraction (XRD) [61]. The X-ray source is a 0.8 T bending magnet of the ESRF, which emission spectrum is reported in fig. 3.1. Relevant features of the ESRF storage ring and the GILDA beamline are reported in tables 3.1 and 3.2, respectively.

The beamline is constituted of four different lead shielded hutches. The first hutch, allocates the optical elements: monochromator, mirrors, beam monitors, filters, while the remaining hutches are dedicated to the experimental

Parameter	Units	Value
Electron Beam Energy	GeV	6
Max. Electron current	mA	200
Typical lifetime	hours	40
Horizontal emittance	10^{-9}mrad	4
Vertical emittance	10^{-12}mrad	30
Typical beam divergence at E_c	μrad	50
Brilliance at 10 Kev	ph/s/mm^2/mrad^2/0.1%BW	10^{20}
Brilliance at 60 Kev	ph/s/mm^2/mrad^2/0.1%BW	10^{19}

Table 3.1: ESRF main technical data.

Parameter	Units	Value
Bending magnet	T	0.8
Source dimensions (H×V)	mm^2	0.187×0.128
Source divergence (H×V)	μrad^2	115×5
Emitted power at the front end	W	225
Power density at 25 m	W/mm^2	0.83
Beam dimensions at 25 m (H×V)	mm	90×3
Horizontal acceptance	mrad	3.6
Spot size (H×V)	mm	2×1
Spectral range	KeV	5-85
Energy resolution		10^{-4}-10^{-5}
Peak brilliance	ph/s/mm^2/mrad^2/0.1%BW	$7{\cdot}10^{13}$
Flux on the sample	ph/s/mm^2/mrad^2/0.1%BW	$10^8 - 10^{11}$
Critical energy ε_c	KeV	19.8

Table 3.2: GILDA station main technical data.

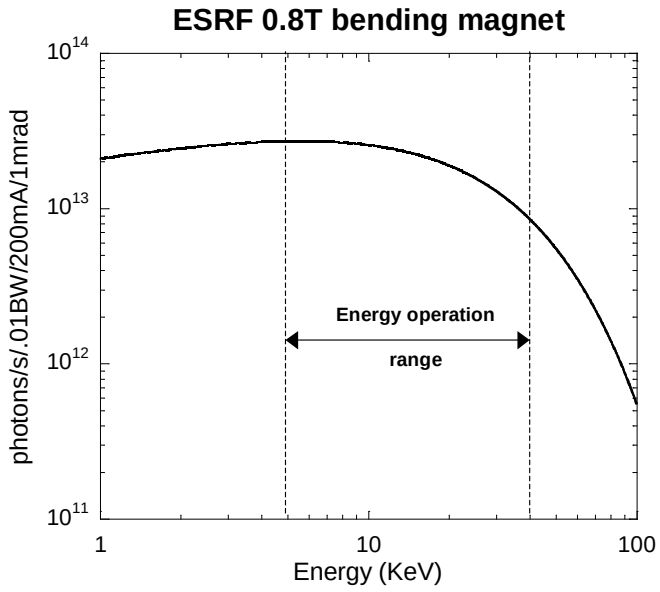

Figure 3.1: X-ray emission from a typical ESRF bending magnet equal to the one installed on the GILDA beamline.

stations.

The first experimental hutch is dedicated to absorption experiments. Two vacuum chambers are used for transmission and fluorescence experiments and can allocate different sample environments, allowing low temperatures (down to 4.2 K) and high temperatures (up to 550K) measurements with the possibility of *in situ* treatments of the sample. The same hutch also allocates XAS experiments in total reflection mode (ReflEXAFS).

In the second hutch a scattering apparatus based on a translating imaging plate allow to perform time resolved powder diffraction measurements with medium resolution (FWHM$\approx 0.05^o$).

The third experimental hutch is dedicated to non standard experiments and allocates an ultra high vacuum chamber (UHV). The beamline is isolated from the storage ring by a beryllium window; the beam outcoming the storage ring is defined in size and shape by a couple of vertical and horizontal slits located at the beginning of the hutch. The total power on the optical

elements is reduced using suitable filters: carbon, aluminium, and copper lamina of different thickness. All the optical elements exposed to the white beam are water cooled, to avoid thermal deformation. A cylindrical mirror is placed before the monochromator to collimate the diverging incoming beam in a parallel one. It also serves to reject higher harmonic contribution. A second mirror, located after the monochromator, focuses the beam on the sample in the vertical direction. Two different coatings, Pt and Pd, are deposited on the mirror's surface along two stripes parallel to the path of the beam. It is possible to move the mirrors horizontally in order to use one of the two coatings, which harmonic rejection efficiency is energy dependent (fig. 3.2). The incident angle of the mirrors is typically 3mrad.

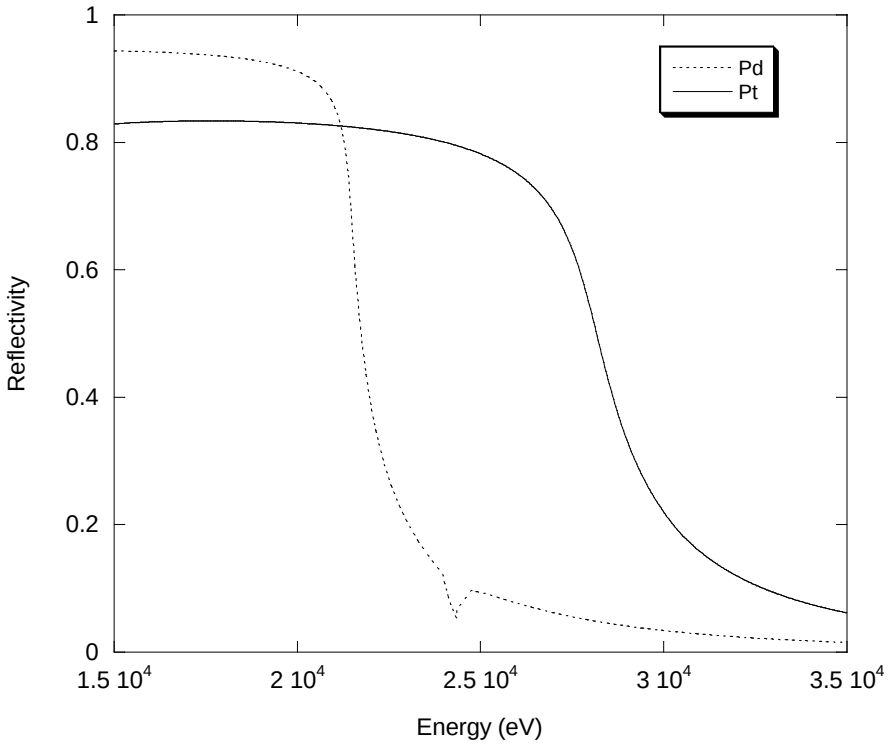

Figure 3.2: Pd and Pt reflectivity calculated at an incident angle of 3 mrad.

The optical system is designed to work in two different configurations: a low

energy configuration (less than 30 KeV), which uses mirrors, and a high energy one, without mirrors. In the latter configuration the energy resolution depends mainly on the primary slits vertical width, which determines the divergence of the white beam entering the monochromator. In this case, harmonic rejection can be achieved by detuning the angle between the monochromator crystals. This technique is based on the fact that harmonics have a smaller Darwin width than fundamental. [1]. In fact, in the case of scattering perpendicular to the orbit plane (S-polarized wave) the Darwin width ω_s of a perfect crystal at a wavelength λ is given by:

$$\omega_s = \frac{2}{sin2\theta_B}\frac{r_e\lambda^2}{\pi V}|F_{hkl}|^2 e^{-M} \tag{3.1}$$

where r_e is the classical electron radius, V is the crystal unit cell volume, θ_B the Bragg angle, F_{hkl} the crystal factor that depends on the Miller indices hkl and on the Bragg law ($sin2\theta_B/\lambda$), and e^{-M} a factor that takes in account the effect of the thermal effect. In this way a slightly misalignment of one monochromator crystal with respect to the other, a little bit more than the 3rd harmonic rocking-curve width, do not reduce the fundamental but the harmonic almost disappear.

A second couple of mirrors is used to reject harmonic contribution at low energy (< 8 KeV).

[1] Intuitively, this can be understood recalling that the crystal acts as a diffracting grating and the resolution of such a device depends on the number of the diffracting elements. In Bragg condition, the beam path in the crystal is limited by the diffraction process, so the number of planes participating to the constructive interference is limited. This gives rise to the non zero width of the reflectivity curve (the, so called, rocking-curve). The penetration length, called "extinction length", depends on the scattering factors of the material: the higher the scattering factor the stronger the diffusion of the beam. In the case of the reflection of an harmonic the angle is identical but the exchanged momentum is much larger so the material scattering factor is lower. This means a longer extinction length, an higher number of diffracting elements thus an enhanced resolution of the "grating"

The hearth of the optical system is the fixed exit, sagittal focusing monochromator constituted of two independent silicon crystals. The first crystal is flat and water cooled while the second is cylindrically bendable. Si(111), Si(311) and Si(511) crystals are used to cover the whole energy range ($5 - 50$ KeV) with the required energy resolution. The angle of the first crystal is finely controlled by a μrad precision piezoelectric actuator having an angular range of 100μrad. The angle is continuously adjusted by the means of an analogical proportional, integral, derivative (PID) feedback system which reads a beam detector (ion chamber) after the monochromator and compares the output signal with a set-point level. The relative angle between the first and second crystal is changed by this system in order to keep fixed the output intensity. To maintain the exit beam at a constant height, the second crystal moves along the beam direction, as a function of the energy, by the means of a bent driven actuator. The second crystal is diamond shaped in order to be cylindrically bent for the horizontal (sagittal) focusing of the beam (fig. 3.3).

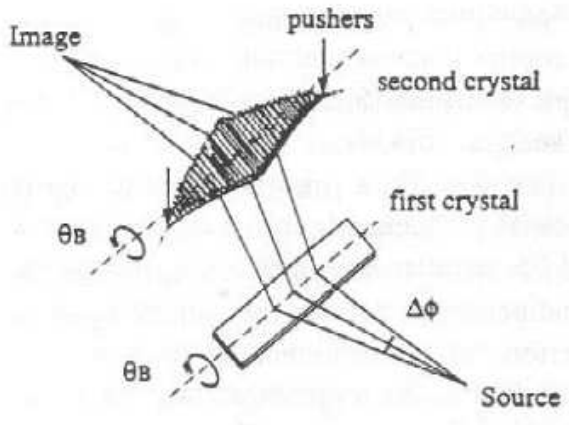

Figure 3.3: Representation of the sagittal focusing.

Energy resolution

The resolution of a monochromator depends both on the intrinsic crystal resolution (at its turn depending on the crystal and on the chosen diffracting planes) and on the divergence of the incoming beam, $\Delta\psi_{in}$. In the case of small source, being ΔE_{int} the intrinsic resolution, L the source to slits distance and h the slits half-width, the resolution $\Delta E/E$, when working at an angle θ_B is given by:

$$\begin{aligned} \Delta E/E &= \sqrt{\Delta E_{int}^2 + \cot^2\left(\theta_B \cdot \Delta\psi_{in}\right)} \\ \Delta\psi_{in} &= \frac{h}{L} \end{aligned} \tag{3.2}$$

This is true as long as the slits determine the beam divergence. Placing a focusing mirror, with its focus in the source, behind the monochromator, the diverging beam is converted in a parallel beam and the slit aperture has no more influence on the incoming divergence. This is true for ideal components; in the real life the source dimension, the shape errors of the mirrors and the bumps generated by the thermal load, limit the minimum theoretical divergence of the beam after the mirror.

3.2 X-ray absorption apparatus

Fig. 3.4 shows the simplest detection scheme for XAS measurements: the transmission mode. The X-ray flux impinging on the sample and the transmitted flux are directly measured using two ionization chambers. The first chamber, placed before the sample, measures the incoming beam (I_0) and is usually settled to absorb 20% of the beam. The second ionization chamber is placed downstream the sample and is usually settled up to absorb 80% of the transmitted photons (I_1); such percentages are chosen to enhance the S/N ratio. In order to absorb the correct percentage, ionization chambers are

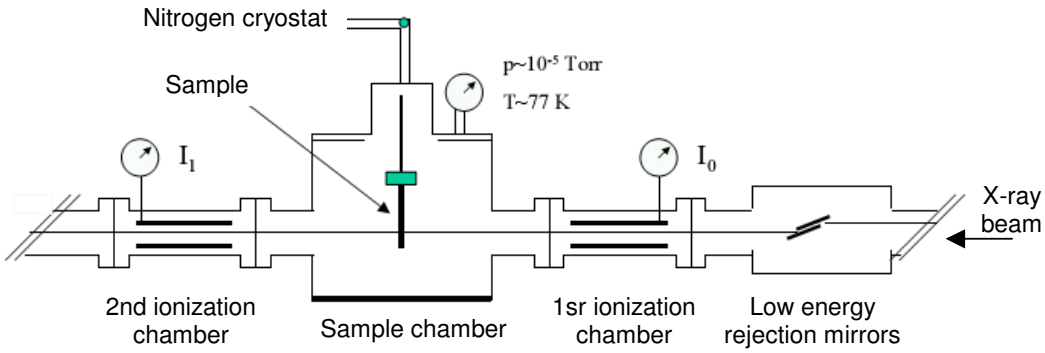

Figure 3.4: Sketch of the experimental hutch dedicated to absorption experiments in transmission and fluorescence mode. Two vacuum chambers are installed in this hutch and can be equipped with a nitrogen or helium cryostat. A ion chamber is placed before the experimental chambers to measure the incoming beam while a second ion chamber, placed after the vacuum chambers, serves to measure the outcoming beam.

filled with different gases (nitrogen, argon, krypton) at different pressures, depending on the working energy.

Transmission measurements are fast and accurate if concentrate, sufficiently thin and homogeneous samples are available. If the sample absorbs too much or the concentration of the absorber species is too low the signal to noise ratio becomes low. In these cases it is more convenient to measures indirect phenomena related with the photon absorption, such the fluorescence or electron yields sketched in fig. 3.5.

The photoionization process (fig. 3.5) (a) leaves the atom in an excited state, with a core hole that is suddenly filled by the transition of another electron from higher energy levels. Multiple de-excitation process can occur. A radiative process, giving rise to the fluorescence yield, occurs when an electron falls from an higher energy state to the ionized one emitting a photon (fluorescence photo, fig. 3.5(b)). Alternatively, a non-radiative process, occurs when the hole filling is accompanied by the emission of a fast electron to balance the energy difference (Auger electron); this second process (fig. 3.5(c))

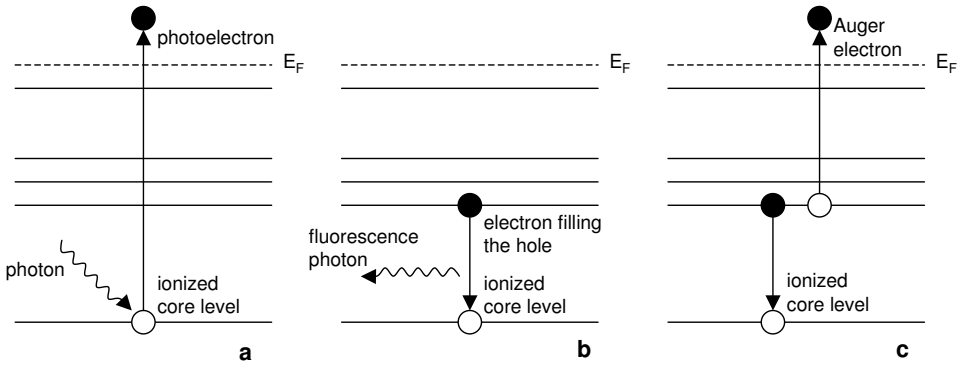

Figure 3.5: Schematic view of (a) photoionization process, (b) the radiative decay of the core hole via a fluorescenze photon and (c) the non-raidative decay via an Auger electron.

gives rise to the electron yield. For light atoms the Auger effect is more probable, while for heavy atoms fluorescence emission becomes more likely (fig. 3.6). The relative weight of the two processes is measured by the fluorescence yield:

$$\eta_s = \frac{X_s}{X_s + A_s} \tag{3.3}$$

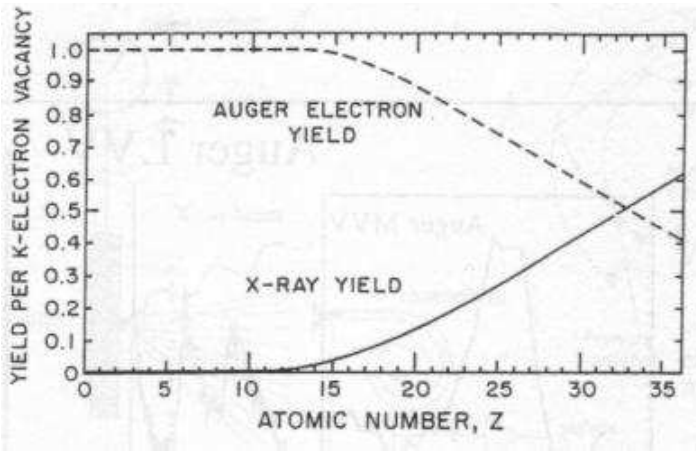

Figure 3.6: Calculated Auger electron and X-ray yields per K vacancy as a function of atomic number (Siegahn et al.)

where X_s and A_s are the decay rate of emission of one fluorescence photon

or Auger electron.
Under definite conditions, the decay rate of a fluorescence/Auger process, being proportional to the number of hole created, results proportional to the absorption coefficient of a particular species.
A more detailed discussion of the electron yield method (Total Electron Yield, TEY) will be given in the next chapter.

3.3 X-ray Absorption

Consider a monochromatic X-ray beam passing through a material of thickness x:

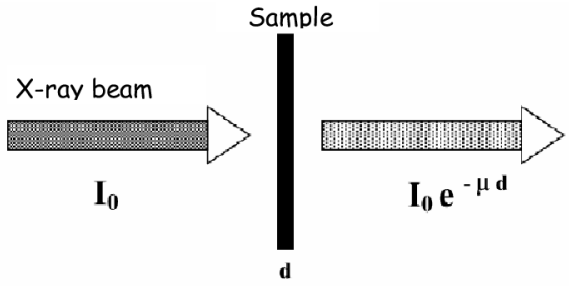

Figure 3.7: Attenuation of an X-ray beam passing through a material of thickness d.

the transmitted intensity is reduced with respect to the incident one according to the equation:

$$I = I_0 e^{-\mu x} \tag{3.4}$$

where μ, the linear absorption coefficient, depends on the photon energy, the density and the atomic species constituting the absorbing system. The general trend of μ with energy is a decreasing one, interrupted only by abrupt discontinuities that represent specific absorption edges corresponding to the

binding energies of deep electronic levels (Fig.(3.9)). Absorption edges corresponding to the extraction of an electron from the deepest level ($1s$), are those having the highest energy and are called K-edges. In the following table we report, in order of decreasing energies, the names of the edges together with the corresponding electronic core levels:

Edges:	K	L_1	L_2	L_3	M
Levels:	1s	2s	$2p_{1/2}$	$2p_{3/2}$	3s

The energy of the absorption edges are characteristics of atomic species and increase with the Z number as shown in Fig.(3.8).
From eq.(3.4) one can express the absorption coefficient in terms of the beam intensities before and after the sample as:

$$\mu(\omega) = \frac{1}{x} \ln \frac{I_0}{I}. \tag{3.5}$$

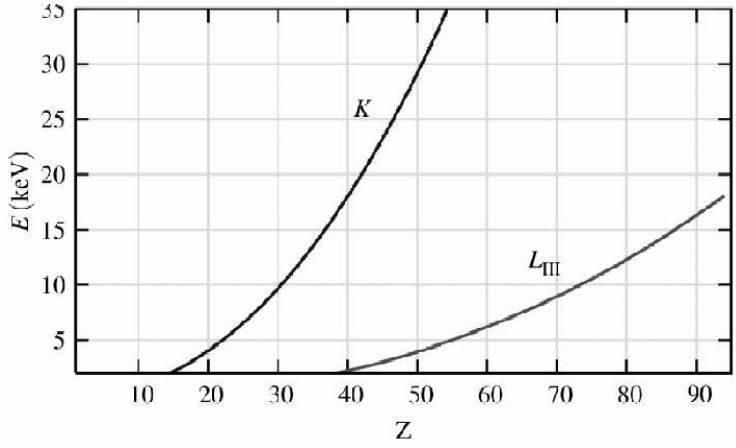

Figure 3.8: Binding energy at the K- and L_3-edge as a function of the atomic number Z.

For a monoatomic substance, $\mu(\omega)$ is correlated to the atomic absorption cross section $\sigma_a(\omega)$ by:

$$\mu(\omega) = \frac{\sigma_a(\omega) N_a \rho}{A} \tag{3.6}$$

where N_a stands for the Avogadro's number while ρ and A are the mass density and the atomic weight of the absorber respectively.

For a chemical compound $P_x Q_y ...$ the total absorption mass coefficient can be expressed as:

$$\left(\frac{\mu(\omega)}{\rho}\right)_{tot} = x \left(\frac{\mu(\omega)}{\rho}\right)_P \frac{A_P}{M} + y \left(\frac{\mu(\omega)}{\rho}\right)_Q \frac{A_Q}{M} + ... \tag{3.7}$$

where M is the molecular weight of the compound, A_i are the atomic weights of the constituent elements.

With increasing photon energy the absorption coefficient μ progressively decreases (Fig.(3.9)). For energies in the range 1-30 keV above an absorption edge the trend is generally well described by the empirical Victoreen relation:

$$\frac{\mu(\omega)}{\rho} = C\lambda^3 - D\lambda^4 \tag{3.8}$$

where C and D are functions of the atomic number Z.

When an absorption edge occurs the absorption coefficient increase abruptly, from a value μ_{inf}, up to an higher value μ_{sup}. The difference $\delta\mu = \mu_{sup} - \mu_{inf}$ represents the absolute contribution to the absorption associated to the excitation of a specific core level. The relative absorption can be expressed as $(\mu_{sup} - \mu_{inf})/\mu_{sup} = 1 - 1/r$ where $r = \mu_{sup}/\mu_{inf}$ is the so-called *jump ratio*.

3.4 X-Ray Absorption Fine Structure Spectroscopy

The term X-ray Absorption Fine Structure (XAFS) refers to oscillations in the absorption coefficient that occur above the absorption edge of a given

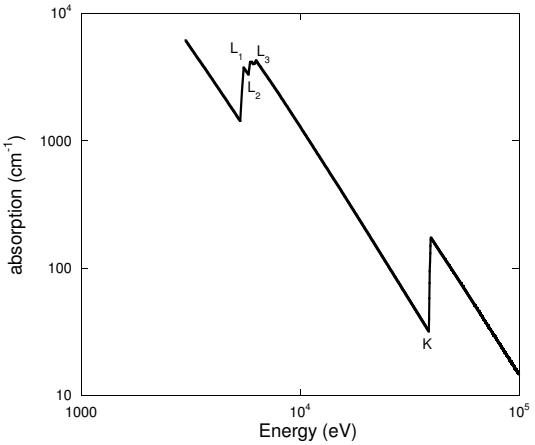

Figure 3.9: Absorption coefficient evidencing the discontinuities associated to K-, $L_{1,2,3}$-edges.

atomic species (fig. 3.10). Such oscillations, first observed in 1931 [19], can extend up to 1000 eV above the edge, may have a magnitude of 10% of the absorption jump (see Fig. 3.10) and are not present in the gaseous phase. According to different physical phenomena occurring and to different theoretical interpretation schemes, an absorption spectrum is usually divided into three main regions (fig. 3.10):

- the *pre-edge region*, limited to a few eV around the edge energy (E_b), dominated by the effects of transitions to localized electronic states, multipole transitions; it is very sensible to the details of the atomic potential;

- the energy region near the edge (*Near-edge Region)*), extending up to a few tens of eV above the edge. The fine structures (named XANES, X-ray Absorption Near Edge Structure) present in this region are dominated by multiple scattering processes of photoelectrons emitted with low kinetic energy. XANES contain information on the electronic struc-

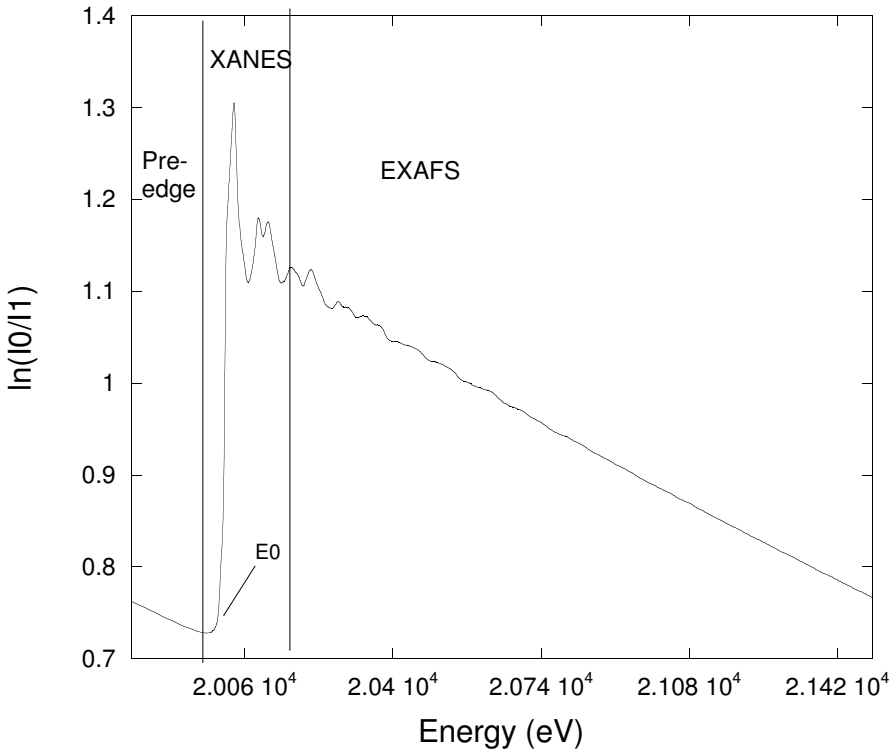

Figure 3.10: Absorption K-edge of the Mo atom (E_0 = 20000 eV). Post-edge EXAFS oscillations are evident compared to the smooth pre-edge and far post-edge atomic background.

ture of the investigated samples and on the geometric symmetry of the absorbing site;

- the energy region, starting from about 40-50 eV above the edge is named the *Extended Region*. The fine structures features constitute the EXAFS signal (Extended X-ray Absorption Fine Structure) and contain information on the atomic local structure around the absorber atom. The interpretation of EXAFS is generally simpler and much more consolidated than that of XANES.

It took a long time to achieve a coherent physical explanation of the EXAFS structures. At the very beginning both a short range order theory [19], ac-

cording to which oscillations were due to the modification of the final state wave function of the photoelectron caused by back scattering from the surrounding atoms (Fig. 3.11), and a long range order one [4], which considered the energy gaps at the Brillouin zone boundaries, were proposed.

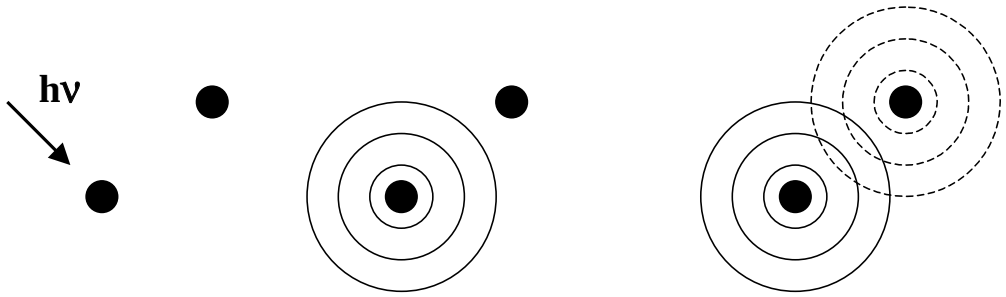

Figure 3.11: Pictorial representation of the EXAFS phenomena: a photon with energy equal or greater to the core absorption edge hit the absorber atom (left). The photoelectron extracted from the inner shell is represented by a wave function (center, solid circles). The photoelectron is backscattered by the surrounding atoms (right, dashed circles). The incoming and outcoming wavefunctions give rise to constructive and destructive interferences, which turns out to modulate the absorption coefficient in the way shown in fig. 3.10.

The long range order approach was shown to be in error, but only 40 years after [85] the first observation of the phenomenon; the long delay was due to the fact that, at the beginning, predictions made with the both theories didn't match well the experimental data. The first breakthrough occurred in 1971, when Sayers et al. [79] pointed out that a Fourier transform of XAFS with respect to the photoelectron wave number should peak at distances related to the atomic neighbors of the absorber. This discovery disclosed the possibility to extract from the XAFS structural information, like bond distances and coordination numbers. It also clarified the short range order origin of the effect, since the transform revealed only the first few shells of neighbor atoms. The second breakthrough was the availability of Synchrotron Radiation Sources, that delivered X-ray intensities orders of magnitude greater

than rotating anodes, and reduced the time for acquiring a spectrum on a concentrated sample from one week to the order of minutes. Nowadays it is established that a single scattering short range order theory is adequate under most circumstances, if we exclude the energy range immediately above the edge (up to about 30 eV). In this range, which is referred to as XANES region (acronym for X-ray Absorption Near Edge Spectroscopy), the energy of the photoelectron is very small (its wavelength being comparable with the interatomic distances), while its mean free path is quite high (some tenths of Å); as a consequence the probability for the photoelectron to be scattered from more than one atom in the surroundings of the absorber increases. XAFS, with the use of state of art analysis tools, provides information on the local structure around the absorber which is energetically selected; by using this technique it is possible to measure the bond lengths distribution and to determine the number of neighbors of the absorber. In some particular case, XAFS permits also to identify unknown neighbors and/or to measure the relative number of different neighbors in a mixed shell and to estimate the structural disorder of the lattice with respect to a model that takes into account both the not distorted theoretical lattice and the phonon behavior. It can provide information on the bond angles and on the geometry of the photoabsorber site, by studying multiple scattering and exploiting the polarization dependence. As a result, XAFS has become a very important investigation technique in different scientific fields, such as physics, material science, chemistry, biology and biophysics; the local character of the probe made it complementary to X-Ray Diffraction, which provides on the contrary information on the long range order.

3.4.1 Standard EXAFS formula

The linear absorption coefficient μ represents the reduction in the energy density u carried by the electromagnetic field, due to the interaction with

the material. It can be also expressed as :

$$\mu(\omega) = -\frac{1}{u}\frac{du}{dx} \tag{3.9}$$

where

$$u = \frac{\varepsilon_0 E_0^2}{2} = \frac{\varepsilon_0 \omega^2 A_0^2}{2} \tag{3.10}$$

and A_0 is the amplitude of the vector potential associated to the electric field, whose maximum amplitude is E_0 and ε_0 is the dielectric constant of vacuum. $\mu(\omega)$ depends on the atomic density of the sample n and on the probability of transition W_{fi} for the photoabsorber from the initial state $\mid \psi_i >$ to the different possible final states $\mid \psi_f >$, corresponding to possible different core holes or multiple excitations:

$$\mu(\omega) = \frac{2\hbar}{\varepsilon_0 \omega A_0^2} n \sum_f W_{if} \tag{3.11}$$

In order to calculate the probability of transition W_{fi}, the time dependent perturbation theory is exploited, which permits to expand in series the interaction potential between the atom and the electromagnetic field, and to use the only first term of the series if the interaction is weak. The transition probability is in this way determined by the Fermi's golden rule:

$$W_{fi} = \frac{2\pi}{\hbar} | < \psi_i \mid H_i \mid \psi_f > |^2 \rho(E_f) \tag{3.12}$$

where $\rho(E_f)$ is the final density of states and H_I is the interaction Hamiltonian operator for photoelectric absorbtion which, at the first order, can be written as :

$$H_I = i\hbar \frac{e}{m} \sum_j \overrightarrow{A}(\overrightarrow{r_j} \cdot \overrightarrow{\nabla_j}) \tag{3.13}$$

where j labels the electrons inside the atom and $\overrightarrow{\nabla_j}$ their linear momentum. By using equations 3.12 and 3.13, we find the probability of transition for the

photoelectric absorption of photons belonging to a monochromatic, polarized and collimate beam:

$$W_{fi} = \frac{\pi\hbar e^2}{m^2}|A_0|^2 < \psi_i \mid \sum_j e^{i\overrightarrow{k}\overrightarrow{r_j}}\hat{\eta}\cdot\overrightarrow{\nabla_j}\mid \psi_f >|^2\rho(E_f) \tag{3.14}$$

$\hat{\eta}$ and $\overrightarrow{k}$ are the polarization unity vector and the electric field vector ($k = 2\pi/\lambda$). If we use the first order term of the series expansion for the exponential, we obtain the transition probability in the dipole approximation (valid for $|\overrightarrow{k}\overrightarrow{r_j}|^2 \ll 1$):

$$W_{if} = \frac{\pi\hbar e^2}{m^2}|A_0|^2| < \psi_i \mid \sum_j \hat{\eta}\cdot\overrightarrow{\nabla_j}\mid \psi_f >|^2\rho(E_f) \tag{3.15}$$

If we substitute the momentum with the position operator :

$$W_{if} = \frac{\pi e^2}{\hbar m^2}|A_0|^2| < \psi_i \mid \sum_j \hat{\eta}\cdot\overrightarrow{k_j}\mid \psi_f >|^2\rho(E_f) \tag{3.16}$$

In the dipole approximation the following selection rules are valid for the angular momentum:

$$\Delta l = \pm 1;\ \Delta s = 0;\ \Delta j = \pm 1, 0;\ \Delta m = 0 \tag{3.17}$$

If the transition involves only one electron, the first rule implies that, in case of symmetry s (i.e. $l = 0$) for the initial state, the final state has p symmetry (i.e. $l = 1$). This is the case of all the edges (K) investigated in this thesis work. In order to calculate the transition probability of equation 3.16 and hence the absorption coefficient, it would be necessary to know the final state $\mid \psi_f >$ (the initial state is simply the fundamental state of the absorbing atom). This is a priori difficult, since the final state involves all the electrons in the atom and, furthermore, it is perturbed by the local environment of the absorber. An approximation used to simplify the situation is the single electron one, based on the fact that a large fraction $\mu_{el}(\omega)$ of the absorption

coefficient is due to transitions where only one electron modifies its state and the others $N-1$ just relax their orbitals to accomplish the new potential created by the presence of a core hole. The remaining fraction of μ is due to inelastic transitions, where the excitation of the primary core electron takes to the excitation of more external electrons, which can occupy higher energy states (*shake up* process) or leave the absorber atom (*shake off* process); the photon energy is in this case shared by all these excited electrons. The absorption coefficient, following this approximation, can be written as :

$$\mu(\omega) = \mu_{el}(\omega) + \mu_{anel}(\omega) \tag{3.18}$$

$$\mu_{el}(\omega) \propto | < \psi_i^N \mid \hat{\eta} \cdot \overrightarrow{r} | \; \psi_f^{N-1} \psi_f > |^2 \; \rho(\varepsilon_f) \tag{3.19}$$

where ψ^{N-1} is the Slater representation for the wave functions of passive electrons while ψ, $\overrightarrow{r}$ and ε_f are the wave function, position vector and final energy of the active electron. If the photoelectron has sufficiently high kinetic energy, it takes such a short time in leaving the absorber atom that its motion is not affected by the slower relaxation of the passive electrons [41]. In this case, we can separate the contribution of the active and passive electrons in the initial and final wave functions (*sudden approximation*):

$$\mu_{el}(\omega) \propto S_0^2 | < \psi_i \mid \hat{\eta} \cdot \overrightarrow{r} | \; \psi_f > |^2 \; \rho(\varepsilon_f) \tag{3.20}$$

where:

$$S_0^2 = | < \psi_i^N | \; \psi_f^{N-1} > |^2$$

S_0^2 represents the overlap integral of the passive electrons wave functions in the initial and final states. The sudden approximation, which reduces the calculation of the final state to the final state for the photoelectron only, is rigorous starting from some tenth of eV above the edge. In general S_0^2 varies

between 0.7 and 1, and can be experimentally determined by measuring a standard compound with local environment similar to that of the sample under investigation, as has been done during this work when possible. If there is no relaxation of the $N-1$ electrons, i.e. if $S_0^2 = 1$, $\mu_{el}(\omega)$ in equation 3.20 has to be equal to $\mu(\omega)$ of equation 3.18: this means that S_0^2 measures the fraction of absorption due to the only elastic transitions.
The XAFS function is defined as:

$$\chi(E) = \frac{[\mu(E) - \mu_0(E)]}{\Delta\mu_0} \tag{3.21}$$

where $\mu(E)$ is the smooth atomic background absorption, which can be simulated by a spline, and $\Delta\mu_0$ is the jump in the absorption coefficient at the edge. Since in the Extended-XAFS region (EXAFS) (starting from about 30 eV above the edge) the final density of states varies slowly and monotonically with energy, the oscillations contained in $\chi(E)$ come only from the matrix element. Different derivations for the single scattering XAFS formula have been proposed (see for example ref. [41]); they normally use a Muffin Tin approximation for the atomic potential, i.e. radial inside a sphere surrounding each atom and constant between the atoms. Even if this approximation is quite crude, it works well in the EXAFS region, where the high energetic photoelectron is essentially scattered by the inner part of the potential and moves almost freely in the interstitial region [68]; the high energy makes it less sensitive to the potential details. If spherical photoelectron wave functions are employed, the single scattering XAFS formula, as a function of the photoelectron wave number $k = \sqrt{2m(E-E_0)/\hbar^2}$, is:

$$\chi(k) = -3\ S_0^2(k) \sum_j \frac{N_j}{kR_j^2}\ |f_j(k,R)|\ \sin\left(2kR_j + 2\delta_c(k) + \phi_j(k,R_j)\right) \\ e^{-2k^2\sigma_j^2} e^{-2R_j/\lambda_j(k)} (\widehat{\eta}\cdot\widehat{R_j})^2 \tag{3.22}$$

The sum is performed over j-different atomic shells which contain each N_j

identical neighbors; in case of mixed shells, linear combinations have to be used. R_j is the vector which links the absorber to the j-neighbors, $|f_j(k, R_j)|$ is the modulus of the backscattering function of the atoms in the shell j, while $|f_j(k, R_j)|$ is its phase; in the spherical wave-approach they depend on R_j. $\delta_c(k)$ is the phase shift of the photoelectron wave induced by the central atom, this phase shift is counted twice (first while the photoelectron leaves the atom and second when it come back after been scattered from the neighbors). $e^{-2k^2\sigma_j^2}$ is the Debye-Waller factor which measures the broadening of the distances distribution, σ_j^2 being the mean square fluctuation of the bond lengths ($\sqrt{(R_j - \bar{R}_j)^2}$). If the distribution of the distances is gaussian (*harmonic approximation*), σ_j^2 can be expressed in terms of vibrational normal modes using the Debye's or Einstein's models [82].

$\lambda_j(k)$ measures the mean distance covered by the photoelectron before losing coherence with its initial state; it causes a damping in the XAFS amplitude since only photoelectrons which do not lose coherence with the initial state give a contribution to the signal. The relative lifetime is $\tau = \lambda/\nu$, where ν is the speed of the photoelectron; the lifetime can be written as the sum of two contributions :

$$\frac{1}{\tau} = \frac{1}{\tau_h} + \frac{1}{\tau_e} \tag{3.23}$$

The first is related to the core hole life time and diminishes with increasing atomic numbers, since the number of possible final states increases; this term is energy-independent. The second contribution is related to the photoelectron and is due to inelastic interaction with electrons of the absorber neighbors; this term is energy-dependent.

The product $\widehat{\eta} \cdot \widehat{R_j}$ between the polarization and position unitary vectors takes into account the fact that the photoelectron is preferentially ejected in the direction of the field. For isotropic samples as polycrystalline powders, amorphous materials, or single crystals with a cubic symmetry, this product

can be substituted by the angular average 1/3 . As far as the photoelectron is sufficiently energetic and interacts only with the inner orbitals, we can consider the scattering centers as point-like and neglect the curvature of the spherical wave. As a consequence, the scattering process can be treated in the simpler plane-wave formalism, the complex backscattering amplitude can be expanded in series of partial waves and does not depend on R_j any more:

$$f(k,\pi) = \frac{1}{k}\sum_{t=0}^{\infty}(-1)^l\ (2l+1)\ e^{i\delta_l}\sin\delta_l \tag{3.24}$$

δ_l are the phase shifts of the partial waves.
In the *isotropic* and *small atom* approximation the single scattering XAFS formula becomes:

$$\chi(k) = -S_0^2(k)\sum_j \frac{N_j}{kR_j^2}\ |f_j(k,R)|\ \sin(2kR_j + 2\delta_c(k) + \phi_j(k,R_j))$$
$$e^{-2k^2\sigma_j^2}e^{-2R_j/\lambda_j(k)} \tag{3.25}$$

For non Gaussian distances distributions, the XAFS formula can be written in series of cumulants C_k; the odd cumulants determine the phase of the signal, while the even ones determine the amplitude. In this case the contribution to XAFS of the j-th atomic shell is:

$$\chi_j(k) = \frac{S_0^2}{k}N_j|f_j(k,\pi)|\exp(C_0 - 2k^2C_2 + \frac{2}{3}k^4C_4\cdots) \tag{3.26}$$

In the formulation of equation 3.26, relative to the *harmonic approximation*, S_0^2 can be determined by measuring a standard compound, $|f_j(k,\pi)|$ and $2\delta_c(k) + \phi_j(k)$ can be either calculated *ab initio* or extracted from standard compounds with similar local environment; $\lambda_j(k)$ can be also estimated. As a consequence three quantities remain unknown and can be determined by fitting the experimental data: the number of atoms for each shell N_j , the distances R_j and the Debye-Waller factors. Different approaches to the first

principles calculation of amplitudes and phases, and different fitting procedures were proposed in order to extract structural information.

3.4.2 The Debye-Waller factor

The Debye-Waller factor is one of the relevant physical quantities that can be obtained from an EXAFS analysis. Since the physical meaning of such a quantity is not trivial, while it returns very important structural information, it will be discussed more in detail in this paragraph.
The Debye-Waller factor measures the superposition of the thermal vibration of the lattice (the phonons) and of the structural disorder (if present). Since it appear in the standard EXAFS formula as a negative exponential, it contributes to dump the EXAFS signal. It depends on two linked parameters: the temperature and the atom displacement from their equilibrium position.

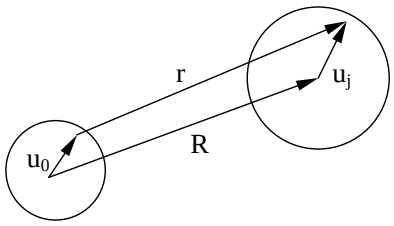

Figure 3.12: Relation between the instantaneous distance $\vec{r}$ and the thermal displacements $\vec{u}_0$ e $\vec{u}_j$

The equilibrium distance $\overrightarrow{R_j}$ is continuously modified by the displacement of the absorber and the back scatterer atoms $\overrightarrow{u_0}$ and $\overrightarrow{u_j}$, respectively (see fig. 3.12), its instantaneous value being:

$$\overrightarrow{r_j} = \overrightarrow{R_j} + \vec{u_j} - \vec{u_0} \tag{3.27}$$

which modulus can be expressed as:

$$r_j = |\vec{R}_j + \vec{u}_j - \vec{u}_0| = R_j \left(1 + 2\hat{R}_j \cdot \frac{\vec{u}_j - \vec{u}_0}{R_j} + \frac{(\vec{u}_j - \vec{u}_0)^2}{R_j^2}\right)^{1/2} \tag{3.28}$$

The relative displacement, $\Delta\vec{u}_0 = \vec{u}_j - \vec{u}_0$, can be separated in its component parallel and perpendicular to the direction of the interatomic bond. The parallel component is:

$$\Delta u_{\parallel} = \hat{R}_j \cdot (\vec{u}_j - \vec{u}_0) \tag{3.29}$$

while, the square of the perpendicular component is:

$$\Delta_{\perp}^2 = \Delta u^2 - \Delta u_{\parallel}^2 = (\vec{u}_j - \vec{u}_0)^2 - [\hat{R}_j \cdot (\vec{u}_j - \vec{u}_0)]^2 \tag{3.30}$$

Performing a series expansion on the last equation and neglecting higher order terms, the instantaneous distance can be expressed as:

$$r_j = R_j + \Delta u_{\parallel} + \frac{\langle \Delta u_{\perp}^2 \rangle}{2R_j} \tag{3.31}$$

In the case of harmonic lattices, in which the distances have a gaussian distribution centered on the equilibrium distance, it can be shown that $\langle \Delta u_{\parallel}^2 \rangle = 0$. Hence, the average value of the distance distribution is:

$$\langle r_j \rangle = R_j + \frac{\langle \Delta u_{\perp}^2 \rangle}{2R_j} \tag{3.32}$$

The Mean Square Relative Displacement of the distance distribution can be derived from the expression of the instantaneous distance. The largely predominant term is the first one in series expansion, usually indicated as σ^2:

$$\sigma_j^2 = \langle \Delta_{\parallel}^2 \rangle = \langle [\hat{R}_j \cdot (\vec{u}_0 - \vec{u}_0)]^2 \rangle \tag{3.33}$$

Expanding the square, the MSRD can be expressed as a sum of three terms:

$$\sigma_j^2 = \langle(\hat{R}_j \cdot \vec{u}_j)^2\rangle + \langle(\hat{R}_j \cdot \vec{u}_0)^2\rangle - 2\langle(\hat{R}_j \cdot \vec{u}_j)(\hat{R}_j \cdot \vec{u}_0)\rangle \tag{3.34}$$

The first two terms represent the Mean Square Displacement and depends in the amplitude of the displacement of the back scatterer and of the absorber, respectively. The last term is the Displacement Correlation Function and depends on the correlation of the motion of the two atoms. Contrary to EXAFS, diffraction, which is sensitive only to the long range order, is not affected by the correlation of nearest atoms, but only by the MSD. In Bravais lattices, σ^2 can be expressed in terms of normal vibration modes. Defining a density of modes $\rho(\omega)$ we obtain:

$$\sigma_j^2 = \frac{\hbar}{2\mu}\int \frac{d\omega}{\omega}\rho_j(\omega)\coth\left(\frac{\beta\hbar\omega}{2}\right) \tag{3.35}$$

where μ is the reduced mass for a absorber-back scatterer couple ω the frequency of the modes and $\beta = 1/kT$. Since in a EXAFS analysis one is usually interested in estimate the evolution of the structural disorder with the temperature (for example, while crossing a transition point), it become necessary to find a way to decouple the usual lattice phonon behavior from an eventual structural disorder contribution to σ. The usual phonon behavior as a function of the temperature can be approximated using the simple Einstein or Debye models modified for the EXAFS case [Beni-Platzmann]. The structural disorder contribution can be estimated by comparison with the phonon behavior or considering the latter as a background to be subtracted.

3.4.3 Data analysis

Extraction of the EXAFS signal

The procedure of EXAFS analysis, leading from the raw experimental data to the structural parameters determination, is complex and presents several tricky aspects. To extract the information from the absorption spectrum it

is necessary to follow steps dictated by theory but also by a large experience. XAFS data analysis usually follows three steps:

- first the XAFS function is extracted from equation 3.21;
- then an evaluation of the backscattering amplitudes and phase shifts is done using lattice models and dedicated codes;
- finally a fit of the data, varying some of the structural parameters, to the model equation 3.25 is performed.

The aim of the first step is to isolate the EXAFS oscillations in the K-space in order either to directly fit them using the standard equation (3.25) or to Fourier transform in the real space R and to perform the fit in this space. It is otherwise possible to back Fourier transform the data to the K-space in order to filter out all other frequencies except the ones included in the chosen transformation window. The analysis software exploited to obtain backscattering amplitudes and phase shift was the FEFF8 code, developed at the University of Washington, Seattle [3], while for the atomic background removal an home made FORTRAN code has been used. This program first performs a pre-edge background removal using a linear function (fig. 3.13 (a)); in this procedure most of the energy dependence of the absorption, other than that from the absorption edge of interest, is removed. Then the program carries out a normalization to the edge step (which can be manually imposed) and, finally, it performs a post-edge background removal (fig. 3.13 (b)). The last procedure consists in subtracting from $\mu(E)$ a smoothly varying background function $\mu_0(E)$ by the means of a series of polynomial splines, which approximate the absorption from the isolated embedded atom, obtaining in this way $\chi(E)$, the EXAFS signal (fig. 3.13 (c)). Fourier transform and back-transform of the EXAFS signal are illustrated in fig. (fig. 3.13 (d)) and (e)). The program permits to adjust a large variety of parameters

such as the the number of polynomial spline used to simulate the atomic background, their degree, the position of the knots (the points in which the splines connect), the value of the edge step and the way the first spline passes through the edge. The splines and their first two derivatives are required to be continuous at the knots and one degree of freedom is associated to each knot; the background function is not required to pass through the experimental curve at the knots. Since the spline substraction from the data is a quite arbitrary procedure this is the most tricky step, the one in which errors that can invalidate the results can occur. This step requires a large degree of experience and can be really dubbed to be a *trial&error* procedure.

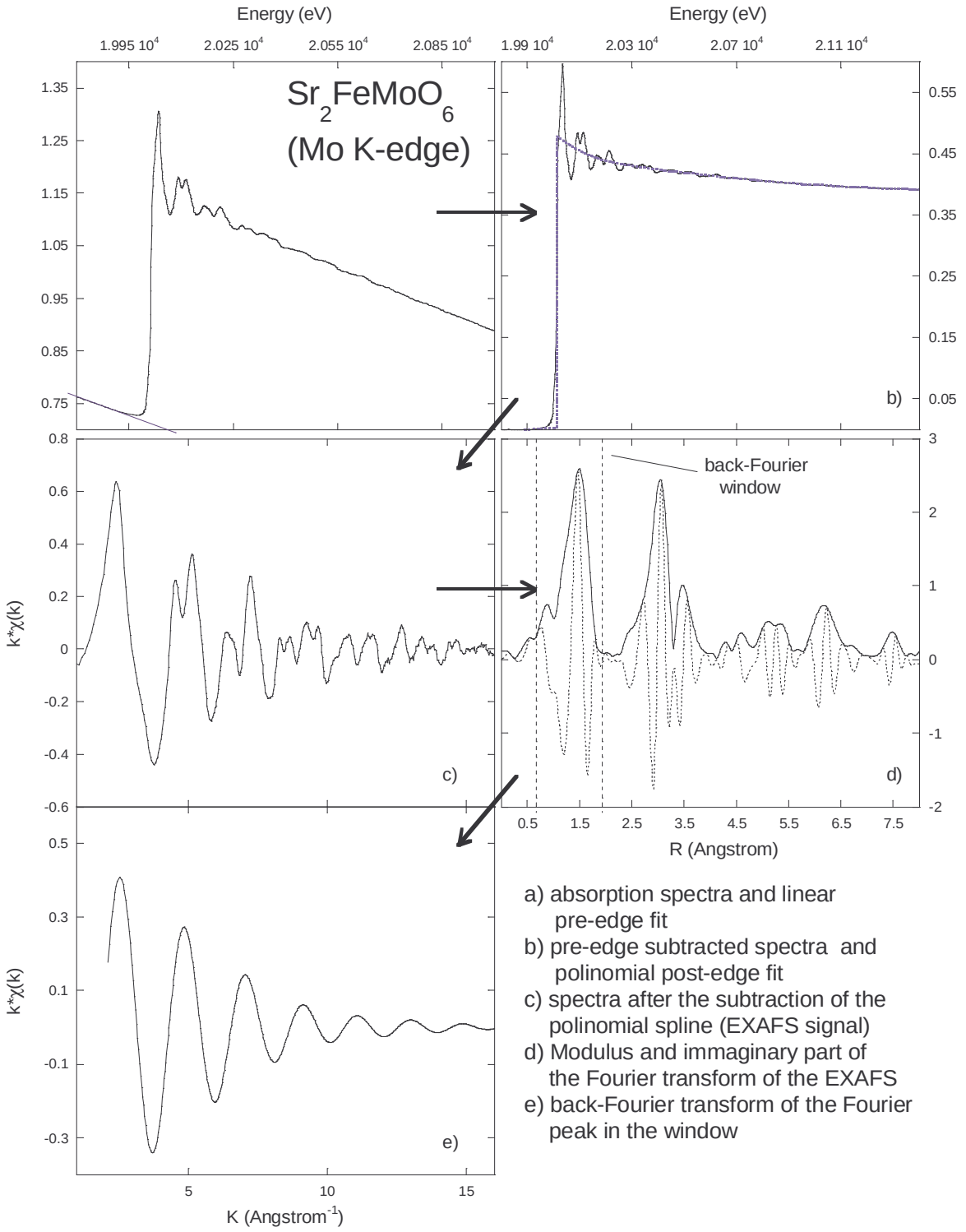
Energy (eV)
Energy (eV)
Sr2FeMoO6
(Mo K-edge)
b)
back-Fourier
window
c)
d)
e)
k*χ(k)
k*χ(k)
R (Angstrom)
K (Angstrom-1)
a) absorption spectra and linear pre-edge fit
b) pre-edge subtracted spectra and polinomial post-edge fit
c) spectra after the subtraction of the polinomial spline (EXAFS signal)
d) Modulus and immaginary part of the Fourier transform of the EXAFS
e) back-Fourier transform of the Fourier peak in the window

Figure 3.13:

Theoretical amplitude and phase backscattering functions

After background removal, all the atomic clusters which are useful for simulating EXAFS and single and multiple scattering signals are generated using the FEFF code [3]. Using the code ATOMS simulates from the IFEFFIT package [66], we can generate a cluster centered on the absorbing atom from the knowledge of lattice parameters and spatial groups. Atomic positions are read by the FEFF code, which perform an *ab initio* modeling of the absorption cross section and of the theoretical amplitude and backscattering functions.

Minimization

The theoretical amplitudes and phases generated by FEFF are successively exploited to construct a model function:

$$\chi_{model}(k) = \sum_{path}(k\ , Amp(k)\ , Phase(k),\ Path\ parameters) \tag{3.36}$$

which is fitted to the data. An home made external FORTRAN routine has been written to exploit one of the most tested and reliable minimization programs, the MINUIT code from CERN libraries [1]. This program is conceived as a tool to find the minimum value of a multi-parameter function and analyze the shape of the function around the minimum. It is possible to choose between various minimization routines (MIGRAD, MINIMIZE, SCAN, SEEK, SIMPLEX) and minimization strategies which helps to achieve a best fit. MIGRAD is considered the best minimizer routine for nearly all functions. Its main weakness is that it depends heavily on knowledge of the first derivatives, and fails if they are very inaccurate. SCAN is not intended to minimize and just scan the model function one parameter at a time retaining the best value after each scan. SEEK is a Monte Carlo based routine. SIMPLEX

is a multidimensional minimization routine which does not use first derivatives overriding problems eventually encountered running MIGRAD but is slower and does not give reliable information about parameters errors and correlation and cannot be expected to converge accurately to the minimum in a finite time. MINIMIZE simply calls SIMPLEX when MIGRAD fails and then calls MIGRAD again. A useful characteristic of MINUIT is the possibility to set limits on the allowed values for a given parameter which help to prevent the parameter from taking on unphysical values. Moreover, the external routine gives the possibility to set up links between the parameters. This is very useful to reduce the correlations when physical constraints between two or more parameters are known. As it will be shown, this method has been widely used in this work. For example, when refining the spectra of the doped compounds studied in this thesis work, two different atomic species can simultaneously occur at the same lattice site with different probability but with the overall constraint that the sum of the weight returns unity.
Both the experimental and theoretical signals are K-weighted, apodizated with a Gaussian window and eventually Fourier filtered in the R-space and back Fourier transformed; finally, a non-linear least square routine is exploited to find the best set of variables which minimizes the χ^2 statistic for the difference between the experimental and theoretical signals in the K-space. The minimization is performed in the K-space and the EXAFS function is parameterized as follow:

$$k \cdot \chi(k)_{theo} = \sum_i N_i \; S_0^2 \; \frac{A_i(k)}{R_i^2} \; \sin(2kR_i + \phi_i(k) + 3^{th}_{cumulant}) \\ \exp -[2k^2\sigma^2 + 4^{th}_{cumulant}] \; \cdot \; exp - \left[2k\gamma \left(k + \frac{\eta}{k}\right)^4\right] \qquad (3.37)$$

where the 3th and 4th cumulants, which are used in the case of non-Gaussian distribution, are defined as:

$$3^{th}_{cumulant} = \frac{4}{3}\, k^3 \cdot\ c3_i$$
$$4^{th}_{cumulant} = \frac{2}{3}\, k^4 \cdot\ c4_i^2$$

$c3$ and $c4$ are free parameters in the fit. $A_i(k)$ and $\phi_i(k)$ are the theoretical amplitude and phase backscattering functions calculated by FEFF. The last exponential takes into account corrections to the photoelectron life-time (γ and η) calculated by FEFF that can be then chosen to be a fittable quantity. The structural free parameters for each path are the path length (R), the coordination number (N) and the Debye-Waller factor (σ^2) and the third and the fourth cumulants (in the case of asymmetric distributions), while, the threshold energy shift (E_0) and an overall amplitude factor which includes S_0^2 are common to all paths.

We can choice to perform the minimization either directly in the K-space or in the back Fourier transformed K-space (usually dubbed q-space). Since the Fourier transform introduces numerical inaccuracies, mostly due to the limited range of the spectra which requires mathematical artifacts (as the signal windowing), when possible, i.e. when it is possible to reproduce well the main features of the experimental signal using few contributions, I have chosen to perform the minimization in the untransformed K-space avoiding the any Fourier transformation. This choice has a further advantage since the number of independent points, corresponding to the maximum number of free parameter allowed, results much higher. In the K-space the number of independent points is calculated as:

$$N_{ind} = N_{points} - N_{param} \tag{3.38}$$

where N_{points} is the number of experimental points of the extracted EXAFS signal and N_{param} the number of free parameters in the minimization. From

information theory ideas [114] we have that the number of independent points for a fit performed in the back transformed q-space is:

$$N_{ind} = \frac{2\Delta R \Delta k}{\pi} \tag{3.39}$$

where ΔR and Δk are the K- and R-range of useful data. Data having an high signal to noise ratio can extend above 20 Å^{-1} in the K-space. Usually the maximum value for K is around 18 Å^{-1}. Considering equation 3.39 the number of parameters that can be left free in the minimization procedure is usually around 10. Since each path enters three or more free parameters in the fit (the path distance R, the path multiplicity (N) and the Debye-Waller (σ^2)), for fits including more than the first coordination shell, it become necessary to reduce the free parameters by fixing or by imposing constraints between the parameters. This is necessary also considering that parameters like the coordination number and S_0^2 are strongly correlated between each other and with the Debye-Waller (σ^2). Another set of correlated parameters are the energy shift E_0 the path distances R_j. Finally, all parameters have a certain degree of correlation due to constructive or destructive interferences which occurs when summing the sinusoidal contributions from each path having different frequencies. These interferences tend to modulate the amplitude of the EXAFS oscillations resulting in a link between the two set of parameters listed above, which are otherwise uncorrelated.

When possible, S_0^2 is determined measuring a standard compound and kept fixed during the fit. A global E_0 variable is used to adjust the experimental energy mesh to the theoretical one. The coordination number is kept fixed whenever the number of near-neighbors is known. Cumulants beyond the second are used only in case of strong disorder or asymmetric bond distances distribution.

Errors

Parameter errors are calculated exploiting MINUIT dedicated routines and following suggestions of the International XAFS Society - Standards and Criteria Committee (IXS - SCC), which proposes the following model as a starting point for any error assessment:

$$(\Delta\chi)^2 = W\frac{\sum_{i=1}^{N}|Data_i - Model_i|^2}{\epsilon_i^2} \tag{3.40}$$

W is a dimensionless factor described below, and ϵ_i is the measurement uncertainty for the i-th data point. This equation applies to both non-k-weighted data and k-weighted data, provided the data, model, and errors are weighted in the same manner. The functional 3.40 is analogous, but is not identical, to the standard statistical χ^2 function. The following essential points should be borne in mind:

- The points $Data_i$ and $Model_i$ may be represented in E, k, or R-space. In each case the measurement uncertainty ϵ_i should be calculated and normalized accordingly, as discussed below.

- For E-space (raw data) fits, W may be taken as 1. In this case, intrinsic limitations on the number of adjustable parameters become apparent through analysis of the covariance matrix. In *ab initio* fitting it should be stressed that these intrinsic limits are the same as in k- and r-space fitting, whether Fourier filtered or not. The energy range for the fit determines a Δk, and the number of shells included in the fit determines a ΔR, which together limit the number of parameters that can be determined.

- For R-space fits $W = N_{ind}/N$, where N is the number of complex data points contained within the range of the fit.

- For back transformed k- and R-space fits, $W = N_{ind}/N$, and N_ind is approximately given by 3.39, rounded off to the nearest integer.

- The r.m.s. measurement error:

$$\epsilon^2 = \sum_i \epsilon_i^2/N \tag{3.41}$$

  may be used in Eq. 3.40 instead of the individual ϵ_i, as in the case of the code used in this work.

- If $\Delta\chi^2$ is defined as in Eq. 3.40, a fit can be considered acceptable when $\Delta\chi^2 \sim \nu$, where $\nu = N_{ind} - N_{param}$ is the number of degrees of freedom in the fit.

It is necessary to define a normalization factor for eq. 3.40, i.e. the value ϵ defined in eq. 3.41 representing the statistical error. The Minuit error on a parameter is defined as the change of parameter which would produce a change of the function value equal to the normalization factor. This factor can be obtained in various ways, the most common of which being:

- Subtracting a smoothed function $\chi'(k)$ from the background-subtracted experimental $\chi(k)$ data. The statistical component of the error may then be calculated for each point as:

$$\epsilon_i^{statistical} = \chi_i(k) - \chi_i'(k) \tag{3.42}$$

  The average statistical error should be estimated from the r.m.s. value of 3.41 over data segments with similar statistical weight, e.g., over segments with a constant integration time. The smoothed data $\chi'(k)$ may be obtained either by smoothing with a low-order polynomial, or with low-pass Fourier filtering.

- From the r.m.s amplitude of the R-space transform in a region devoid of structural features. If the statistical noise is truly white, the amplitude of its spectrum in R-space can be adequately approximated by a single number, ϵ_R, which is related to the rms. noise amplitude in k-space, ϵ_k, by Parseval's theorem:

$$\epsilon_k = \epsilon_R \sqrt{\frac{\pi(2w+1)}{\delta k(k_{max}^{2w+1} - k_{min}^{2w+1})}} \tag{3.43}$$

  Here ϵ_R is the r.m.s. noise amplitude in the k-weighted R-space spectrum, ϵ_k is the r.m.s. noise amplitude in the unweighted k-space spectrum, w is the k-weight of the transform, the transform range is $[k_{min}, k_{max}]$, and δk is the spacing of the points in k-space. The above formula assumes that an Fast Fourier Transform (FFT) with equidistant k-space points is used, and the forward and back transforms are normalized by $\sqrt{\delta k/\pi}$ and $\sqrt{\delta r/\pi}$, respectively, which is a common XAFS convention. It should be noted that it is not possible to estimate the error point-by-point, as in Eq. 3.42.

The external routine written for MINUIT estimates the statistical error using this second method.
Confidence limits for the fit parameters are estimated from Eq. 3.40 using the covariance matrix C generated by MINUIT:

$$\chi^2_{x\%} = \chi^2_{min} + \sum_{ij} \frac{\partial^2 \chi^2}{\partial \beta_i \partial \beta_j} \Delta\beta_i \Delta_b eta_j$$

where $\Delta\beta_i$ and $\Delta\beta_j$ represents the variation of the parameters β_i and β_j corresponding to a χ^2 confidential level of $x\%$ (set to 95% in our work). Fig. 3.14 shows the χ^2 constant curves obtained using the command CONTOUR. From the analysis of the curves it is possible to estimate the errors on the two parameters considered, including the effect of the correlation.

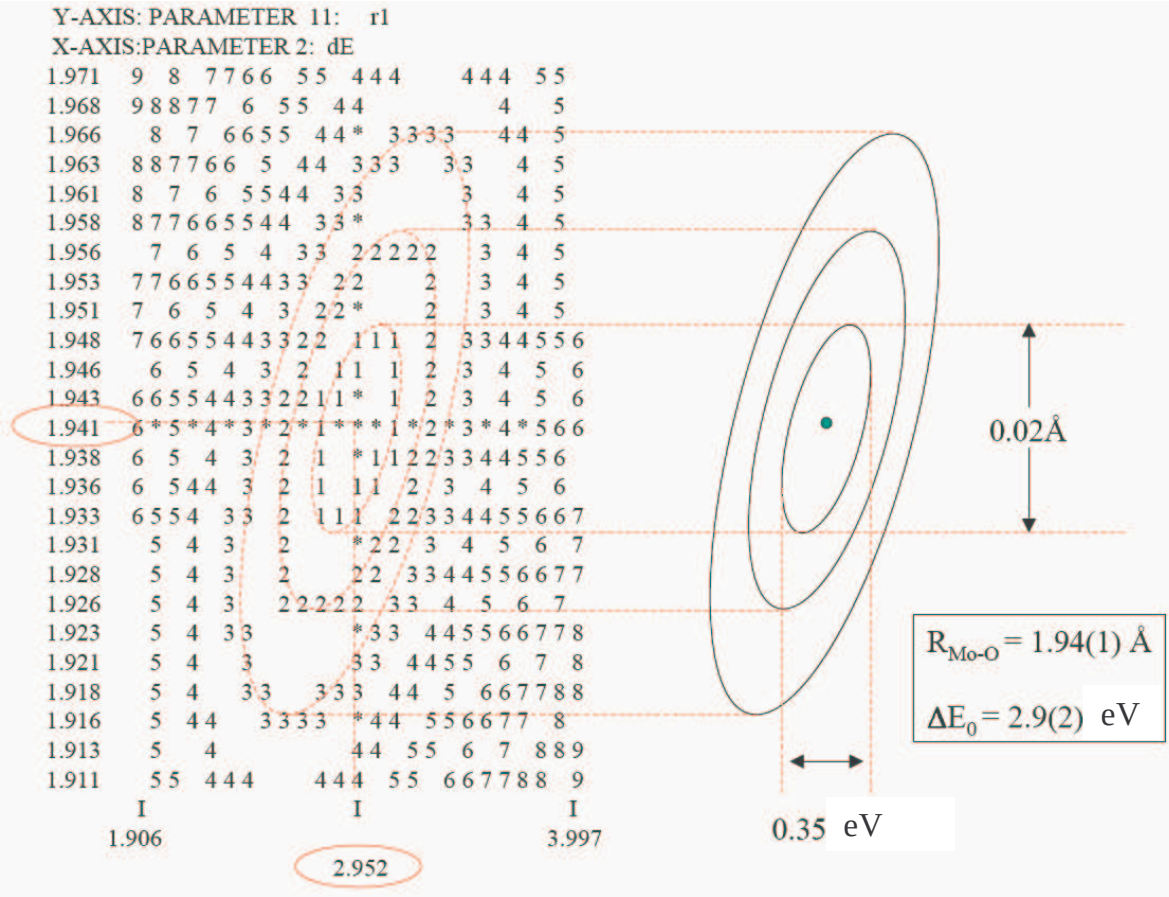

Figure 3.14: χ^2 constant curves for the highly correlated parameters ΔE_0 (energy shift) and R_{Mn-O} (first shell distance) obtained by using the command CONTOUR under MINUIT. From the analysis of the curves it is possible to estimate the errors as shown in the figure.

This matrix, also called error matrix, is the inverse of the second derivative matrix of the χ^2 function with respect to its free parameters, usually assumed to be evaluated at the best parameter values (the function minimum). The diagonal elements of the error matrix are the squares of the individual parameter errors, including the effects of correlations with the other parameters. The inverse of the error matrix, the second derivative matrix, has as diagonal elements the second partial derivatives with respect to one parameter

at a time. These diagonal elements are not therefore coupled to any other parameters, but when the matrix is inverted, the diagonal elements of the inverse contain contributions from all the elements of the second derivative matrix, which is where the correlations come from. Although a parameter may be either positively or negatively correlated with another, the effect of correlations is always to increase the errors on the other parameters in the sense that if a given free parameter suddenly became exactly known (fixed), that would always decrease (or at least not change) the errors on the other parameters.

Information theory shows that for a good fit $\Delta\chi^2 \sim \nu$, ν being the number of free parameters in the minimization ($\nu = N_{ind} - N_{params}$), or equivalently $\Delta\chi^2_\nu \sim 1$, where $\Delta\chi^2_\nu$ is defined as $\Delta\chi^2/\nu$ (reduced χ^2). Systematic errors, which are introduced both during acquisition and analysis of EXAFS data, arise from a large number of sources. Some of the more common sources of acquisition-related systematic errors include sample inhomogeneities, radiation damage, thickness and particle size effects, insufficient suppression of higher harmonics in the monochromatized photon beam, detector nonlinearity, glitches (both monochromator and sample-related), and improper sample alignment. Analysis-related errors include: systematic modifications of the amplitude of the EXAFS oscillations caused by improper pre-edge background subtraction and/or normalization to unit step height; imperfect references (both experimental and ab initio); improper determination of S_0^2 and/or improper energy-dependent normalization when *ab initio* references are used; and technical errors during pre-processing of the data. While some types of systematic error may be eliminated through good data acquisition and analysis practices (e.g., harmonics, alignment, sample preparation), others are often unavoidable (e.g., imperfect standards, certain types of glitches, inadequate energy-dependent normalization). A clear distinction needs to be made between identifiable and well-characterized sources of systematic error,

such as thickness effects, self-absorption effects, energy- dependent normalization, and inadequate structural models, and poorly understood systematic errors, such as those listed in the previous paragraph. The former sources of error are calculable, must be corrected for, and should not be included in the estimate for ϵ. For these reasons determining the fit quality is not easy, especially when the contribution of systematic effects to the total error is significant, e.g., when $\Delta\chi^2 \gg \nu$. For example, it is not clear how to distinguish fits that are truly bad (in the sense of inadequate models) from those simply dominated by systematic errors. These two situations may be differentiated to some extent by examining an R-factor, defined as:

$$R^2 = 100 \times \frac{\sum_{i=1}^{N} |Data_i - Model_i|^2}{\sum_{i=1}^{N} |Data_i|^2}\% \tag{3.44}$$

As long as the signal-to-noise ratio (S/N) of the data is good, the R-factor of adequate fits can be expected to be not more than a few percent. The analysis code utilized in this thesis provides both R^2 and S/N, where the latter being defined as:

$$S/N = \frac{1}{N}\sqrt{\frac{\sum_{i=1}^{N} |data_i|^2}{\epsilon_{stat}^2}} \tag{3.45}$$

Chapter 4

Total Electron Yield

4.1 Introduction

Electron-yield XAS is the non-radiative analog of X-ray fluorescence XAS and provides similar information. However electron-yield is inherently surface sensitive since the electrons, because of their short mean free path in solids, can only escape from the near-surface region of the sample. For this reason this technique has become an established method for surface XAS investigations.

4.2 Formation of the TEY signal

Mass absorption of X-ray photons is dominated by photoemission of electrons which leave an atom with a core vacancy. The photoinduced core hole is unstable and decays in a cascade of inner and outer shell transitions until the photoexcited atom attains charge neutrality. Taking K-edge absorption as an example, the first decay step fills the primary K-shell vacancy with an L-shell electron, This step can occur either by radiationless transition (KLL Auger process) or via emission of a fluorescent photon, the two processes be-

ing in competition. The relative probabilities of radiative and non-radiative transitions of the single core hole vary with the atomic number and their values have been tabulated (see fig. 3.6 chapt 3). The KLL Auger process produces a double L-shell vacancy, while the fluorescent transition simply moves the single core hole into the L-shell; L-shell holes formed during the K-shell neutralization undergo similar decay mechanism as the K-holes, but the relevant transitions involve the M-shell electrons (if present) and have much reduced fluorescence probabilities. The decay of the vacancies in higher shells proceeds likewise, provided that these shells are occupied. The initial shell vacancy, thus, passes (and multiplies in the case of radiationless transition) from inner to outer shells. Charge neutrality is finally restored by hole-filling in the outermost atomic shell (which is, in the case of the conductor, the valence band) by an external supply of electrons. Unfortunately, a quantitative analysis of the cascade of core transitions is made difficult by the fact that the transition rates for the decay of the multiple core holes formed in the KLL and LMM processes are not completely understood. The physical principles underlying the formation and decay of multiple core vacancies are still the object of active research.

The TEY technique involves the measure of the electrons originating from the various radiationless transitions. The KLL Auger electrons are the most energetic, while LMM, MVV and other Auger electrons, coming from higher shells, have energies which are approximately one (LMM), two (MVV) and more (higher shells) orders of magnitude lower. In addition there is also the contribution due to primary photoelectrons, whose energy is zero at the edge step, but linearly increasing with X-ray energy [1].

[1] This contribution gives the linearly increasing background affecting TEY spectra

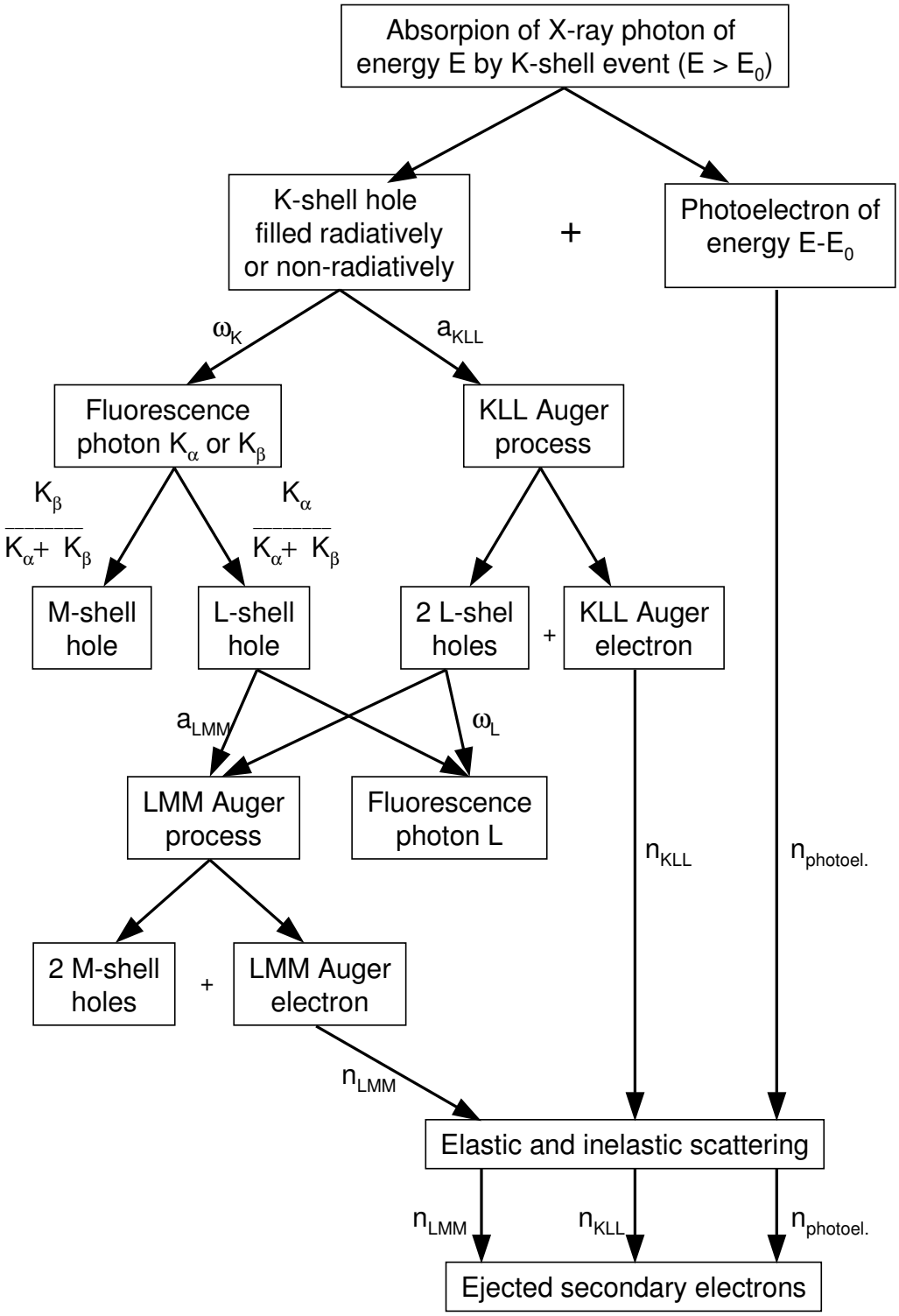

Figure 4.1: Relationships among relevant processes in TEY current production for K-shell absorption. a_{KLL} and a_{LMM} are the probabilities for radiationless decay of K and L-holes. K_α/K_β is the emission rate ratio for the K-shell fluorescence probability $\omega_K = 1 - a_{KLL}$ and n indicates the number of KLL, LMM Auger electrons and photoelectrons.

The emitted flux of these primary photoelectrons is vanishingly small near the absorption edge, because of their low kinetic energy. In most experimental situations, the primary photoelectron contributions to the TEY become visible only at energies well above the edge, where the photoelectron energy becomes comparable to that of the Auger electron contributions. In contrast, the emitted flux from the KLL Auger channel is always substantial because these energetic electrons can travel a comparatively long distance to the surface before their excess kinetic energy is thermalized. Kinetic energy and penetration range of lower-energy Auger electrons (LMM, MVV, etc) are significantly smaller than for KLL ones so that, in bulk samples, the depth information carried by the TEY is mostly determined by the KLL emission. A more surface-sensitive contribution to the Auger yield due to LMM electrons is usually non-negligible. This contribution is particularly pronounced when the thickness of the sample is of the same order as the LMM penetration range; in this case, the LMM flux can become comparable or even larger than the KLL signal.

The signal measured in a TEY experiment represents all electrons which escape from the sample surface. An always present fraction of the emitted electrons is not due to the Auger and photoelectrons generated in the initial X-ray absorption event, but to electrons arising from inelastic scattering processes of primary electrons in the sample specimen. The average energy of these "true" secondary electrons is very low (< 40 eV), with the peak of the spectrum typically centered around a few eV and characterized by a half width which is rarely larger than 20 eV. Because of their low energy content, most of these secondary electrons escape only from a shallow region below the surface, whose thickness is typically less than 100 Å. The rate of secondary electron production is primarily dependent on the probability of inelastic scattering events, so that the magnitude of the secondary electron fraction depends critically on the number energetic electrons which pass through the

near-surface region from which the secondary electron can escape. Accordingly, the depth information contained in the secondary yield is determined by the more energetic electrons escaping from the sample.

4.2.1 Probing depth and gas amplification

The contribution of secondary electron to TEY signal, that is the electrons generated by elastic and inelastic collision in the sample (not to be confused with higher shells, LMM, MVV..., Auger electrons) has been overstated [23] in the past. More recently, in an very complete work, Schroeder [81] demonstrated that TEY is dominated by Auger electrons, at least for absorption edges in the energy above several KeV. Previously it was also assumed that TEY detection in gas-phase may enhance the surface sensitivity. This method is commonly used to enhance the TEY signal through charge-multiplication in the gas-phase. This assumption was based on the consideration that Auger electrons emerging from the sample with high energies have undergone fewer inelastic scattering events along their trajectory and hence should have originated closer to the surface than heavily scattered, lower-energy Auger electrons. But, if TEY were dominated by the low-energy secondary electrons, then gas effects should be negligible because most of the electrons would not be able to afford any charge multiplication via electron/ion pair formation. Following the assumption that TEY signal is mainly formed of Auger electrons, Schroeder concluded, by means of experimental evidences, that gas-flow detection can actually be *less* surface sensitive than vacuum experiments, contrary to earlier predictions [84, 60]. The range of subsurface sensitivity for TEY has been estimated to be $\sim$ 1000 Å from measurements at the Cu K-edge, less than 700-1000 Å for GaAs and 390 Å for Al_2O_3 (Al K-edge). KLL Auger electrons with energies in the range 3-5 KeV originate no more than 1000 Å from the surface. LMM electrons carrying one tenth of the KLL energies have a penetration depth of less than

100 Å. Schroeder has modeled the TEY signal in vacuum and in gas phase as

$$TEY = i_{KLL} + i_{LMM} + i_{sec} \tag{4.1}$$

$$A \cdot TEY = A_{KLL} \cdot i_{KLL} + A_{LMM} \cdot i_{LMM} + i_{sec} \tag{4.2}$$

respectively. Where A is the total amplification factor in gas-phase, A_{KLL} and A_{LMM} are the partial amplification for the KLL and LMM yields and i_{sec} is the secondary electron yield. The latter contribution is mainly produced by inelastic interaction of the lower energy LMM cascade because of the high cross sections for energy losses at kinetic energies below 1 KeV. Because of their very low energy (< 60 eV), MVV and i_{sec} does not undergo significant amplification in gas phase. Since LMM and i_{sec} electrons originate closer to the surface with respect to KLL ones, this model shows how vacuum detection enhance the surface sensitivity of TEY.

A confirmation of the above discussion comes from experiments performed in this thesis on manganites thin films. It has been noted that the quality of the spectra of the thinnest samples (125 and 50 Å) could be improved by lowering the detector-gas pressure. This result is expected from the above considerations, since gas phase charge-multiplication in the detector weights the TEY signal linearly with electron kinetic energy. Nevertheless, for very thin samples, the majority of KLL electrons originate in the substrate. LMM electrons, on the contrary, originate in the near-surface region (i.e. from the thin film), thus carrying the information we are interested to.

In their work, Erbil et al. [23] reported a simple empirical relationship to estimate approximately the effective penetration range (R_p) of electrons which energies lie in the interval 1-10 KeV:

$$R_p \approx \frac{1000E^{1.4}}{\rho} \tag{4.3}$$

where R_p is in Å, E in KeV and ρ is the material's density in g/cm^3.

4.3 Detector

4.3.1 Basic principles

In the contest of my Ph.D. thesis I designed, built and tested a TEY detector to exploit this technique on the GILDA beamline. The fundamental goals of the design were:

- Improved signal to noise ratio by charge-multiplication process in gas phase.
- Ability to measure at low temperature (down to 4.2 K)
- Possibility to smear-out Bragg peaks that could affect TEY signal in the case of crystalline substrate of the sample.

A TEY detector is essentially constituted of a ion chamber with an internal photoemitting sample. The detection of the energetic electrons involves the ionization of the gas atoms or molecules in the ion chamber via impact ionization events. Each ionizing collision between an energetic electron and a gas particle produces a positively charged ion and a free electron. Both particles, due to their opposite charges, attract one another. In an electric field of enough strength, recombination is prevented by acceleration in opposite direction along the electric field lines. The energy required to create such an electron/ion pair has been measured for a wide variety of gases. An important result of these studies is the observation that the pair formation energy is, for most gases, almost independent of the incident electron energy. Furthermore, energy loss necessary for a pair formation varies little between gases; typical values are 30 ± 15 eV. The average electron/ion pair formation

loss in He gas, which is the one generally chosen, due to its low X-ray absorption cross section, is $\Delta E(He) = 42.3$ eV.

Depending on the magnitude of the applied voltage, ionization chambers can be operated in several regimes.

In the highest voltage region (several KeV), the so-called Geiger-Muller region, very high electric field strengths result in intense acceleration of the emitted electrons. Saturated discharge pulses are formed by the detected signal electrons.

The lower-voltage region includes the proportional and the current mode regimes. The proportional region is similar to the Geiger-Muller region in that, field acceleration allows the formation of additional charges via impact ionization of the collision partners. However, the intensity of each charge pulse is proportional to the number of charges which would be formed by each electron in the absence of an electric field. Increasing the field strength in the detector increases the measured pulse height signal.

The current regime is the one we have used in this work and applies at voltage between 60 V and 200 V; below the threshold at which any additional charge, due to field-induced pair formation, can be formed. For voltages lower than 40 V a non linear response of the detector occurs, due to the electron-ion recombination process. The important property of this regime is that the signal strength is independent of the detector voltage, and any gas amplification of the TEY signal, relative to vacuum detection, must originate from the excess kinetic energy carried by electrons from the sample. In this sense, the signal amplification factor is a measure of the kinetic energy content of the TEY.

4.3.2 Design

The design of a TEY detector which fulfills the requirements stated above has been challenging from a technical point of view. The major difficulties

came from the little dimension of the sample chamber of the He cryostat available on the GILDA beamline, which has a diameter of only 3 cm; this resulted in constraints like the size of the components, which must be very little and hence difficult and fit together. Another important issue was due to the cryostat. In such cryostat, liquid helium is released directly in the sample chamber through a Joule-Thomson valve; this method results in very stable temperatures and in a first stage, it seemed convenient to use the helium gas, which serves to cool down the sample, also for the charge-multiplication process. Test runs performed using this setup returned good quality spectra at high temperatures but very noisy ones at low-temperature spectra. This noise was due to rapid changes of the gas density due to the formation of a liquid helium phase at the bottom of the sample chamber. To avoid this problem we built a cylindric shaped box capable to contain the sample, the electrode and the helium gas, together with the in- and out-let gas lines and electrical connection. In these way, the helium used for the charge-multiplication process is separated from the cryostat helium circuit. This system has the further advantage of performing an efficient electrostatic shielding for the sample-collector system (since the cylindric box is metallic) and to give the possibility to choose a custom pressure for the helium gas inside the box, different from that of the cryostat. As we will see, the gas pressure is a key parameter that can be adjusted in order to achieve good quality spectra.

The detector itself is very simple (fig. 4.3). A polarized electrode is placed at a suitable distance from the sample and serves to accelerate and collect the electrons emitted from the sample. According to the work of Schroeder [81], the electrode was placed at 10 mm from the sample surface. In fact, as demonstrated by continuous slowing-down approximation (CSDA) calculations, this distance should be sufficient for energetic Auger electrons to dissipate their kinetic energy so to take part in the charge-multiplication pro-

cess. Such calculations are performed for helium gas at 1 atm and for Auger electrons in the range below 10 KeV (such range covers all KLL Auger electrons energies in the periodic system up to Br). For heavier elements or lower pressures, larger sample-collector distances or heavier detector gases are required. The collector is made of 200 μm of pure Al (99.99%, Goodfellow in order to avoid excitation of edges other than that under invesitgation.

To avoid noise induced by any electrical instrument connected to electric network (50Hz noise), the polarization of the electrode is performed by the means of a set of eight 9 V commercial batteries giving a total voltage of 72 V. This value is chosen well below the proportional regime but high enough to avoid recombination effects, which become important below 40 V. A criterium to optimize the voltage is to detect the voltage at which the TEY current from the samples saturates. The use of higher voltages is useless and enhance spurious electron detection.

In the present setup the TEY signal passes through the battery pack. Since the batteries can superimpose a constant or drifting voltage to the TEY signal, in the future we will polarize negatively the sample. As signal cables, we used an AXON coaxial cable (diameter 1mm) designed for low temperatures; to avoid multiple ground points, the shielding of the cable is connected to the sample, which is isolated from sample holder. A battery-powered OXFORD floating amplifier, detached from the main electric network (typical amplification 10^{10}), is connected to a voltage-to-frequency converter (VFC) and then to a CAEN counter card, which is connected to the acquisition computer.

The whole instrument (detector + sample holder, fig. 4.2) is a 80 cm long steel rod at which end is mounted the detector itself (sample+electrode). The stick is long enough to insure that when the sample at its edge is at the lowest temperature (4.2 K) the upper part is at room temperature. The void inside the stick is used as a gas line to refill of helium or to empty the

sample chamber. It also accommodates the electric cables for the signal, the electrode polarization and for the diode to measures the temperature. This diode is placed as closer as possible to the sample in order to measure the effective sample temperature. The cylindric box which contains the gas is made of aluminum to insure thermal exchange with the cooling helium of the cryostat. Two windows permits the incident X-ray beam to hit the sample and to pass through (if the sample is transparent to X-rays) in order to perform simultaneous transmission measurements. Windows are made of 20 μm thick aluminated Mylar, which is less permeable than Kapton to helium gas. An aluminium layer is evaporated on the windows in order to avoid their electrostatic charging and insure the continuity of the electrostatic shielding.

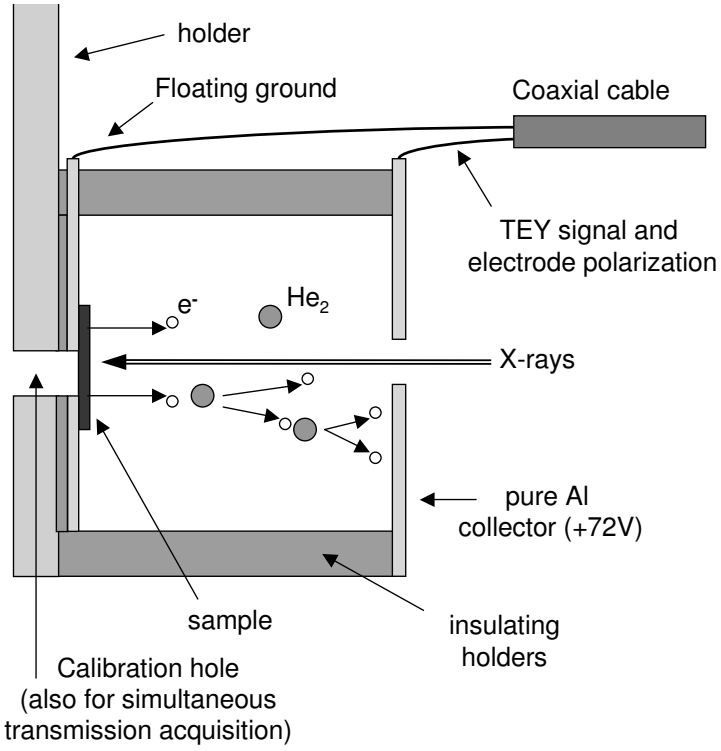

Figure 4.2: Detail of the TEY detector.

An important feature of the detector is the possibility to oscillate the sam-

ple during the measurements. This is useful to reduce intense Bragg peaks coming for example from the substrate in very thin films. Since these peaks occurs when the Bragg condition ($n\lambda = 2sin\theta$) is fulfilled, the basic idea is to keep this condition valid for the shortest time possible by rapidly varying θ. Since each energy point is time integrated, the Bragg peak is smeared out. Hence we needed a fast as possible motion of the sample around the incoming X-ray beam. On the other hand, the amplitude of this movement can be very small. From the relation $\Delta\lambda/\lambda = \cot\theta \cdot \Delta\theta$, for an oscillation reducing the Bragg intensity to 10^{-2} of its original value we get:

$$100 \cdot 10^{-4} = \cot\theta\Delta\theta$$

and hence:

$$\Delta\theta \approx 10^{-2}\text{rad}$$

10^{-4} being the typical energy resolution of the X-ray beam.
A prototype mechanism have been built using a miniaturized electric engine which rotates the sample continuously around the beam. Anyway, due to the little size of the cryostat chamber and to the heat produced by the electric engine it was impossible to cool the sample using such a system. Nevertheless this simple mechanism demonstrated the possibility of partially or totally removing the Bragg peaks. Several different solution have been considered to reproduce a similar movement inside the cryostat at low temperatures. Finally we decided to move the entire sample holder from its upper part, i.e. from outside the cryostat. The movement is no more a rotation but a oscillation of amplitude of about five degrees around the X-ray beam (which is orthogonal to the sample surface). The period of the oscillation is adjustable, its minimum being around 100 ms. Since typical integration time are of 5 s, it is ensured that a large number of oscillations occur for each energy point measured. Further, this solution has the advantages that it does not perturb the signal, since the engine that produce the movement is far enough from

the sample ($\sim$ 100 cm). Moreover, it permitted the use of simple Viton gaskets to keep the cryostat chamber sealed, since the movement is mounted on the part of the cryostat that remain at room temperature. Finally it did not require space inside the very little sample chamber.

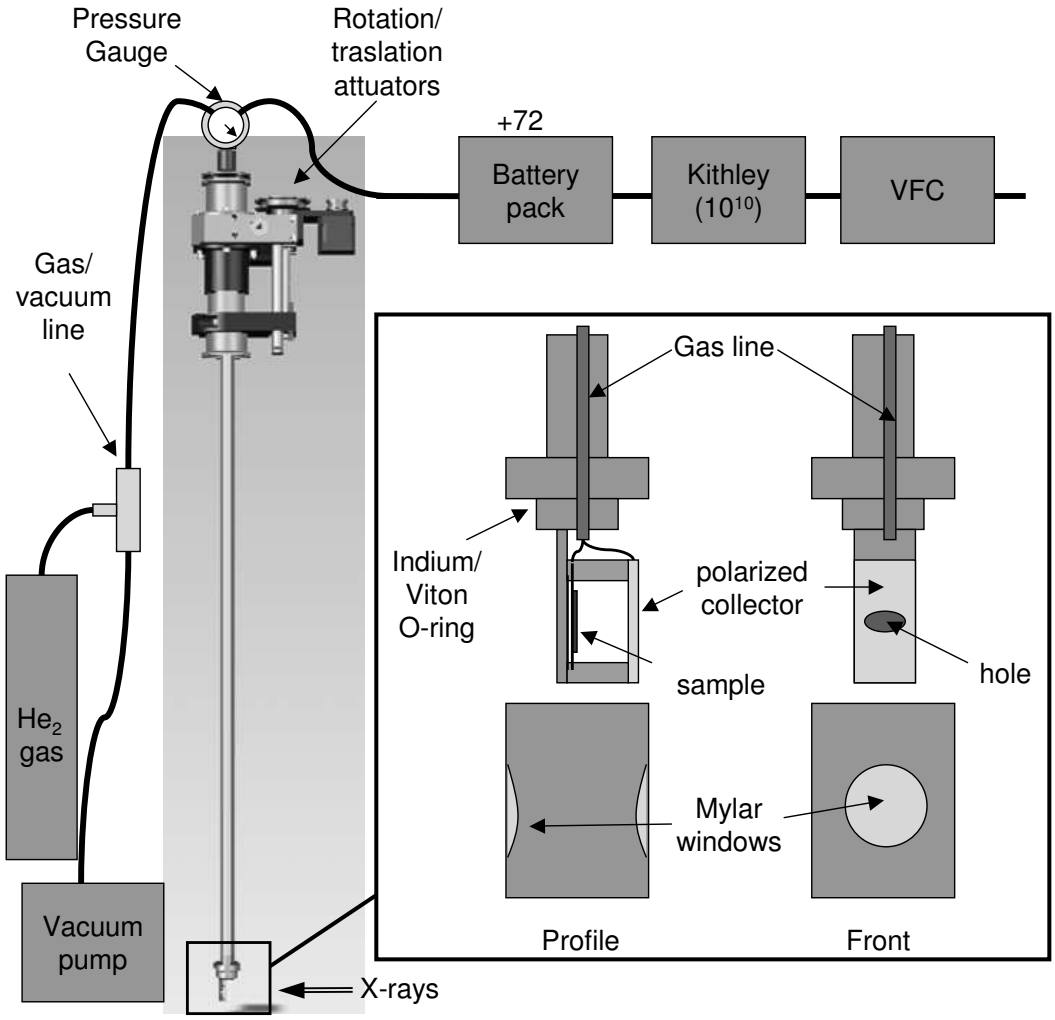

Figure 4.3: Picture of the sample holder and detector system.

4.3.3 Characterization

Test measures have been performed in order to characterize the detector. A standard thin and thick copper foil has been used to study the amplitude reduction factors which is a characteristic of the TEY signal. A manganese foil was then used to quantify this reduction at the Mn K-edge in order to correctly analyze manganite thin film samples studied in this thesis.

Copper foils

Figure 4.4 show the raw TEY signal obtained from a 5 μm thick copper foil, together with its spectrum, simultaneously recorded in transmission mode, and a TEY spectrum of a 1 mm thick copper foil. The comparison between the thick and thin foils has been performed to confirm the hypothesis of Erbil [23] that predicts a reduction of the amplitude of the TEY signal for thin samples. Figures 4.5 and 4.6 show the comparison between the extracted EXAFS signal and their Fourier transformation for the three cases. It can be noted the expected reduction of the amplitude of the signal. This reduction can be quantified to be around 30% for the thin foil and around 25% for the thick one. The signal to noise ratio is lower for the TEY signal (as expected) but of the same order of magnitude.

Figure 4.7 show a comparison between the room temperature and the 150 K spectra of the thin copper foil. As can be noted, the quality of the two spectra is very similar indicating that the detector does not change its properties with the temperature. Nevertheless, it is worth to note that it is crucial to maintain the same helium gas pressure for every measurement, otherwise the efficiency of the detector changes. Obviously, while changing the temperature in a closed box the pressure changes. Actually, the parameter that must be conserved is the number of gas molecules, i.e. the box must be well sealed. To maintain the system sealed at very low temperature, an indium gasket have been added to the Viton one.

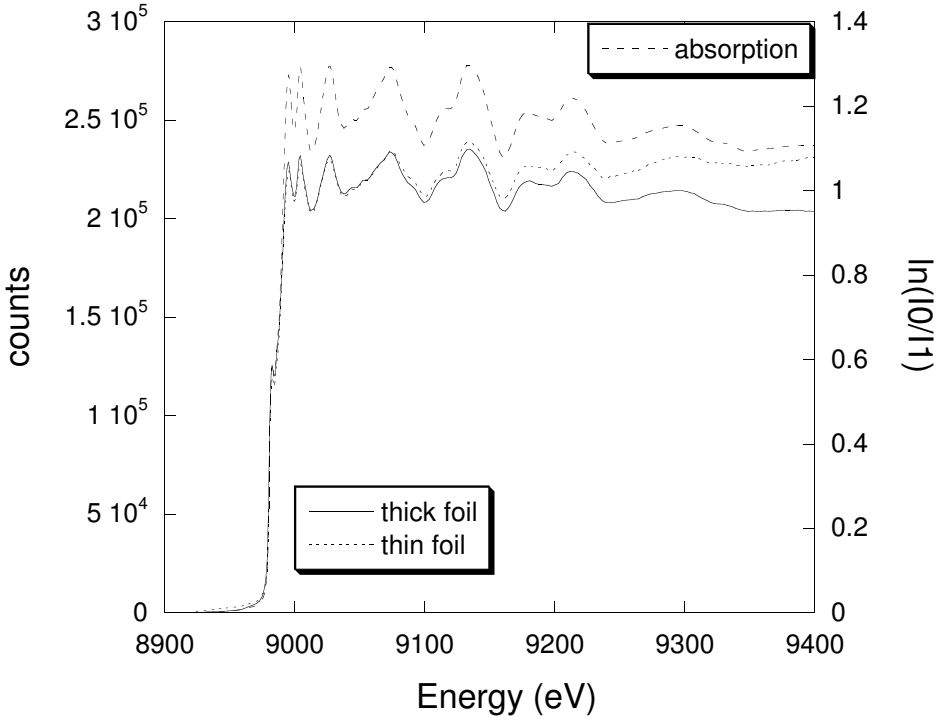

Figure 4.4: Comparison among absorption and TEY raw spectra of a thin copper foil, simultaneously acquired and a TEY raw spectra of a thick copper foil.

Table 4.3.3 reports the extracted structural parameters from a first shell analysis. As can be seen, the parameters are very similar except for the many body loss factor (S_0^2) that, in this case, includes the expected reduction of the TEY signal amplitude [81]. Another difference can be found in the value of the Debye-Waller factor for the low temperature spectra, which results lower, as expected from lower thermal damping.

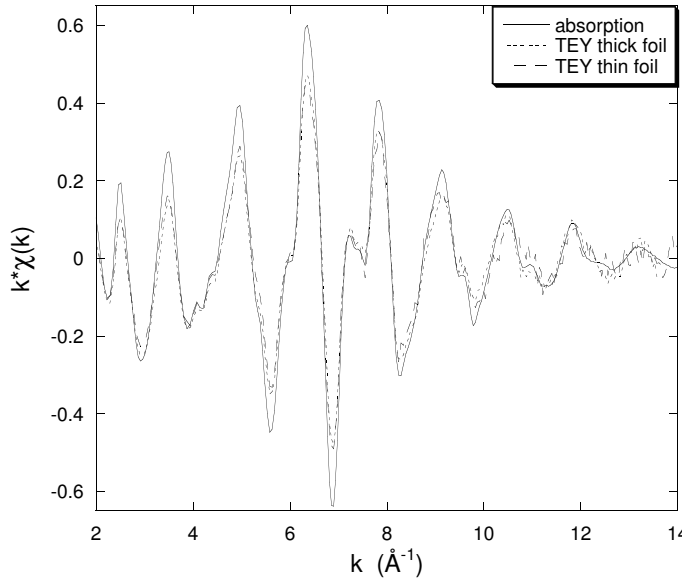

Figure 4.5: Comparison among the extracted EXAFS oscillation of the spectra reported in the upper figure.

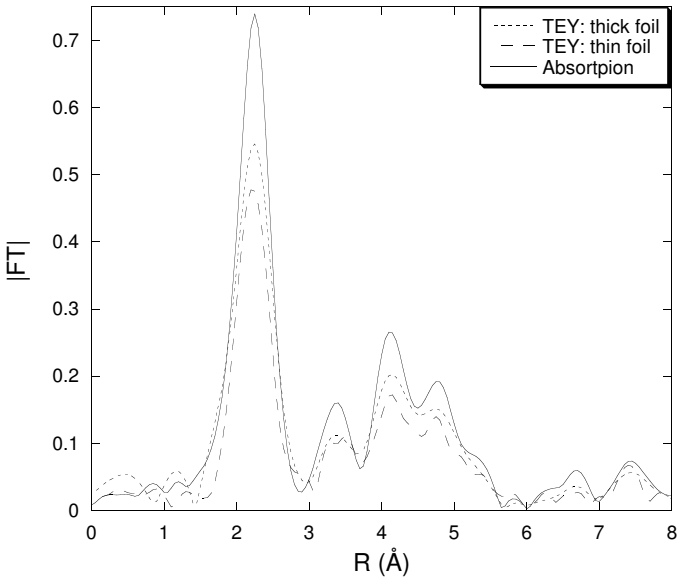

Figure 4.6: Comparison among the Fourier transformations of the spectra of a thin and a thick copper foil measured by absorption and TEY techniques

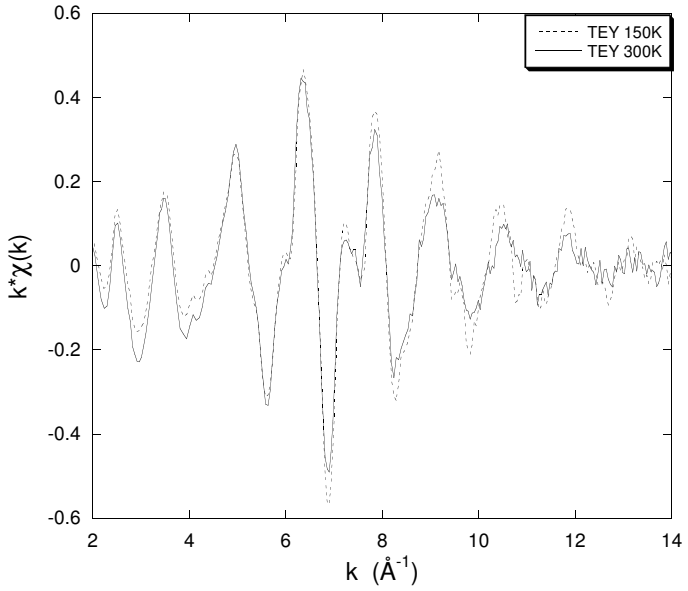

Figure 4.7: Comparison between the EXAFS oscillations of the 300 K and 150 K spectra of a thin copper foil. It can be noted the lower Debye-Waller factor for the 150 K EXAFS signal.

	T(K)	S_0^2	R(Å)	σ^2 (Å^2)
Absorption	300	0.9(1)	2.536(9)	0.007(1)
TEY thick foil	300	0.7(1)	2.53(1)	0.007(1)
TEY thin foil	300	0.6(1)	2.53(1)	0.007(1)
TEY thin foil	150	0.6(1)	2.53(1)	0.005(1)

Table 4.1: Fitted values of the copper samples measured by TEY and absorption. The value of the S_0^2 factor confirms the expected reduction of the amplitude of the TEY signal with respect the absorption one.

Manganese foil

A 4 μm thick manganese foil has been measured using TEY and transmission simultaneously to measure the reduction of the signal amplitude. Unexpectedly, as can be seen from fig. 4.8, the transmission and TEY spectra are very different.

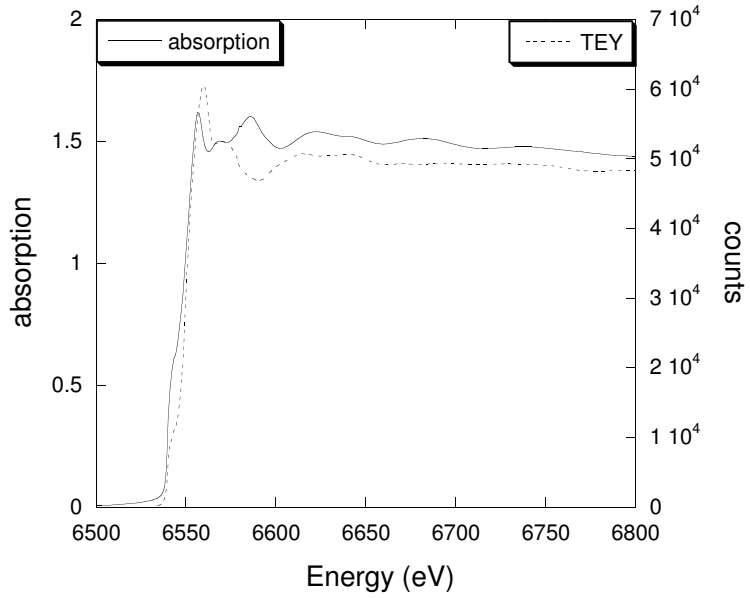

Figure 4.8: Comparison between simultaneously acquired absorption and TEY spectra of a Mn foil.

The transmission spectrum is clearly a spectrum of bulk manganese. Differently, TEY spectrum shows a large white-line typical of oxide compounds. This assumption is supported by fits performed on the two spectra. Transmission spectrum can be easily fitted using the only metallic manganese backscattering theoretical functions. The value of the Mn nearest neighbor distance corresponds to the Mn-Mn bond value. On the other hand, TEY spectrum can be fitted only using an admixture of manganese oxides.

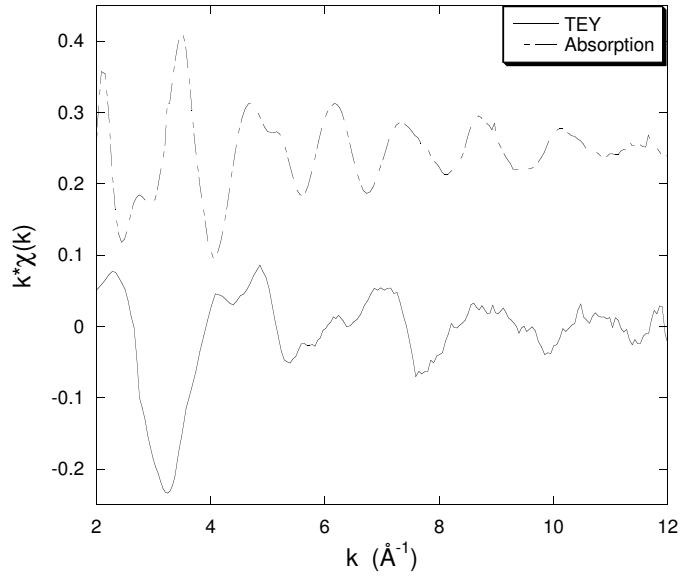

Figure 4.9: EXAFS oscillation extracted from the Mn-foil absorption and TEY spectra reported in figure 4.8

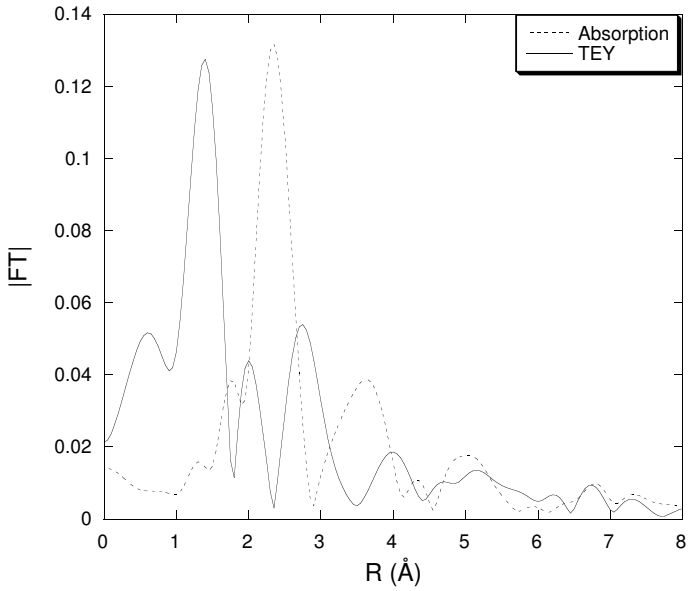

Figure 4.10: Fourier transforms of the EXAFS signals reported in the figure 4.9.

The nearest neighbor is clearly found to be oxygen, at a distance much lower than that of the Mn-Mn bond, as can be seen by eye from the Fourier transform of the EXAFS oscillations (fig. 4.10). Thus, an unknown thickness oxidized Mn layer covers the Mn foil used for the test.
This result evidences the probing depth dependence of the TEY technique.

Manganite thin films

The study of manganites thin films motivated the realization of the TEY detector; in particular we studied Na doped manganites thin films of thickness ranging from 50 to 750 Å, grown on a 1 mm $SrTiO_3$ substrate. Due to the small thickness, the signal coming from the manganite film is very low compared to the strong signal of the substrate; in such cases, fluorescence yield is usually a suitable detection scheme. Nevertheless, in this particular case there were two major problems. First: the fluorescence line of the Mn K-edge we want to investigate is near to the intense fluorescence line of the Ti present in the substrate (fig. 4.11). A solid state fluorescence detector has limited count rates and was unable to measure the strong signal from the Ti fluorescence together with the very low Mn signal. Further, due to the low Mn fluorescence ($\sim$ 100 counts/s) it was useless to introduce filters which reduce the Ti signal. Second: strong Bragg peaks from the substrate prevented the use of the fluorescence technique. On the other hand, due to its limited probing depth, TEY retrieved less intense Bragg peaks; To further reduce Bragg peaks the sample was oscillating, as described in the previous paragraph. The efficiency of the oscillation in removing Bragg peaks can be judged by comparing the raw TEY spectra reported in figure 4.12. These spectra have been recorded at 10 K, on the same sodium doped 750 Å manganite thin film, in the case of oscillation switched off (upper figure) and on (lower figure).

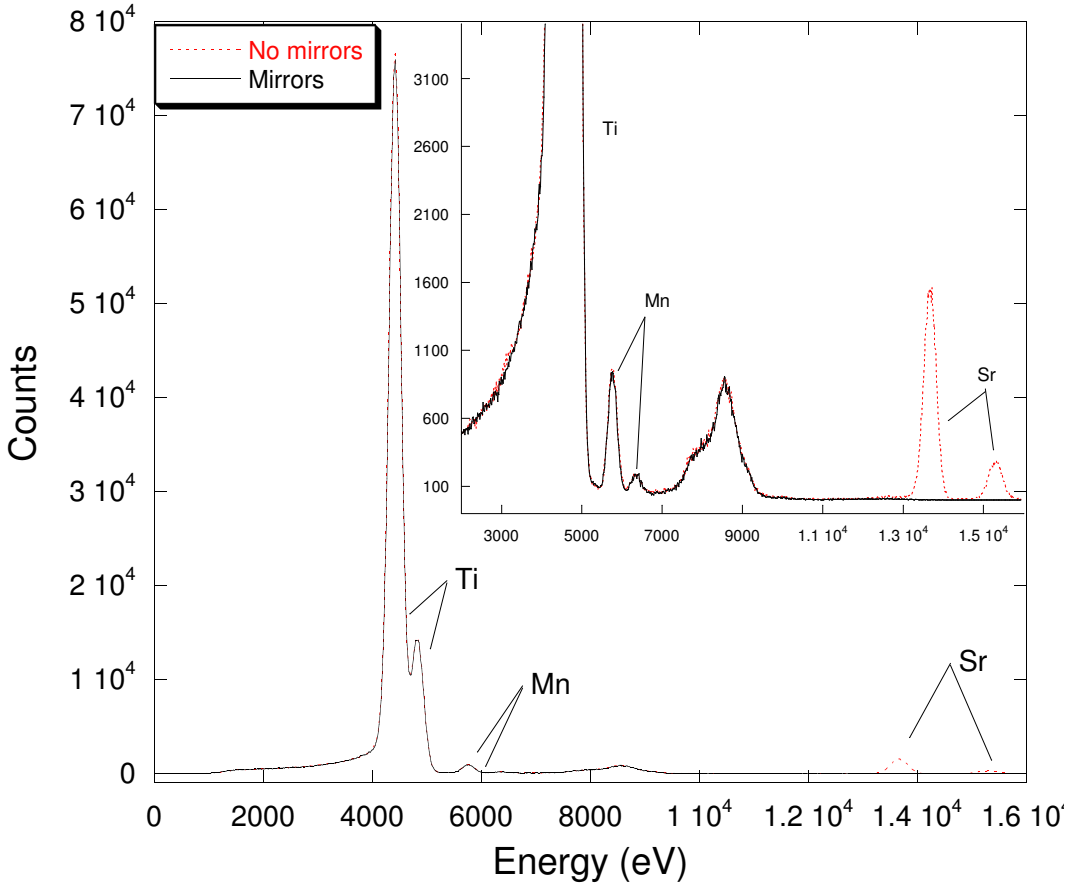

Figure 4.11: Fluorescence peaks of a $La_{0.87}Na_{0.13}MnO_3$ 750 Å thin film deposited on a $SrTiO_3$ substrate measured at 6.6 KeV, above the Mn k-edge (6.5 KeV). The fluorescence of the Sr at $\sim$ 14 KeV can be noted in the case no harmonic rejection mirrors are present. This derives from the contribute of the third harmonic harmonic at 19.8 KeV (using 311 Si monochromator crystals) which excites the Sr K-edge at 16.1 KeV.

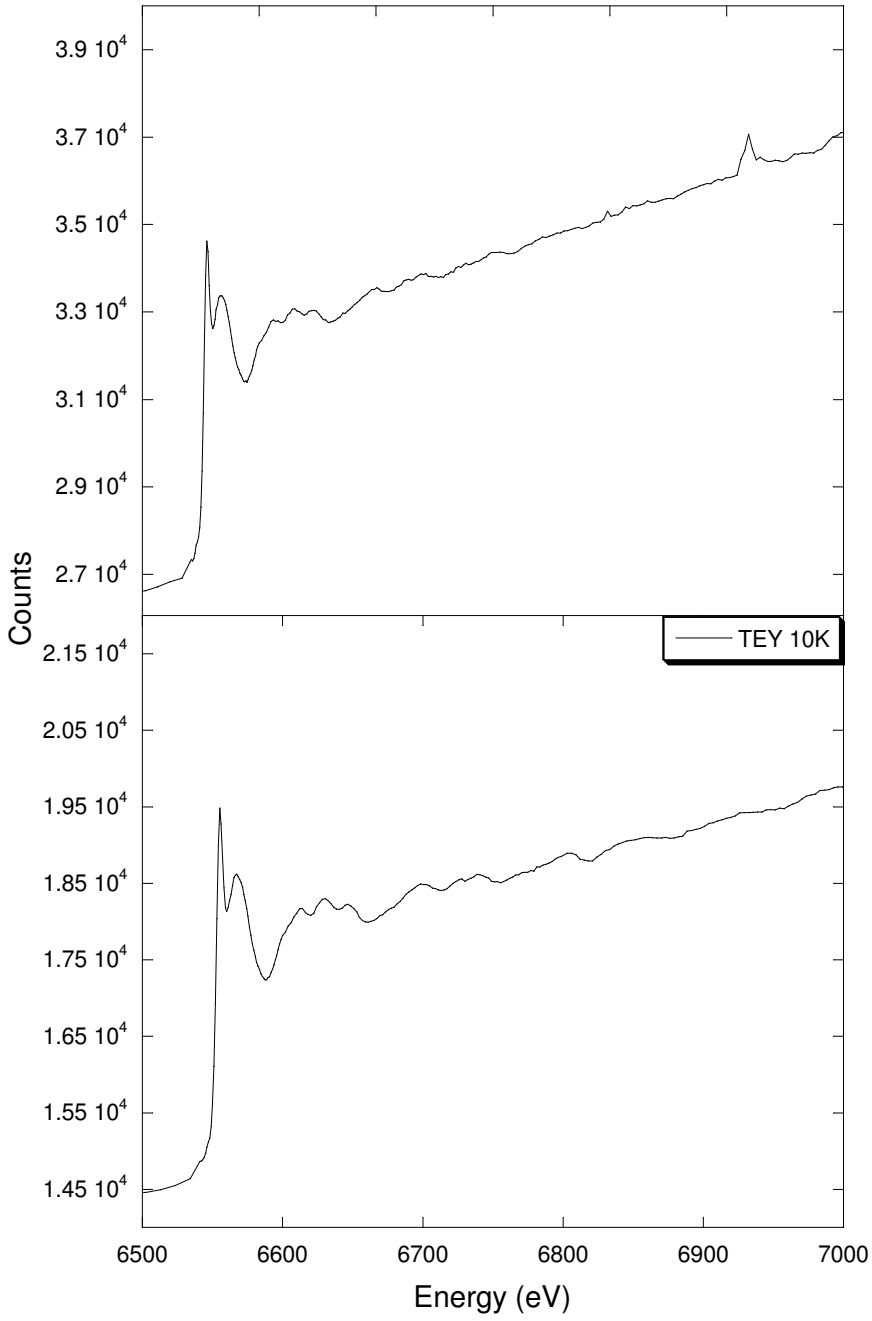

Figure 4.12: Comparison between the raw TEY spectra of a $La_{0.87}Na_{0.13}MnO_3$ 750 Å thin film acquired at 10K without (upper panel) and with (lower panel) the Bragg peaks removal system. The effectiveness of the removal system can be judged from the figure.

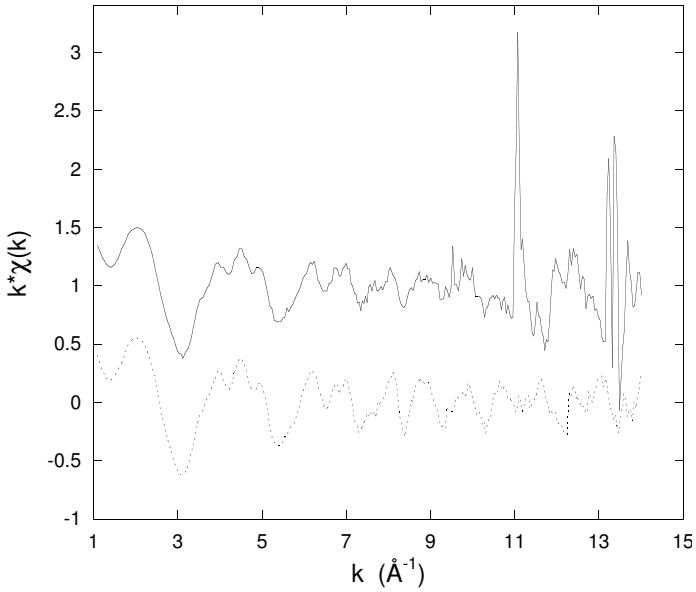

Figure 4.13: EXAFS oscillations extracted from the spectra reported in figure 4.12. It is evident the effect of the Bragg peaks, present in the spectra acquired without the removal mechanism, on the extraction of the data.

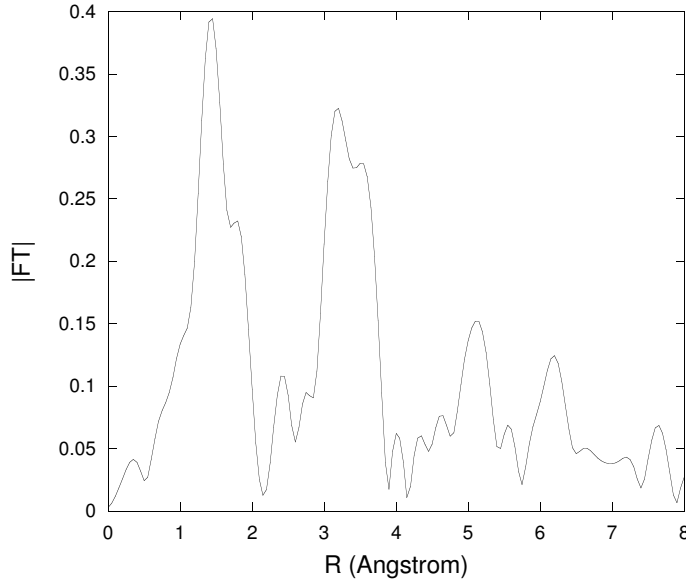

Figure 4.14: Fourier transformation of the EXAFS signal reported in the upper figure in the case of removal mechanism switched on.

From figure 4.12 it is evident the efficiency of the system in removing Bragg peaks. As can be seen in fig. 4.13, in the case of oscillation switched off, intense Bragg peaks prevented the spectra from being analyzed. On the contrary, when the oscillation mechanism is switched on, these peaks are reduced below the noise level. A vestige of Bragg peaks are still present at higher values of the wave vector K (> 12 Å^{-1}), where the amplitude of the signal become smaller, preventing the analysis of the spectra above K= 12 Å^{-1}.

4.3.4 Conclusions

In this thesis work I designed, developed and tested a TEY detector capable to measure at low temperatures and to smear-out parasitic Bragg peaks. The comparison between the test measurements and the data in the literature, demonstrate the goodness of the instrument. Nevertheless, more work has to be done to optimize the system and characterize the detector. It is crucial to have a good knowledge on the behavior of the system upon all the possible adjustable parameters. In particular it is important to achieve a better knowledge of the amplification factor in gas phase with respect to the vacuum acquisition mode. Other important issues are the study of the optimal pressure as a function of the sample and the dependence of the current intensity on the geometry of the detector and the sample-collector distance. Another issue to investigate is the efficiency of the Bragg removal mechanism system on other samples.

Chapter 5

Thin films

5.1 Introduction

As discussed in the first chapter, perovskites based on transition-metal oxides show a large number of properties related to the competing interactions between charge, spin and lattice. This versatility allows to design heterostructures with very promising technological properties. Among these, the best known are probably tunnel junctions based on half metallic manganites such as $La_{2/3}Sr_{1/3}MnO_3$ (LSMO) [44, 89] and $La_{2/3}Ca_{1/3}MnO_3$ [32] (LCMO), but spinvalves structures [58] or spin injectors [20] have also been fabricated. The improvement in controlled heterostructures and multilayers is a necessary stage for the realization of many devices and circuits. Thin-film methods offer a powerful and versatile technique for growing new structures. This is due to strain effects that can stabilize structures which do not exist under classical conditions of pressure and temperature. In bulk, the physical properties of these materials depend on the overlap between the manganese d orbitals and oxygen p orbitals, which are closely related to the Mn-O-Mn bond angle and the Mn-O distance. As the unit cell of the thin film is modified with respect to that of the bulk material, the Mn-O distances and Mn-O-Mn angles

are altered, inducing variations in the electronic properties. Since it has been shown that in the bulk material a slight variation of the Mn-O bond length or bond angle drastically modifies the physical properties, it is of prime importance to carry out a microstructural characterization of the films, trying to understand how such microscopical characteristic are influences by growth parameters.

One thing is to study the thickness dependence of the magnetoelectronic properties of films grown on different substrates as a function of film thickness, t. Two major features are usually observed. First, the resistivity increases when t is reduced. It has also been found that when t is lower than a critical value, LSMO and LCMO films are insulating in the whole temperature range [92, 10]. These observations have been interpreted as due to the presence of an insulating dead layer, i.e. an interfacial reaction layer between the substrate and the manganite film [86, 28]. This is often accompanied by a decrease of the magnetic moment and magnetically dead layers have also been detected recently [63, 8, 95, 94, 11]. However, the factual presence of a dead layer has been questioned in LCMO films [95]. The thicknesses of these dead layers are usually of the order of tens of Å and varies with the nature of the substrate. Second, several publications have reported a reduction of the Curie point, T_c, and of the metal-insulator transition temperature, T_{MI}, in LSMO and LCMO films with respect to bulk values, when t decreases. This is the case of films with a gradually relaxed structure but also of fully strained films, which is an indication that strain cannot be the only factor responsible for the reduction of T_c in very thin films. Evidence of multiple phase separation into ferromagnetic-metallic, ferromagnetic-insulating, and non-ferromagnetic-insulating regions, has been found [7]. The nucleation of non-metallic regions appears to be related to a modification of the carrier density in the metallic phase which causes the Curie temperature to decrease for thinner films. The change in the effective doping value induced by phase

separation can be considered as one of the possible factors responsible for the thickness dependence of T_c in manganite thin films. The other factors are the substrate-induced strain and disorder, which is discussed in the next paragraph, and orbital degeneracy effects, such as the Jahn-Teller effect, always present when dealing with trivalent manganese ions.

5.1.1 Substrate-induced effects: strain and disorder

Thin films deposited onto different substrates are usually affected by anisotropic strains, which are due to the epitaxial grown of the films on substrates having different lattice parameters, an effect called: lattice mismatch. For example, it has been reported that in ultrathin films (< 60 Å) of LCMO grown on $SrTiO_3$ (STO), the crystal structure is different from the bulk [92] and the strain induced by the substrate leads to disorder effects. The lattice mismatch between the film and the substrate can be evaluated using the formula $s = 100 \cdot (a_S - a_F)/aS$ (where a_S and a_F respectively refer to the lattice parameters of the substrate and of the film). For example, $La_{1-x}Na_xMnO_3$ films are under tensile stress when epitaxially grown on STO substrate. That is, there is a decrease of the lattice parameters in the growth direction and an expansion in the plane. Same films are under compressive stress on $LaAlO_3$ (LAO): decrease of the lattice parameter in the plane and expansion out of the plane. For a tensiled film, the out-of-plane and in-plane parameters, respectively gradually increase and decrease as a function of the film thickness, as shown in fig. 5.1 [64]. Further, lattice mismatch influences not only the parameters of the film but also the texture (or epitaxy), i.e. the in-plane alignments.

A surprising effect of lattice mismatch is related to the orientation of the films, especially those that crystallize in an orthorhombic perovskite cell. This was first seen for $YMnO_3$ [72] which is (010) oriented on STO, but (101) oriented on $NdGaO_3$ or LAO. This dependence on the orientation with

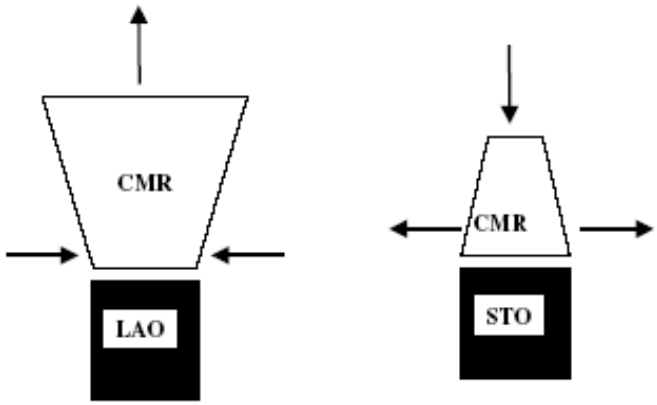

Figure 5.1: The schematic structure of a film grown under tensile stress on STO (right panel) and compressive stress on LAO (left panel). Note the compression or the elongation of the out-of-plane parameter, depending on the nature of the stress.

respect to the substrate is explained by the lattice mismatch which should favor one particular orientation.

From XRD measurements, many groups have reported the presence of two regimes of strain relaxation: one highly strained regime, located close to substrate and having constant thickness and another, quasi-relaxed, in the upper part of the film, which increases with film thickness. These two distinct thickness ranges behave differently with respect to the thickness dependence of the magnetotransport properties [90]; contrary to the lower one, the upper range ($t > 200$ Å) is weakly thickness dependent. Nevertheless, It is not exactly clear where the interface is located or even if it exists in every film. As proposed in [9], structural disorder at interface could arise from the coexistence of different atomic terminations at the surface of the substrate at the beginning of the growth. Indeed, it has been reported that commercial STO substrates generally present two types of terminations, namely SrO or TiO_2 [36]. In this case, it is expected that the manganite grows with (La,Ca)O planes on top of TiO_2 terminations and MnO_2 planes on SrO terminations. The existence of these two possible environments for the Mn ions at the in-

terface, could promote electron localization in highly distorted sites (MnO_2 /SrO type) as well as the coexistence of a spreading of Mn-O distances and Mn-O-Mn angles. This would certainly induce a substantial disorder in the magnetic interactions (double and super-exchange) in a ferromagnetic homogeneous system and can lead to the nucleation of antiferromagnetic regions within the model of Moreo et al. [51].

In order to obtain more information on fundamental issues such as the thickness dependence of the Curie temperature and the origin and characterization of dead layers, we have performed a systematic study of the thickness dependence of the microstructural and magnetotransport properties of films of optimal doped $La_{1-x}Na_xMnO_3$ ($x = 0.13$) deposited on $SrTiO_3$ with thickness in the range 50 Å $\geq t \leq$ 750 Å. Aim of this work is to investigate the local structural environment of Mn by means of X-ray Absorption (XAS) techniques, as a function of the thickness of the manganite layer, to get an insight into the actual presence and nature of the dead layer. The choice of Na doped material is due to the fact that the disorder induced by doping is expected to be small, both because the amount of doping is halved, as two holes per doping atom are created for charge compensation [47], and because the close similarity in the ionic radii for 12-fold coordinated Na^+ and La^{3+} (1.39 and 1.36 Å, respectively) [83]. Since, the structure of these materials is expected to be more ordered than Ca-doped manganites with the same hole content, we should be able to detect smaller variations in the local environment of Mn.

5.2 Sample preparation

All the samples were prepared by the group of professor P. Ghigna at the department of chemical physics of the University of Pavia. Powder $La_{1-x}Na_xMnO_3$

samples with $x = 0.13$ (corresponding to optimized CMR response) were synthesized by solid state reaction starting from high purity (Aldrich $> 99.99\%$) stoichiometric amounts of La_2O_3, Mn_2O_3 and Na_2CO_3. Pellets were prepared from the thoroughly mixed powders and allowed to react at 1173 K for a total time of at least 90 h in air.

Thin films of the $La_{0.87}Na_{0.13}MnO_3$ materials were deposited onto $SrTiO_3$ (STO) (100) single crystals (Mateck) by an off axis radio frequency (RF) magnetron sputtering system (RIAL vacuum); the gas in the chamber was an argon/oxygen mixture (ratio 12:1). This gas composition was chosen because in previous investigation it have been observed that the formation of films with the same stoichiometry, with respect to the target material, can be properly accomplished in an oxygen-poor gas environment [45]. The total pressure in the sputtering chamber was $4 \cdot 10^{-6}$ bar and the RF power was kept at 145 W. The substrate temperature, measured with a K-type thermocouple located under the substrate, was set at $700C^0$. The film thickness was monitored by means of an internal quartz microbalance and precisely defined by X-ray reflectivity (XRR) measurements. Four films have been deposited, with thickness equal to 750, 250, 125 and 50 Å, respectively.

5.3 Sample characterization

X-ray powder diffraction (XRD) measurements and electron micro-probe analysis (EMPA) inspections were performed to check the chemical and phase purity of the obtained materials. XRD patterns were acquired on a Philips 1710 diffractometer equipped with a Cu anode, adjustable divergence slit, graphite monochromator on the diffracted beam and proportional detector. The lattice constants were determined by minimizing the weighted squared difference between calculated and experimental Q_i values, where $Q_i = 4\sin^2 2\theta_i/\lambda_i^2$ and weight$= 1/\sin^2 2\theta_i$. Instrumental aberrations were

considered by inserting additional terms into the linear least square-fitting model.

EMPA measurements were carried out using a ARL SEMQ scanning electron microscope, performing at least 10 measurements in different regions of each sample. According to EMPA and XRPD, the above synthetic procedure gave single phase materials; in addition, for each composition the prepared materials were found to be homogeneous in the chemical composition, in fair agreement with the nominal one.

Magnetization measurements were performed in the $2 \div 300$ K temperature range with an applied magnetic field $H = 100$ Gauss, after a zero-field cooling (ZFC) process and during a field cooling (FC) process, by means of the standard sample extraction technique using a superconducting quantum interference device (SQUID) dc magnetometer, with the sample parallel to the applied magnetic field.

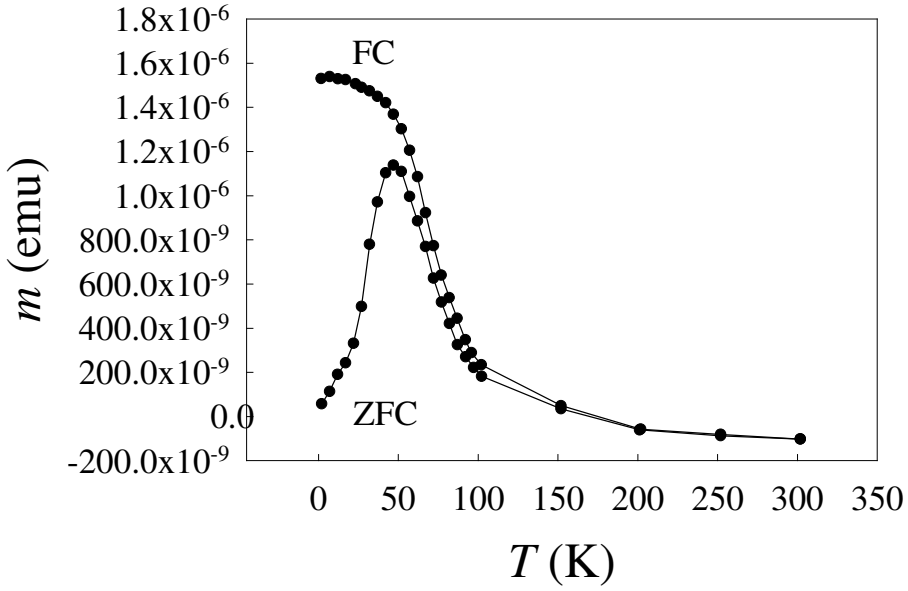

Figure 5.2: Magnetization of the 50Å thick $La_{1-x}Na_xMnO_3$ film ($x = 0.13$).

Fig. 5.2 reports the magnetic susceptibility measurements for the 50 Å film.

The magnetic response suggests a spin glass behavior.

Direct current (DC) resistance measurements were performed in the four probe geometry by means of an Amel 55 galvanostat, a Keithley 180 nanovoltmeter and a Leybold ROK cryostat. Fig. 5.3 shows the resistance plots for the 125, 250 and 750 Å films. For these three films; a quite sharp transition from insulating to metallic behavior is found near room temperature. For the 750 Å thick film an additional feature is evident near 150 K. On the contrary, the 50 Å thick film was found to be fully insulating at room temperature, with a resistance of about $10^9\Omega$: therefore, for this film it was not possible to carry out any resistance measurement as a function of T. At least for the films grown onto STO (100) substrates, it is therefore possible to infer the presence of an insulating dead layer, the thickness of which is no less than 50 Å.

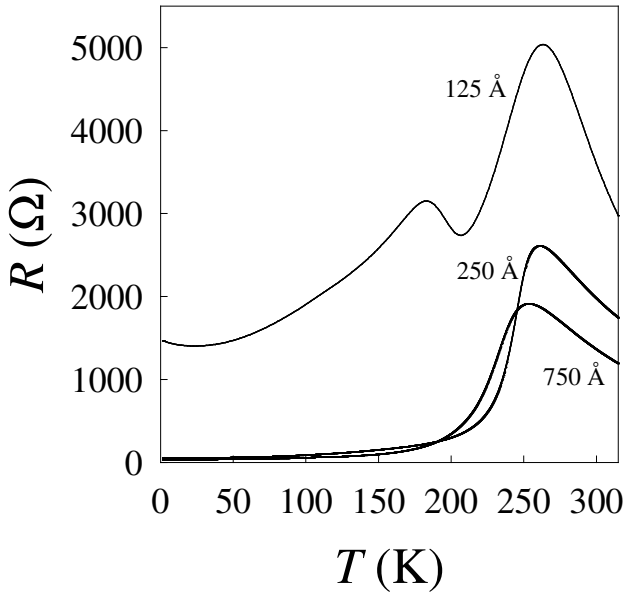

Figure 5.3: Resistance plots of the 750, 250 and 125 Å $La_{1-x}Na_xMnO_3$ films.

An atomic force microscopy (AFM) characterization was performed on all the prepared films. For all of them, a general and common morphology was

observed; in particular, it can be shown that the films are made of small grains with average dimension lower than 20 nm.

5.4 X-ray absorption measurements

The X-ray absorption fine structure (XAFS) spectra have been recorded on the GILDA (BM08) beamline at the European Synchrotron Radiation Source (ESRF) in Grenoble (France) by means of the Total Electron Yield (TEY) technique. All the spectra have been recorded performing energy scans in the range including the Mn K-edge (6539 eV) with the monochromator equipped with Si 311 crystals. A prototype TEY dedicated sample holder, which exploits same ideas of the more sophisticated TEY detector described in chapter four, have been used (fig. 5.4.

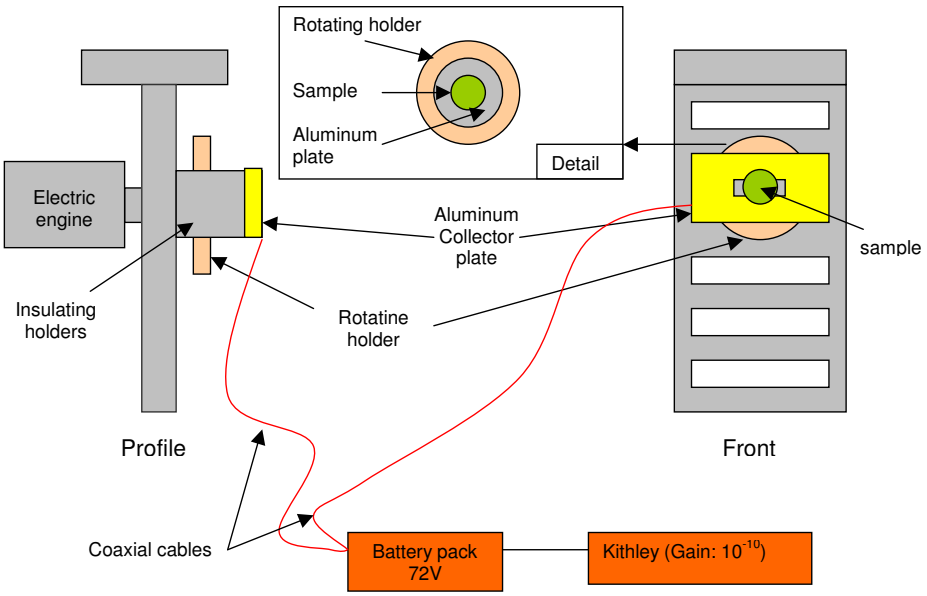

Figure 5.4: Schematic picture of the prototype TEY detector.

This prototype was unable to work at low temperatures; for this reason all the measurements were performed at room temperature. The emitted pho-

toelectrons were collected by a 100μm pure aluminium (99.99%, Goodfellow) plate, polarized at 72 V and mounted at about 10 mm from the sample surface by means of plexiglass bearings. The experimental chamber was filled with He at 1 atm. In addition, the sample was continuously turned around the incoming beam direction, by the means of an electric engine, to smear-out strong Bragg peaks coming from the crystal substrate. A comparison between spectra collected with and without this Bragg peaks removal apparatus can be found in the previous chapter, which confirmed the goodness of this system. The first ionization chamber, dedicated to the monitoring of the incident beam, was filled with 500 mbar of nitrogen gas to achieve a 80% beam transmission and a stable feedback. The current recorded by this chamber (I_0) was used to normalize the data in the following way:

$$\mu \cdot x = \frac{I_e}{I_0}$$

where μ represents the absorption coefficient, x the effective sample thickness (corresponding, in the case of TEY, to the effective electron penetration depth), I_e the photoelectron current from the sample and I_0 the incident beam current. I_e and I_0 signals were connected to Keithley amplifiers and the amplification factors were typically 10^{10} and 10^8, respectively. Typical I_e current was of about hundreds of pA at an incident beam intensity corresponding to $\sim 1.5{\cdot}10^9$ ph/s. The amplifiers were connected to a multi-channel voltage-to-frequency (VFC) module and then to a multi-channel counter card (CAEN) and finally recorded on the acquisition computer. Higher harmonic contributions were removed by using a couple of silver coated rejection mirrors (cut-off energy: $\sim 8KeV$) which dumped the incident beam intensity by a factor 3.

Up to ten absorption spectra have been recorded for each film thickness and then interpolated and averaged. The rotating holder succeeded in removing strong Bragg peaks up to $k = 11$ Å^{-1} while, above this value, residual peaks

are still present, even if not visible from the raw data, and prevented the extraction of the EXAFS signal above this value of k. The series of spectra reported in fig. 5.5 gives an idea of the degree of reproducibility of the data.

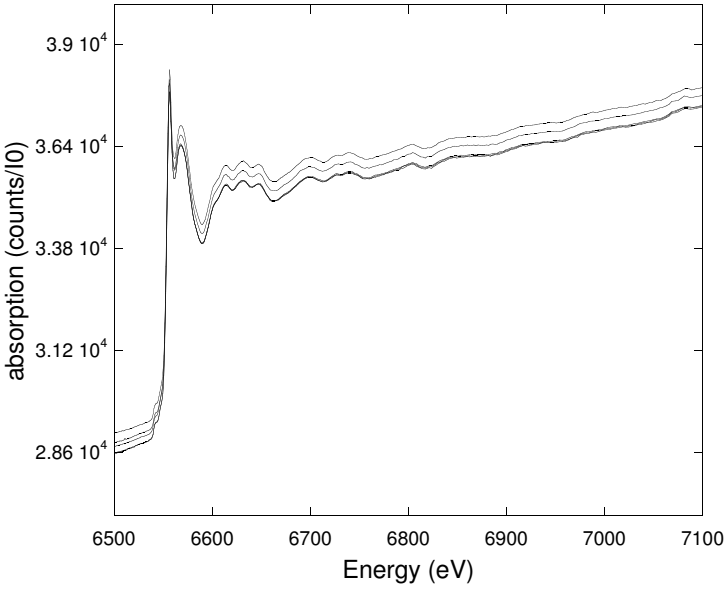

Figure 5.5: Sequential TEY spectra of the 250 Å thick sample.

To carry out the X-ray absorption near edge structure (XANES) analysis, we processed the spectra by subtracting the smooth pre-edge background, which was fitted with a straight line. Each spectrum was then normalized to unit absorption at 1000 eV above the edge, where the extended X-ray absorption fine structure (EXAFS) oscillations are no more visible. The pre-edge region of the Mn-K edge is affected by a vestige of the EXAFS of the La-L_{III} edge. However, it can be shown that the La oscillations have a too small amplitude and are too slowly varying with energy to affect the analysis of the Mn-K edge XANES [13]. The procedure described in chapter three was used to analyze the EXAFS data. The distances were assumed to follow Gaussian distributions, so that only the Gaussian part of the Debye-Waller factor was modeled.

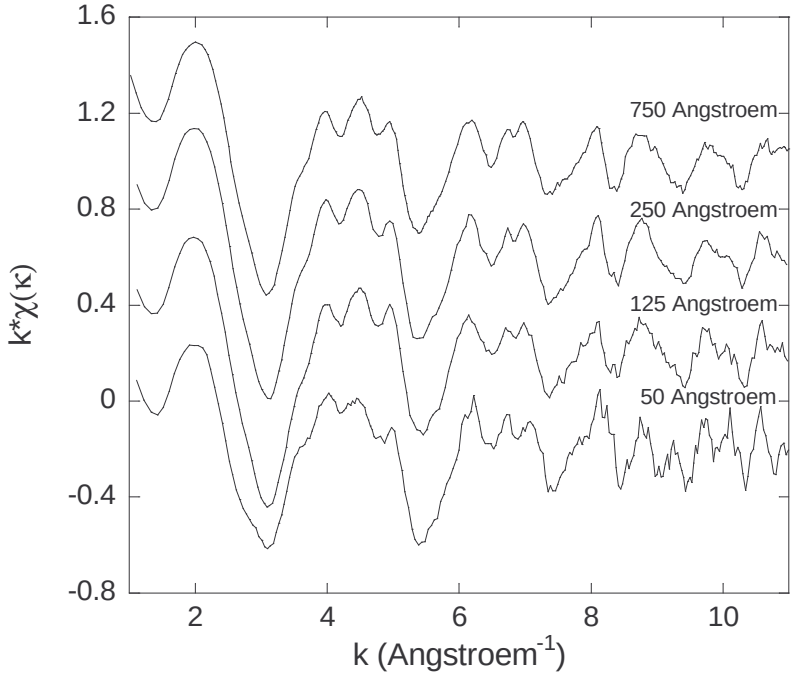

Figure 5.6: EXAFS signals as a function of the sample thickness.

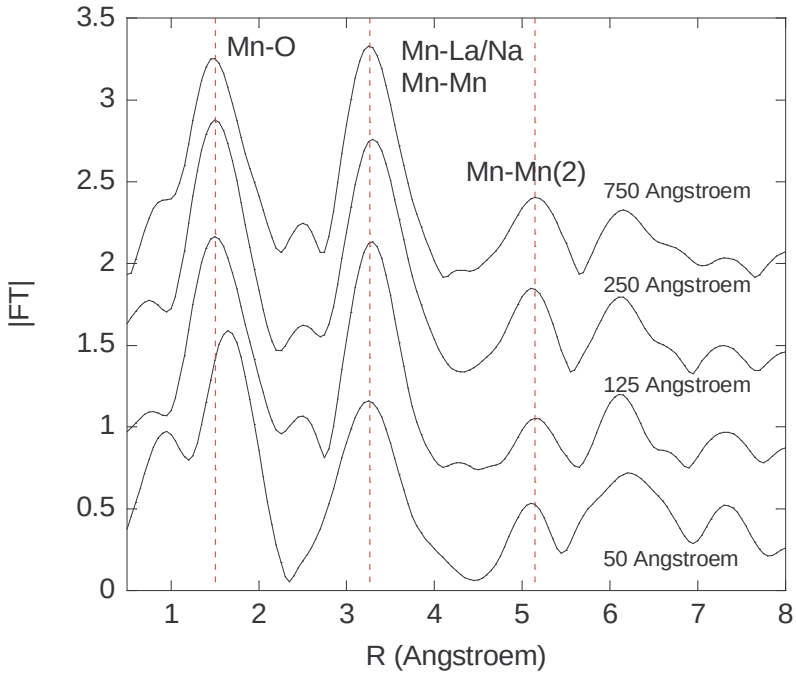

Figure 5.7: Fourier transform of the EXAFS signals reported in figure 5.6

5.5 Data analysis

The Fourier transforms of the EXAFS signal reported in fig. 5.6 show evident peaks up to 6 Å corresponding to contributions originating from coordination shells up to the sixth; this indicates the film having a high degree of crystallinity.

A quantitative analysis of the spectra was achieved using FEFF8 package [3]. Theoretical amplitude and phase functions were calculated for a cluster centered on the Mn absorber atom and extending up to 6 Å. The cluster was built with the ATOMS code [66], using a rhombohedral $R-3c$ structure and lattice parameters obtained from XRD refinements. The model spectrum of the cluster was fitted to the experimental EXAFS signal using the MINUIT minimization code from the CERN laboratories [1]. During the minimization process, the many body loss factor, S_0^2, and the experimental energy shift, ΔE, were fixed in order to reduce correlations and errors between free parameters; the same was done for the coordination numbers. Such policy is also good to evidence eventual difference or trends of the structural parameters from one sample to another. Therefore, each path is minimized using only two free parameters: the bond distance, R, and the Debye-Waller factor, σ^2. According to the Shannon theorem, the maximum number of independent parameters for spectra ranging in the k-interval $2 \div 11$ Å^{-1} is:

$$N_{ind} = 2 \cdot \frac{\Delta K \cdot \Delta R}{\pi} \simeq 26 \tag{5.1}$$

ΔK and ΔR are the inverse and direct space ranges respectively.

To obtain good fits, it was necessary to introduce contributes to the experimental signal up to the seventh coordination shell. We used 14 free fits parameters, well below the maximum number allowed by eq. 5.1. Furthermore, in the final analysis, we have performed the fits in the k-space, without Fourier filtering the data, to avoid distortions of the signal arising from the

Fourier filtering that could affect the refined structural parameters. Moreover, by proceeding this way we do not have the constraint on the maximum number of free parameters stated in eq. 5.1.

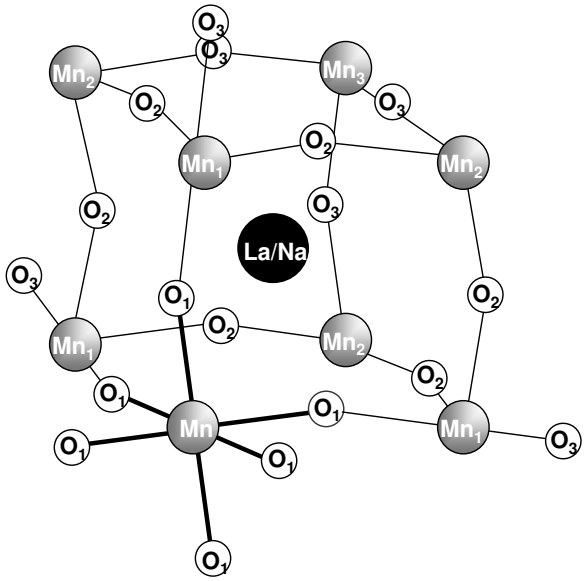

Figure 5.8: Sketch of the perovskite unit cell.

The following photoelectron path contributions to the signal were introduced to obtain good fitting results:

The main contribution to the EXAFS oscillations arises from the the first coordination shell at ~ 1.95 Å which is formed by six oxygen atoms. The photoelectron path is sketched in fig. 5.9. The theoretical distance as a function of the rhombohedral lattice parameter a is $a/2\sqrt{2}$. Mn ion is surrounded by oxygen octahedra (fig. 5.8), which is usually distorted due to the Jahn-Teller (JT) effect. Since our resolution is lower than the typical JT-induced distortions ($\sim 0.1 \div 0.2$ Å), we modeled this contribution with a single six-fold degenerate Mn-O distance including the fine structure of the JT-distorted distances in the Debye-Waller (DW) factor of the shell.

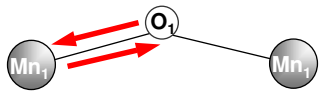

Figure 5.9: Pictorial view of the first shell photoelectron single scattering path (contribution from the Mn-O bond). The degeneracy of this path is equal to 6.

The second coordination shell includes the path between the Mn absorber atom and the La/Na ions at the center of the perovskite cell (fig. 5.10), having an average bond distance of $\sim 3.3\mathring{A}$. Since 15% of the ions occupying this site are Na^+ ions, we initially considered this contributions into the fits assuming two subshells: one made of La and the other of Na, and using a weighting free parameter x as:

$$x \cdot La + (1 - x) \cdot Na$$

It resulted that the main contribution arise from the Mn-La signal and that we could neglect the small Na contribution, so reducing the complexity of the fitting procedure.

Figure 5.10: Pictorial view of the second shell photoelectron single scattering path (contribution from the Mn-La/Na bond). The degeneracy of this path is equal to 8.

Other relevant contributions comes from the Mn-Mn bond length, corresponding to the edge of the cubic perovskite cell (fig. 5.11). The problem when taking into account this contribution is that there are two relevant

multiple scattering paths (Mn-O-Mn and Mn-O-Mn-O-Mn, see fig. 5.11) superimposed to the single scattering signal and the effective distances of these three contributions are very close to each other. Mainly for the limited signal to noise ratio of the spectra, it was difficult to obtain reliable information on these paths. In fact, these contributions enter in the fitting procedure in a way that results hard to control: the minimization program could find false minima by adjusting the distance (i.e. the frequency in the k-space) of each contribution in a way that the resulting signal reproduces the experimental one even with unphysical parameters. This is due to constructive and destructive interference phenomena between the different contributions. We tried to put constraints on the free parameters between different contributions. This reduces the number of free parameters so to reach a better control of the minimization process and more stable fits. Nevertheless, even following these procedure, the information obtained from these contribution is less reliable.

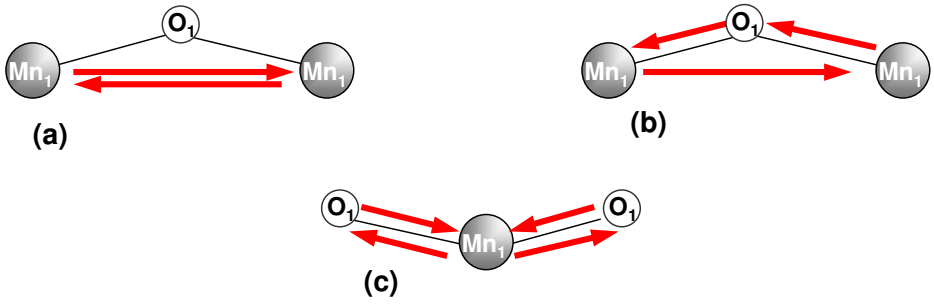

Figure 5.11: Pictorial view of the third shell photoelectron single-scattering and multiple-scattering paths. (a) Single-scattering Mn-Mn contribution lying on the edge of the cubic cell with degeneracy equal to 6. (b) Multiple-scattering (three body) Mn-O-Mn contribution with degeneracy equal to 12. (b) Multiple-scattering (four body) Mn-O-Mn-O-Mn contribution having degeneracy equal to 6.).

The last contribution that have been taken into account is the Mn-Mn single

scattering distance that connects two vertexes of the cubic cell through the diagonal a face (fig. 5.12). Even if very far, from the EXAFS point of view, this parameter is very important, being the lattice parameter (a) of the rhombohedral cell.

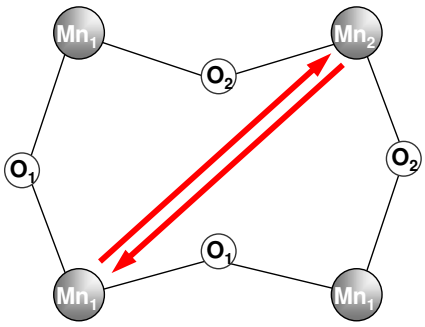

Figure 5.12: Pictorial view of the fourth shell photoelectron single scattering path. Contribution from the Mn-Mn bond lying on the diagonal of the face of the cubic cell. The degeneracy of this path is equal to 12).

5.6 XANES

The pre-edge structure of the Mn-K edge consists of two or three relatively small peaks that have (at least) partial 3d character. Since the 1s $\rightarrow$ 3d transitions are dipole forbidden, the pre-edge structure is generally ascribed as due to a mixture of quadrupole allowed 1s $\rightarrow$ 3d transitions and 1s $\rightarrow$ 3d dipole transitions that becomes allowed due to the hybridization of the 3d and 4p states. In bulk manganites two peaks labeled A1 and A2 in fig. 5.13, are present: recent calculations showed that the energy splitting of the A1 and A2 peaks is equal to the splitting of the e_g and t_{2g} states [22, 5]. In this scenario, the A1 peak is due to transitions into e_g states, while the A2 peak to transitions into t_{2g} states. A large change from the bulk situation is observed for the thinnest film (50 Å): in this case the A1 peak is shifted at lower energies and the width is much increased if compared to the bulk material. In addition, the A2 peak is shifted upward as a consequence of the larger energy splitting. As discussed in the work of Elvimov et al. [22], such an enhanced splitting of the A1 and A2 pre-edge peaks is the signature of the presence of a strong JT effect. This result well agrees with the strongly insulating nature of the 50 Å film. On the other hand, the thicker films XANES spectra does not change much with respect to the bulk spectra, accordingly with their transport properties.

5.7 EXAFS

Since all measurements were done in normal incidence (i.e. with the electric field oriented in the plane of the film), we are sensitive only to bonds lying in the plane of the film. As a matter of fact, the effective coordination number, often indicated as the weight, of each coordination shell, is a function of the angle, a_{ij}, between the polarization of the electric field and the absorber-scatterer bond direction, namely:

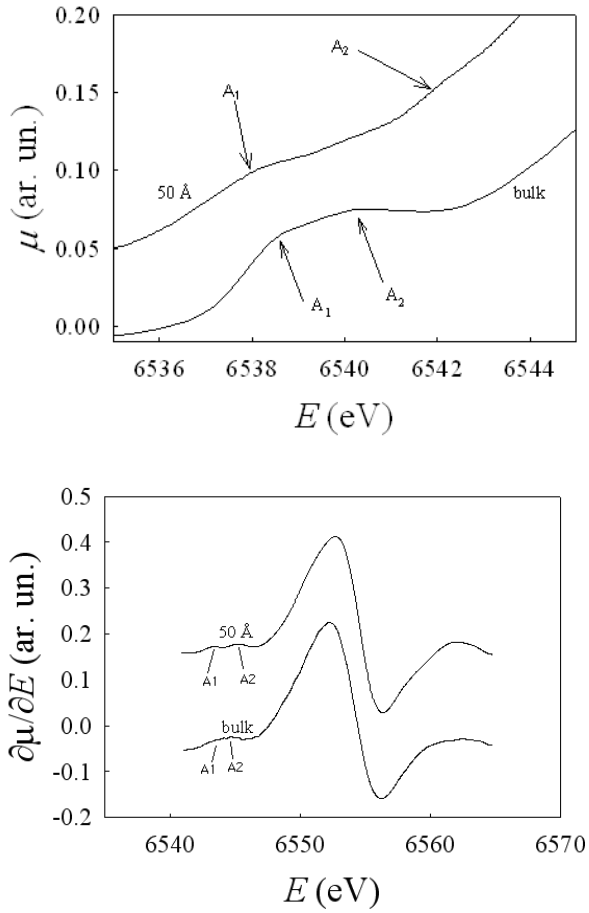

Figure 5.13: Upper figure: XANES region of the four samples. A spectrum of bulk sample is shown for comparison. The arrows indicate the pre-edge peaks labeled A1 and A2, discussed in the text. Lower figure: derivatives of the XANES region of the spectra reported in the upper figure. From the figure it can be noted the evolution of the pre-edge peaks A1 and A2 discussed in the text.

$$N_j^* = 3 \sum_{i=1}^{N_j} \cos^2 a_{ij} \tag{5.2}$$

For the first coordination shell, assuming a polarization vector of the incident radiation in the plane of the film (fig. 5.14 we have:

$$N^* = 3 * [\cos^2(45^o) + \cos^2(135^o) + \cos^2(225^o) + \cos^2(315^o)]_{\|} +$$

$$
\begin{aligned}
&+ \quad 3 * [\cos^2(180^o) + \cos^2(0^o)]_{\perp} = \\
&= \quad 3 * \left[\frac{1}{2} + \frac{1}{2} + \frac{1}{2} + \frac{1}{2}\right] + 3 * [0 + 0] = 3 * \frac{4}{2} + 3 * 0 = 6
\end{aligned}
$$

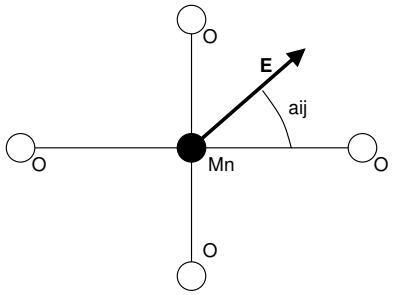

Figure 5.14: Relations between the bonds and the polarization of the electric field in the plane of the film.

Therefore, the effective coordination number of the first shell remain the same as for unpolarized radiation. Nevertheless, we have to remember that, in the present case, we are sensitive only to in plane bonds so that every consideration on the first shell local structure must be done keeping in mind that we are limited to the in-plane film structure [1]. In the following I am presenting the structural parameters extracted from the EXAFS refinements, focusing on the first coordination shell (Mn-O bond distance, coordination number and Debye-Waller factor). As widely discussed in the previous section, these are the key parameters in determining the magneto-transport properties (and also the more reliable parameters that can be obtained using this technique). I will also report the values found for the second shell (table 5.7). On the contrary, I will not report values for the third coordination shell; even if important to determine the structure, the strong multiple-scattering contributions (Mn-O-Mn, Mn-O-Mn-O, fig. 5.11) superimposed to the Mn-Mn

[1] Negligible contributes from out-of-plane bonds can occur due to lattice distortions (such as the octahedra tilting, common in manganites) or sample misalignment.

Thickness Å	$R_{Mn-O(1)}$ Å	$\sigma^2_{Mn-O(1)}$ Å^2
750	1.951 ± 0.004	0.0062 ± 0.0007
250	1.955 ± 0.007	0.0062 ± 0.0008
125	1.964 ± 0.007	0.0089 ± 0.0009
50	1.99 ± 0.01	0.0065 ± 0.0009

Table 5.1: First shell: Mn-O bond lengths and Debye-Waller factors as a function of the thickness.

single scattering path makes information less reliable. I will report fourth shell values (table 5.7), which, even if very far from the point of view of the EXAFS technique ($\sim$ 5.50 Å), are more reliable, being a pure single scattering path (Mn-Mn bond lying on the diagonal of the face, fig. 5.12). Due to the polarization effect, the extracted values for the first shell lengths reported in table 5.7 and in figure 5.15 are an average over the Mn-O bonds in the plane of the film. A trend, which can easily be detected as a function of the thickness of the film, is evidenced in the graph reported in figure 5.7, which shows that the average Mn-O bond distance grows up by reducing the film thickness. The overall change in the Mn-O distance is:

$$\Delta R = \frac{1.99 - 1.95}{1.97} \cdot 100 \sim 2\%$$

much greater than the lattice mismatch, which is around 0.5%. Therefore, lattice mismatch cannot be invoked as the only origin of the Mn-O bond stretching. Futher, since, as already pointed out, due to the in plane polarization of the incoming beam we are sensitive only to in-plane bonds, the observed elongation of the Mn-O distance must occur **in** the plane of the film.

The second shell values, reported in table 5.7, are almost the same for all samples (within the experimental error), with the exception of the thinnest sample, which shows a slightly reduction of the Mn-La bond length.

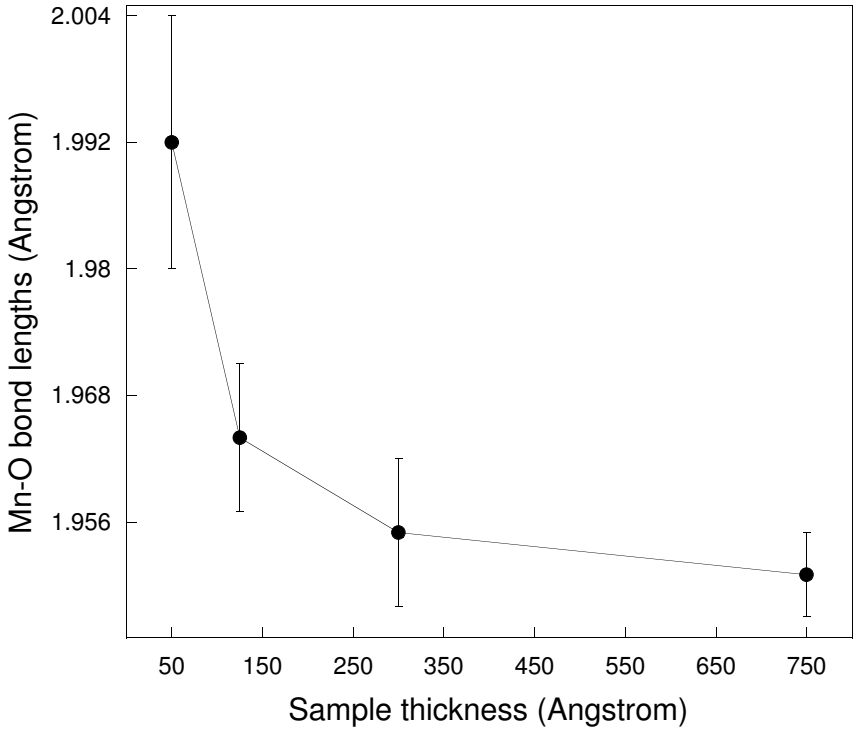

Figure 5.15: First shell (Mn-O) trend as a function of the thickness (values from table 5.7.)

The fourth shell values (table 5.7) remain almost unchanged for all the samples. This result indicates that the unit cell does not evolve by changing the thickness of the film. This may be understood assuming that a uniaxial Jahn-Teller distortion is accompanied by a rotation of the MnO_6 octahedra that compensate the elongation observed in the first shell bonds, maintaining almost unchanged the in-plane lattice parameters.

5.7.1 Discussion

According to the transport properties we can divide the studied samples in three types. The first includes thicker films, i.e. films with thickness > 200 Å; these have physical properties, metal to insulator transition temperature,

Thickness Å	$R_{Mn-La/Na}$ Å	$\sigma^2_{Mn-La/Na}$ Å^2
750	3.379 ± 0.008	0.0062 ± 0.0007
250	3.364 ± 0.014	0.0089 ± 0.0019
125	3.385 ± 0.009	0.0089 ± 0.0019
50	3.346 ± 0.026	0.0125 ± 0.0027

Table 5.2: Second shell: Mn-La/Na bond lengths and Debye-Waller factors as a function of the thickness.

Thickness Å	$R_{Mn-Mn(2)}$ Å	$\sigma^2_{Mn-Mn(2)}$ Å^2
750	5.52 ± 0.01	0.006 ± 0.001
250	5.50 ± 0.03	0.007 ± 0.003
125	5.53 ± 0.04	0.014 ± 0.007
50	5.50 ± 0.03	0.006 ± 0.003

Table 5.3: Fourth shell: Mn-O bond lengths and Debye-Waller factors as a function of the thickness.

Curie point and lattice structure, similar to the bulk material. The second type are the thinner films, with thickness < 100 Å; these films are insulating at all temperatures. The third includes films having thickness in the interval $100 \div 200$ Å. These films show transport and structural properties intermediate between the first and the second type.

5.7.2 Model

All our considerations on the studied samples are based on the model proposed by Lanzara et al. [40] that we have introduced in the first chapter. This model, which explain XAFS data on LCMO bulk samples, describes the insulating phase as composed of fully JT distorted (B) and partially JT distorted (A) Mn sites (fig. 5.16).

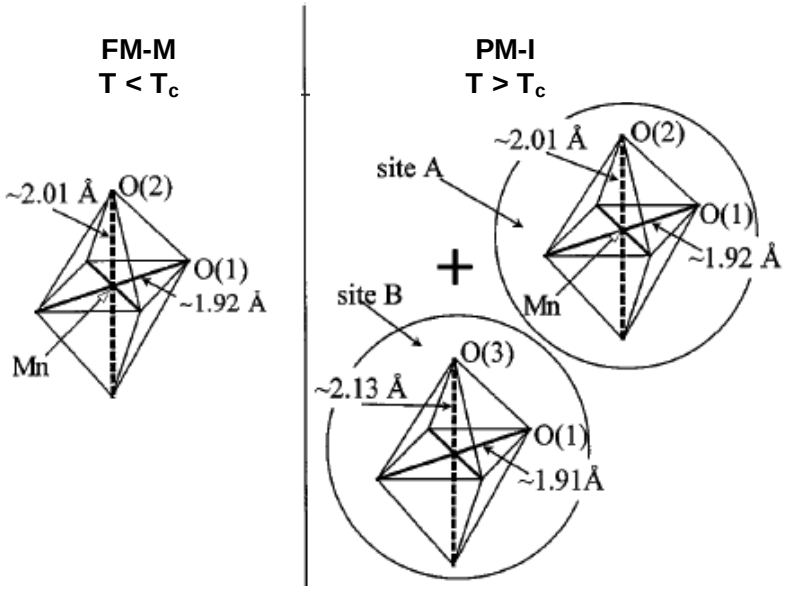

Figure 5.16: Pictorial view of the model proposed by Lanzara et al. [40]

In the metallic phase, only the low JT-distorted configurations (B) are present. This last hypothesis is supported by several evidences showing that the JT distortion is not completely removed in the metallic phase. In this

model the metal to insulator transition is viewed as a crossover between large JT polarons, in the metallic phase, and small JT polarons (insulating phase) corresponding to larger a electron-phonon coupling.

Hereafter we will refer to the c-axis as the one oriented out of the plane of the film. We will assume that the configurations reported in the model by Lanzara can be generalized to other manganites and that the values of for the first shell bond lengths differ very little from one system to another.

The JT effect is a uniaxial distortion of the MnO_6 octahedra resulting in four short equal Mn-O (planar) bonds ($\sim$ 1.92 Å) and two long (apical) bonds ($\sim$ 2.1 Å).

Hereafter we will refer to the long Mn-O bonds as to the "Long Jahn-Teller Component" (LJTC).

Since our spectra are limited to $k = 11^{-1}$, we cannot resolve the Mn-O bonds fine structure reported by Lanzara et al. We "see" a single average Mn-O distance ($\overline{R}$), the spreading of the distances being included in the static part of the Debye-Waller (DW) factor (which, for this reason, results increased). As discussed, we are sensitive to the only in-plane Mn-O bonds and, further, we assume, in the plane of the film, the short and the long Mn-O bonds having the same weight.

Keeping in mind these facts, we now calculate the expected average values of the Mn-O distance and Debye-Waller factor, which will be used to compare the experimental results.

In the following I will show that the experimental data can be explained by assuming the LJTC to lye in the plane of the film. With this assumption and also assuming the presence of 50% A sites and 50% B sites, following Lanzara's model, the situation is as follow:

$$\overline{R}_{MnO} = \frac{\overline{R}_A + \overline{R}_B}{2} = \frac{\frac{(2.13)+(1.91)}{2} + \frac{(2.01)+(1.92)}{2}}{2} = 1.99 \text{ Å}$$

where $\overline{R}_A$ and $\overline{R}_B$ represents the average in-plane Mn-O bonds for the con-

figurations A and and B, respectively.
For the DW factors we have:

$$\begin{aligned}\sigma^2 &= \frac{\sigma_B^2}{2} + \frac{\sigma_A^2}{2} = \\ &= \frac{(2.13 - \overrightarrow{R}_B)^2 + (1.91 - \overrightarrow{R}_B)^2}{2} + \\ &+ \frac{(2.01 - \overrightarrow{R}_A)^2 + (1.92 - \overrightarrow{R}_A)^2}{2} \simeq 0.006 \text{ Å}^2\end{aligned}$$

If, on the contrary, the LJTC lies **out** of the plane of the film, the average distance is equal 1.92 Åbecause both configurations (A and B) have short Mn-O bonds almost equal to this value and the LJTC (long Mn-O bonds) cannot be detected in our experiment due to the polarization effect. In this last case, the static *DW* factor is negligible.
We now apply the above model to the experimental results:
Thinnest film:

The results obtained for this samples are explained under the assumption that its thickness is lower than the dead-layer thickness. Therefore, the structural and transport properties of the whole film are the same of that of the dead-layer. For this sample, both the first shell average Mn-O distance and the *DW* factor ($\overline{R} = 1.992$ and $\sigma^2 = 0.0069$) agree well, within the experimental errors, with the mean values calculated from the model reported above: $\overline{R} = 1.99$ and $\sigma^2 = 0.006$. To match experimental values we have had to assume that the LJTC lies **in** the plane of the film.
Taking into account:

- The reduction of the out-of-plane lattice parameter observed on a 130 Å $La_{1-x}Na_xMnO_3$ (LNMO) film by Malavasi et al. [46] and reported in table 5.7.2;

Thickness Å	out-of-plane parameter a Å
700	3.876
250	3.878
130	3.851

Table 5.4: Out-of-plane lattice parameters (Mn-Mn bond distance) found by XRD measurements by Malavasi et al. [46]

- the lattice mismatch, which is about 0.5%;
- the stretching of the Mn-O bond distances as a function of the thickness, found in the present work, reported in table 5.7 and evidenced in graph 5.15.

We can propose the following scenario:
The positive lattice mismatch between the substrate and the manganite film is the origin of the out-of-plane lattice parameter reduction in the thinnest films. In fact, the entity of the compression of the out-of-plane parameter (3.851 vs 3.876Å, from table 5.7.2) well agrees with lattice mismatch ($\sim 0.5\%$).
On the other hand, the overall stretching of the in-plane Mn-O distances, as a function of the thickness, of about 2% (from $\sim$ 1.95 Å for the 250 and 750 Å thick to $\sim$ 1.99 Å for the 50 Å thick), is much greater than the film/substrate lattice mismatch. An explanation can be attempted by considering the transport properties of this sample. At this thickness, the film is insulating at all temperatures. In manganites this scenario corresponds to the presence of highly JT-distorted MnO_6 octahedra (the B sites of Lanzara's model). If we suppose the presence of a large JT distortion, we can attribute the increase of the average Mn-O bond distance to the lengthen of the two apical distances (the LJTC defined above) and the compression of the remaining ones, in the typical JT fashion.

On the other hand, keeping in mind that we are sensitive only to the in plane bonds, we must suppose the LJTC oriented **in** the plane of the film.
An fact supporting such assumption is the observed reduction of the lattice parameter occurring out of the plane of the film; this would suppress the stabilization of the LJTC in this direction. Viceversa, the expansion of the lattice parameter **in** the plane of the film due to the lattice mismatch, would favor the development of the LJTC in this direction. This hypothesis is supported by similar findings in a work of Salvador et al. [72].

Thicker films:

250 and 750 Å thick films can be treated under the assumption that the contribution of the dead-layer is negligible (less than 10%) so that their structure is mainly bulk-like. The average nearest neighbor distance (1.95 Å) is in excellent agreement with the value found by EXAFS measurements on bulk samples of LCMO [48], corresponding to an unstrained lattice structure. According to the model above, assuming an in-plane orientation of the LJTC, we should expect a distance ($\sim 1.99\mathring{A}$) longer than the one observed (1.964 ± 0.007 Å). This can be explained by supposing that, as the film structure relax above a certain thickness, there is no more a preferred orientation for the *JT* distortion. Under this assumption, we can use the model above considering half sites having the LJTC oriented in the plane of the film and the remaining sites with this component oriented out of the film-plane.
Quantitatively we have:

$$\begin{aligned} \overline{R} &= \frac{\cdot(0.5 \cdot \overline{R}_B + 0.5 \cdot \overline{R}_A)_\perp}{2} + \frac{\cdot(0.5 \cdot \overline{R}_B + 0.5 \cdot \overline{R}_A)_\parallel}{2} = \\ &= \frac{\cdot\left(\frac{2.13+1.92}{2} + \frac{2.01+1.92}{2}\right)_\perp}{2} + \end{aligned}$$

$$+ \quad \frac{\cdot \left(\frac{1.92+1.92}{2} + \frac{1.92+1.92}{2}\right)_{\parallel}}{2} \simeq 1.955 \text{ Å} \tag{5.3}$$

where the sign $\perp$ and $\parallel$ represent the LJTC orientation, respectively out of the film-plane and in the film-plane. Such value is in very good agreement with the observed ones (1.951 and 1.956 Å). Also the value of the DW factor supports this hypothesis; in fact, as already evidenced, in the case of out-of-plane orientation of the LJTC, the resulting static contribution to the DW factor is negligible. The remaining contribution comes from the in-plane orientation of the LJTC, which has been calculated above and well agrees with the observed value within the experimental error.

Intermediate thickness:

For this sample we find a value for $\overline{R}_{MnO}$ of $\sim$ 1.965 Å, about half way between the thicker (1.95 Å) and the thinnest (1.99 Å) samples values. The value of the Debye-Waller factor (~ 0.009 Å^2), instead, is significantly higher with respect both the thicker and the thinnest samples. This result can be explained by supposing that the observed distance and DW values result from the superposition of the contributes arising from the strained dead-layer and from the rest of the film. In fact, for the 125 Å thick film we suppose that about 50% (i.e. no less than 50 Å) of the total signal arises from the dead-layer, the remaining part coming from the relaxed, bulk-like, upper part of the film. Therefore, the observed value of the Mn-O bond distance is nothing else than the average between the values observed for the thickest and thinnest samples. Quantitatively:

$$\begin{aligned} \overline{R}_{\mathrm{MnO}}(125\text{Å}) &= \frac{\overline{R}_{\mathrm{MnO}}(50\text{Å}) + \overline{R}_{\mathrm{MnO}}(750\text{Å})}{2} = \\ &= \frac{1.992 + 1.951}{2} \simeq 1.97 \text{ Å} \end{aligned}$$

which is in very good agreement with the experimentally observed value (1.967 Å).

Further, the spreading of the first shell distances results in an higher value of the DW factor. A quantitative determination of the Debye-Waller factor is less straightforward. To build a model that retrieves the observed value we have to consider two gaussian distributions centered in ~ 1.95 and ~ 1.99 Å and having the DW of the thicker and of the thinnest sample, respectively. The resulting σ^2 can be estimated as the sum of the square of the Debye-Waller factors from the thinnest and thicker samples plus the square of the difference between the center of the two distribution functions:

$$\sigma^2(125\text{Å}) = (0.00621)^2 + (0.00655)^2 + (1.992 - 1.951)^2 \simeq 0.01\text{Å}^2$$

within the experimental error, this value is in agreement with the experimental value reported in table 5.7.

5.8 Conclusions

Our data mainly suggest the presence of a strong static JT effect in the thinnest film. Moreover, the entity of the JT distortion follows an increasing trend as a function of the film thickness, becoming less important for thicker films. In our opinion, the large distortion in the local structure observed in the thinnest film, is induced by the disorder due to the dead-layer nature. This disorder may arise from different Mn local environments due to different terminations types present in commercial $SrTiO_3$ substrates (SrO and TiO) as proposed in the work of Bibes et al. [9]. Further disorder arises from the lattice-mismatch, which, nevertheless, cannot be invoked as the unique cause of the change observed in the local structure due its little size compared to the first shell distances elongation. The overall effect of this combined

disorder is a breaking of some double-exchange paths and the consequent charge localization, which, on the other hand, induces the stabilization of a static *JT* effect. This scenario supports the hypothesis of an insulating nature arising from a modification of the carrier density in the interface region. An interesting property of the model that we have proposed to explain the experimental data, is the reversal of the long component of the Jahn-Teller effect (LJTC), which, in the case of thickness of the order of the dead-layer, develops in the film plane. In thicker films the relaxation of the strain removes constraints that forced the LJTC to stay in the plane of the film and, since this component does not has anymore a preferred orientation, the material returns similar to the bulk one. Our work gives a microstructural characterization of sodium based manganites thin films as a function of the thickness, which improved the knowledge of the structure of very thin films. In fact, even if *JT* distortion has been previously inferred by many experimental works, it has never been observed and quantified directly. Moreover we have given important information on the evolution of the local structure as a function of the film thickness.

Chapter 6

The $Sr_2FeMo_xW_{1-x}O_6$ series

6.1 Introduction

In this chapter I will present the X-ray absorption (XAS) data collected on $Sr_2FeMo_xW_{1-x}O_6$ samples with different Mo concentrations.
As exhaustively described in chapter two, the transport properties of Sr_2FeMoO_6 are influenced by the chemical order of the lattice, i.e. by the perfect (or not) alternation of the occupancy of the B and B' sites (where, in our case, B is Fe and B' W or Mo) of the double perovskite structure. The W doping increases the chemical order and, as a consequence, the Curie point rises up (up to 450 K).
Sr_2FeMoO_6 and Sr_2FeWO_6 have opposite transport properties, the first being a half-metallic ferromagnet (HMFM) in a wide range of temperatures (up to 450 K) and the second an antiferromagnetic insulator (AFM-I) at all temperatures. At a Mo concentration of $x \sim 0.25$ a metal to insulator transition (MIT) occurs.
Further, as in manganites, transport properties of $Sr_2FeMo_xW_{1-x}O_6$ largely depend on the local lattice structure (Fe-O and B'-O bond angles and lengths) which has not been directly probed yet. For this reason, a local probe tech-

nique such as EXAFS is a suitable way to study these materials.

6.2 Sample preparation

All the double perovskites compounds studied in this thesis were prepared at the Indian Institute of Science of Bangalore (India). Sr_2FeMoO_6 ($x = 1.0$) was prepared using the solid-state route reported in [37, 54]. The starting materials, $SrCO_3$, MoO_3 and Fe_2O_3, were mixed thoroughly and calcined at 900^0C in air for three hours and then reduced in a flow of 10% H_2 in Ar at 1200^0C for two hours. The other members of the series $Sr_2FeMo_xW_{1-x}O_6$, with $x = 0.8, 0.6, 0.3, 0.2, 0.15, 0.05, 0$, were prepared by the melt-quenching method under an Ar atmosphere using the following reaction:

$$\begin{aligned} 12\ SrCO_3 \ &+\ 3\ Fe_2O_3 + x\ (5\ MoO_3 + Mo) + (1 - x)\ (5\ WO_3 + W) = \\ &=\ 6\ Sr_2FeMo_xW_{1-x}O_6 + 12\ CO_2. \end{aligned}$$

After the synthesis, all compounds were annealed at 1300^0C for six hours in an Ar atmosphere in order to achieve a homogeneous phase. Since the oxidation of the grain surfaces influences the transport properties, the samples were sealed and shipped in vacuum quartz tubes to maintain their original properties.

6.3 Sample characterization

Energy-dispersive analysis of x-rays (EDAX) confirmed the homogeneous phase for different grains of the samples. X-ray diffraction (XRD) data showed the presence of a single phase and a high degree of ordering of the Fe and Mo cation sites [76] following an increasing monotonic trend from 95% in Sr_2FeMoO_6 to 100% in Sr_2FeWO_6 . The electrical resistivities (ρ) of

all of the samples are shown in figure 6.1 on a logarithmic scale as a function of the temperature; the plots clearly show two regimes. The first group with $x \geq 0.3$ have low resistivities and exhibit metallic behavior, while the compositions with $x \leq 0.2$ are insulating. These results clearly establish a metal-insulator transition as a function of the composition in the range $0.3 > x_c > 0.2$. This value of the critical composition is in agreement with that reported in [37]; however, the critical composition $0.5 > x_c > 0.4$ reported in [55] is significantly different from the present finding. This is most probably due to the grain boundary which influence the transport properties of these sintered samples substantially. For example, the resistivity of the composition with $x = 0.6$ is higher than that of all the other samples with $x > 0.3$. This is likely due to a higher contribution of the grain boundaries in the $x = 0.6$ sample. We also note that the resistivities of all these metallic samples are rather large ($10 \div 100\Omega$·cm; the values are reported to be within $1 - 100\Omega$·cm in [55, 37]), once again indicating a significant contribution from grain boundaries in these sintered polycrystalline samples. We have also observed a time-dependent change in the resistivity of the metallic samples. Though the magnitude of the resistivity does not change significantly with time, the temperature coefficient of resistivity tends to change sign over a period of time, indicating a slow oxidation of grain surfaces and introduction of an insulating grain boundary layer. This possibly explains why in the earlier study the critical composition was thought to be between 0.4 and 0.5. The resistivity data presented here were collected from freshly prepared samples within a day of the synthesis.

6.4 Crystallographic structure

Diffraction data (mainly from the work of Sanchez et al. [73]) will be used both as a starting point to generate the atomic clusters for the calculation of

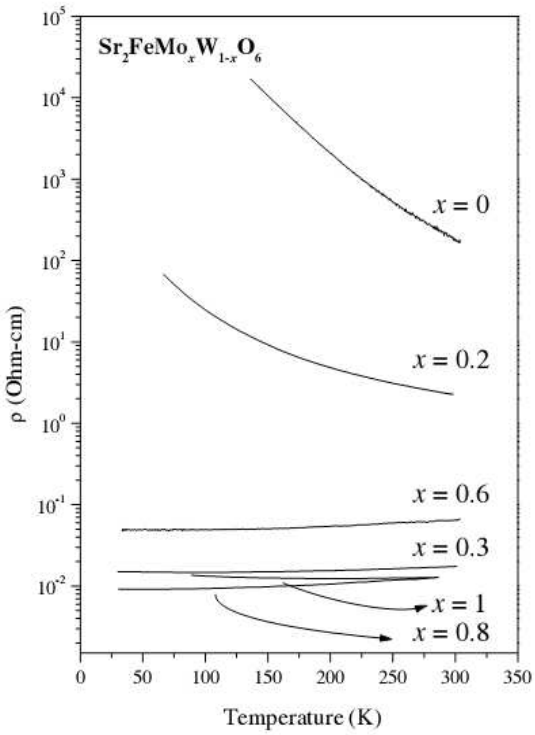

Figure 6.1: Electrical resistivity (ρ) of $Sr_2FeMo_xW_{1-x}O_6$ as a function of temperature, plotted a logarithmic scale.

EXAFS back-scattering amplitudes and phases, and to compare our results to the crystallographic values. In order to compare correctly EXAFS and diffraction data, a few points have to be considered. Due to the lower resolution of our measurements with respect to diffraction data, bond distances belonging to same coordination shells must be averaged. For example, due to the tetragonal distortion of the cell, the first shell, which for Fe, Mo and W absorbers, is formed by oxygen octahedra, is generally splitted into two longs (apical) and four short (planar) bonds. Since this splitting is lower than the resolution that we can achieve, we "see" a bond distance that is the weighted average of the apical and the planar bonds. Only once correctly averaged, diffraction data can be compared with our results. It is also worth to remember that the diffraction technique gives a direct measure of

Path	Fe-O	Mo/W-O	Sr-O	Fe/Mo/W-Sr	Fe-Mo/W Sr-Sr(1)	Sr-Sr(2)
Degeneracy	6	6	12	8	6	12
Shell		1^{st}		2^{nd}	3^{rd}	4^{th}
Units				Å		
$x = 1$	1.996	1.954	2.689	3.414	3.941	5.574
$x = 0.8$	2.004	1.951	2.792	3.418	3.947	5.582
$x = 0.5$	2.023	1.944	2.800	3.426	3.956	5.594
$x = 0.2$	2.058	1.937	2.836	3.439	3.971	5.616
$x = 0$	2.079	1.932	2.821	3.446	3.978	5.627

Table 6.1: Bond distances calculated from the work of Sanchez et al. [73] (figure 6.2) and averaged for comparison with EXAFS data. Sr-Sr(1) and Sr-Sr(2) corresponds to the a and $a \cdot \sqrt{2}$ distances respectively, where a is the lattice parameter.

the lattice parameters. The bond distances are indirectly calculated from the knowledge of these parameters and of the correct space group (figure 6.2). For this reason, diffraction can only distinguish between bond distances belonging to different crystallographic sites. This is why, for example Mo-O and W-O bond distances are reported together in table 6.4 (as the Fe-Sr, Mo-Sr, W-Sr bonds and the Fe-Mo, Fe-W ones). On the contrary, using the EXAFS it is possible to distinguish between these bond distances simply changing the absorber atom (i.e. the incident photon energy). Finally, it should be also noted that Sanchez et al. used samples with slightly different Mo concentrations with respect to ours. This makes harder the comparison of the data.

As anticipated in chapter two, Sanchez et al. found that the compounds with $x \geq 0.5$ (which is the composition nearest to the critical one ($x \sim 0.15$) they have probed) have a tetragonal symmetry, I4/m ($a = b \neq c$, $\alpha = \beta = \gamma = 90^0$), while compounds with $x \leq 0.2$ belong to the monoclinic space group

Sample	$x = 0$	$x = 0.2$	$x = 0.5$		$x = 0.8$	$x = 1$
$I4/m$				$P2_1/n$		
a (Å)	5.56846(5)	5.5753(1)	5.58700(9)	a (Å)	5.6347(3)	5.6508(1)
b (Å)	5.56846(5)	5.5753(1)	5.58700(9)	b (Å)	5.6082(3)	5.6136(1)
c (Å)	7.9004(1)	7.9122(3)	7.9328(2)	c (Å)	7.9252(4)	7.9425(2)
				β (deg)	90.05(1)	90.021(5)
V (Å^3)	244.976(4)	245.94(1)	247.618(9)	V (Å^3)	250.44(2)	251.944(9)
Sr 4d(1/2 0 1/4)				Sr 4e(x y z)		
B (Å^2)	0.93(2)	0.77(6)	0.86(2)	x	1.000(1)	0.9990(7)
				y	0.009(1)	0.0129(8)
				z	0.247(2)	0.2491(9)
				B (Å^2)	1.10(3)	0.87(3)
Fe 2a(0 0 0)				Fe 2d(1/2 0 1/2)		
B (Å^2)	0.81(9)	0.5(3)	1.5(1)	B (Å^2)	1.0(1)	0.36(8)
Mag. mom. (μ_B)	1.7(8)	2.6(3)	1.0(1)	Mag. mom. (μ_B)	—	—
Mo 2b(0 0 1/2)				Mo 2b(1/2 0 0)		
B (Å^2)	0.0(1)	0.4(4)	−0.8(8)	B (Å^2)	0.2(2)	0.6(2)
Mag. mom. (μ_B)	−0.8(3)	−0.2(2)	—	Mag. mom. (μ_B)	—	—
O1 4e(0 0 z)				O1 4e(x y z)		
z	0.254(1)	0.255(3)	0.2622(6)	x	0.0441(8)	0.0473(5)
B (Å^2)	1.00(5)	0.9(1)	0.72(7)	y	0.511(1)	0.496(1)
				z	0.257(2)	0.259(1)
				B (Å^2)	0.8(1)	0.97(9)
O2 8h(x y 0)				O2 4e(x y z)		
x	0.2719(8)	0.272(2)	0.2751(8)	x	0.719(1)	0.719(1)
y	0.2332(6)	0.233(2)	0.2281(8)	y	0.261(2)	0.261(1)
B (Å^2)	1.05(2)	0.89(8)	1.14(4)	z	0.0286(8)	0.025(1)
				B (Å^2)	1.2(2)	1.0(2)
				O3 4e(x y z)		
				x	0.248(1)	0.242(1)
				y	0.235(2)	0.224(1)
				z	0.984(1)	0.976(1)
				B (Å^2)	1.2(1)	1.1(2)

Figure 6.2: Relevant crystallographic information on the $Sr_2FeMo_xW_{1-x}O_6$ series from the work of Sanchez et al. [73]. Note that, contrary to our convention (x = Mo level) the x of the figures refers to the W concentration.

P21/n ($a \neq b \neq c$, $\alpha = \gamma = 90^0 \neq \beta$). Therefore, a structural transition from tetragonal to monoclinic symmetry is expected at some x. The evolution of the lattice parameters a, b and c and of the cell volume, V, with the W content is reported in figure 6.4. An overall continuous cell expansion upon

W substitution is observed. They attempted a microscopic explanation of the structural evolution as a function of the composition x which is reported in the caption of figure 6.4.

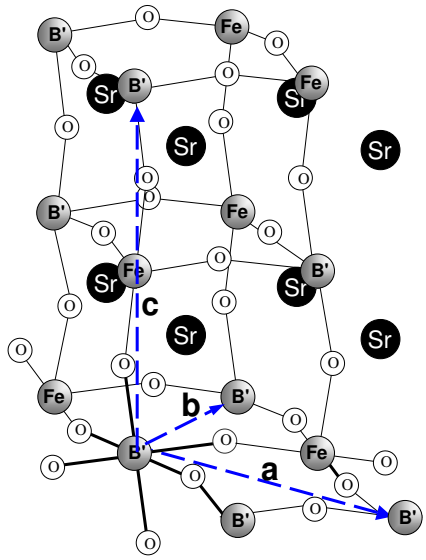

Figure 6.3: Double-perovskite cubic cell. The dashed arrows indicate the lattice vector a, b and c. Note that $a = b \neq c$ for the tetragonal cell (I4/m) and $a \neq b \neq c$ for the monoclinic cell (P21/n).

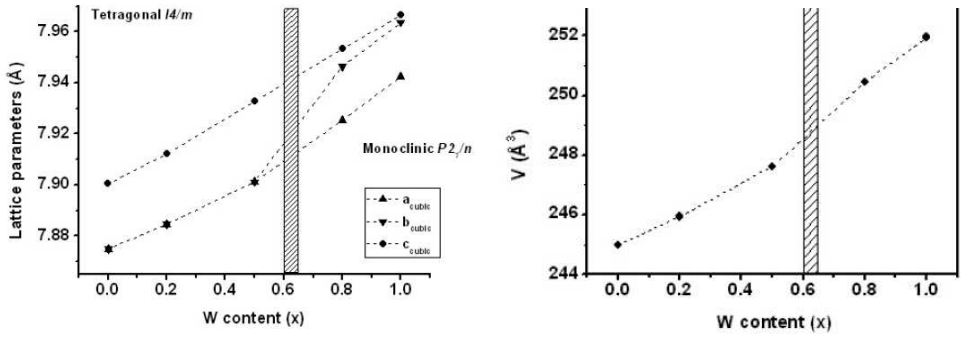

Figure 6.4: Left panel: Evolution of the lattice parameters as a function of the concentration. Right panel: evolution of the unit cell volume (from Sanchez et al.). Note that, contrary to our convention (x =Mo level) the x of the figures refers to the W concentration.

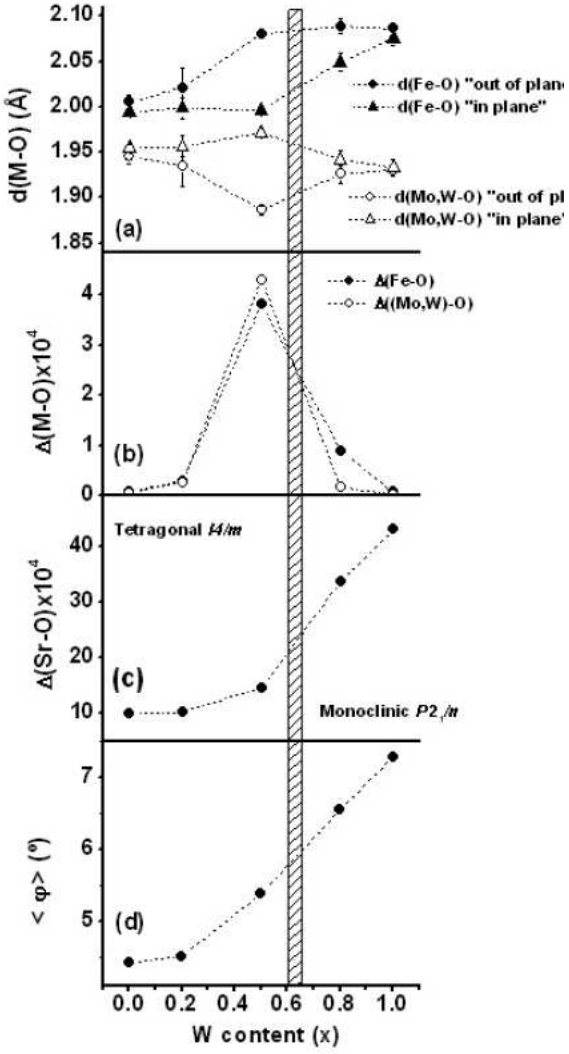

Figure 6.5: Evolution of structural parameters as a function of the W concentration (from Sanchez et al.): "after an Fe atom has received the $5d^1$ electron transferred from a substituting W atom, the FeO_6 octahedra expands along the out-of-plane direction, while the $(Mo/W)O_6$ octahedra contracts (a). The Coulomb energy gain is compensated, in the basal plane, by increasing the antiphase rotation of the octahedra along the c axis (d), keeping the in plane bond distances almost unchanged (a). This provokes a strong distortion of the BO_6 octahedra (b) and a strong increase in the metal-oxygen bond tensile stress with increasing x. At high substitution level, $x < 0.4$, the BO_6 octahedra tilt to relax the bond stress and the compound undergoes a change of symmetry. This can be seen in (a) and (b), where is evident that the distortion is minimized after the structural phase transition. This translates into a distortion of the Sr environment (c), in order to accommodate the changes in the metal-oxygen octahedra within the 12 Sr-O bonds. The distortion factor reported in figure 8b is calculated as: $D = 1/N[dn - < d >]2/ < d >$ where n runs over the number of ligands N, d_n denotes a particular metal-oxygen distance and $< d >$ is the average metal-oxygen distance." Bond distances reported in the figure are not averaged as discussed above. Note that, contrary to our convention (x =Mo level) the x of the figures refers to the W concentration.

6.5 Experimental

To obtain a complete picture of the microstructure of the $Sr_2FeMo_xW_{1-x}O_6$ compounds, the absorption edges of all the metallic elements were investigated. The monochromator were equipped with a couple of 311 Si crystals. The energy resolution (taking into account a main slit vertical aperture of 1mm) is around 0.5 eV at the Fe and W edge energies (7112 and 10207 eV) and of 1 eV at the Sr and Mo (16105 and 20000 eV). Silver coated mirrors have been used to reject higher harmonic contributions at the Fe edge while, at higher energies (> 8.5 KeV) platinum/palladium coated mirrors were used. The photon beam was delimited by means of slits placed at about 1 m from the sample; this was mounted on a copper holder and cooled down to the liquid nitrogen temperature (77 K) to reduce the thermal contribution to the Debye-Waller factor. All the measurements were performed in transmission geometry, the photon beam before and after the sample was measured by the means of two ionization chambers. The chambers were filled with different gas types (nitrogen, argon, krypton) and pressures in order to absorb 20% of the incident beam and 80% of the transmitted one. Typical photon flux was of about 10^9 at 7KeV and 10^{10} at 20KeV.

Great care have been put preparing the samples to fulfill all the requisites necessary to achieve an as high as possible signal to noise ratio. The first requirement is to obtain an optimal compromise between the total absorption of the sample and the height of the edge step. The total absorption (μ_{tot}) is a function of the photon absorption cross section of the whole compound and of the thickness of the sample (d). It was chosen accordingly with the absorption ratio of the ion chambers ($\mu_{tot} = \ln(20\%/80\%)$) in order to obtain a detectable transmitted beam and an as-high-as-possible edge step. With this condition, the optimal sample weight (W) can be calculated as follow:

$$W = \frac{Jump}{\Delta S}$$

where ΔS is the difference between the pre-edge (σ_t^+) and post-edge (σ_t-) photoabsorption cross sections of the compound, and $Jump$ is the edge step:

$$Jump = \frac{\Delta S}{\sigma_t^+} \cdot \mu \cdot d$$

The total photoabsorption cross section can be calculated summing the single elements cross sections multiplied for the weight percentage of the element:

$$\sigma_t^+ = \sum_{i=1}^{N} \sigma_i^+ \cdot weight(\%)$$

where N is the number of elements in the compound, σ_i^+ is the post-edge cross section for the i-th element and the weight percentage is calculated as:

$$weight(\%) = \sum_{i=1}^{N} \frac{A.W.(i)}{M.W.} \cdot n(i)$$

$A.W(i)$ and $M.W.$ being the atomic weight of the i-th element and the molecular weight of the compound, respectively and $n(i)$ the stoichiometric index of the i-th element. To simplify the calculation of the optimal weight for each sample and edge a useful FORTRAN code has been written (JUMP), which contains a full card information of each element (atomic weight, cross section, density).

The second requirement is to have a sample as homogeneous as possible. This condition is very important in transmission geometry since the intensity of the transmitted beam can be distorted by the presence of holes in the sample. To fulfill this condition we ground the samples in a fine powder, suspending an equivalent of the optimal sample weight in ethanol. We kept the solution in a ultrasonic apparatus to disaggregate eventual clusters and then deposited the solution on a 0.5 micron millipore membrane. In this way,

we obtained a homogeneous deposition that we then covered with Kapton tape to protect and limit oxidation.

6.6 XANES results

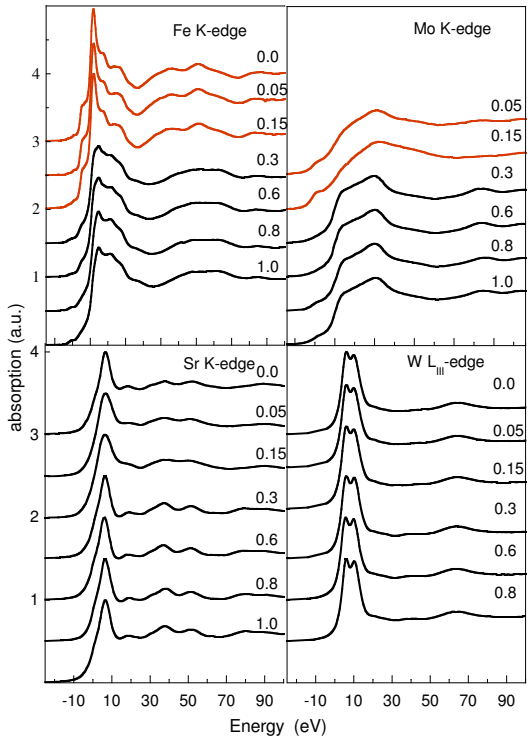

Figure 6.6: XANES region of the pre-edge subtracted and normalized XAS spectra of all the samples at the four absorption edge investigated. Note the large differences between the features of the spectra in the HMFM region ($x \geq 0.3$) respect to the AFM-I phase ($x \leq 0.15$) for the Fe and Mo edges. Also evident at these edges are the pre-edge peaks appearing in the insulating phase. On the contrary XANES spectra at W and Sr edges remain the same for the whole concentration range.

Figure 6.6 reports the XANES region of the absorption edges investigated (Fe, Mo, Sr, W). It can be immediately noted the changes in the features of the spectra at the Fe and Mo edges while crossing the critical concentration of Mo (x_c). More in detail, the spectra below the critical concentration ($0 < x < x_c$), at Fe and Mo edges, have the same features of the Sr_2FeWO_6 ($x = 0$) end compound. On the other side, spectra of intermediate compounds having $1 > x > x_c$ have the same features of the Sr_2FeMoO_6 ($x = 1$) end compound. Finally, XANES spectra at W and Sr edge do not show any significant change for all values of x. These observations confirm that Mo and Fe play a relevant

role in determining the macroscopic properties of these materials.
A more quantitative analysis of the XANES spectra can be attempted by trying to reproduce the spectra of the intermediate compounds by the means of a linear combination of the end compounds spectra:

$$\mu(\overline{x}) = \alpha \cdot \mu(x = 1) + (1 - \alpha) \cdot \mu(x = 0)$$

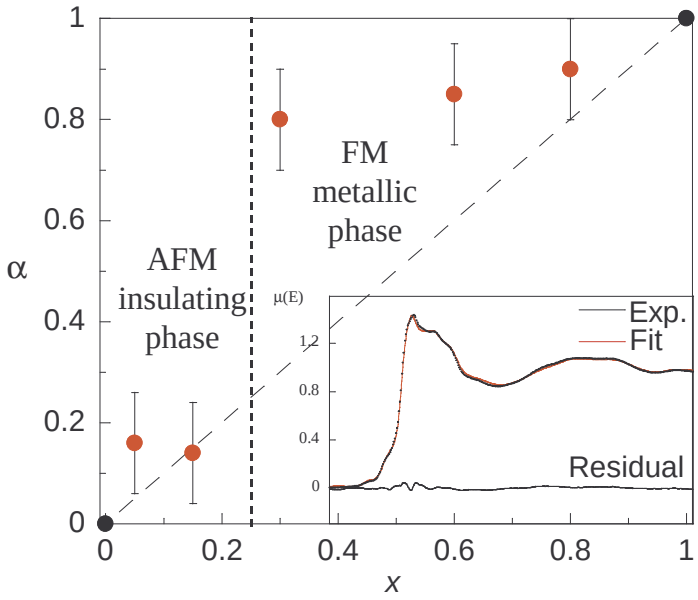

Figure 6.7: This figure reports the values of the weight parameter α used to fit the Fe edge XANES spectra of the intermediate compounds by means of a linear combination of the XANES spectra of the end compounds ($x = 1$ and $x = 0$). The inset reports the experimental absorption spectrum of the $x = 0.6$ compound together with the fit obtained using the linear combination 6.6 and the residual as an example.

where α is a weighting parameter ranging between 0 and 1 and $\mu(\overline{x})$ is the absorption spectrum of the sample having Mo concentration equal to $\overline{x}$. The inset of figure 6.7 show how good the intermediate compounds spectra can be reproduced by such a linear combination (it is worth to note that the same procedure does not work for manganites). Figure 6.7 reports the values of the weight parameter α. This parameter is a measure of the

amount of Sr_2FeMoO_6 ($x = 1$) end compound spectra necessary to reproduce an intermediate compound spectra. From a structural point of view it can be viewed as a measure of the local structure type, i.e. Sr_2FeMoO_6 or Sr_2FeWO_6 -like. Remembering that the Sr_2FeMoO_6 end compound contains only Fe^{3+} ions ($Sr_2^{2+}Fe^{3+}Mo^{5+}O_6^{2-}$), while, the Sr_2FeWO_6 one only Fe^{2+} ions ($Sr_2^{2+}Fe^{2+}W^{6+}O_6^{2-}$), from an electronic point of view it can be interpreted also as a measure of the Fe^{3+} ions concentration. In the following both interpretations will be considered for α.

Supposing that α is a measure of the Fe^{3+} content, it is evident from fig. 6.7 that its trend diverges from the one expected on the basis of a simple model which attributes changes to ions accordingly to the stoichiometric formula; in such case α would follow the same trend as the nominal Mo concentration x. Therefore, the concentration of Mo, which is supposed to be in the 5+ state, should be equal to that of Fe^{3+} (α). On the other hand, the W concentration $(1-x)$ should be equal to the Fe^{2+} concentration $(1-\alpha)$; such expected trend is evidenced in fig. 6.7 by the straight dashed line connecting the points corresponding to the abscissa $x = 1$ and $x = 0$. The observed trend of the α parameter indicate an excess of Fe^{3+} sites in the HMFM phase ($x > 0.25$) with respect to their nominal concentration. The Fe^{3+} concentration has an almost constant value of about 90%, between the experimental error bars. Crossing the critical concentration the weight parameter abruptly decrease to values very close to the nominal concentrations of the insulating samples. From a structural point of view the weight parameter can be viewed as a measure of the two kind of local structure around the Fe absorber. Following this interpretation, the trend of the α parameter show that the local structure in the whole HMFM phase is almost completely Sr_2FeMoO_6 -like. On the other hand, in the insulating phase we cannot discern weather the local structure is an admixture of nominal concentrations of the two end compound local structures or if is mainly Sr_2FeWO_6 -like.

This semi-quantitative considerations on the XANES region of the spectra can help to understand the mechanism of the metal-to-insulator transition (MIT), which is one of the aims of this work. The two scenarios proposed (Kobayashi et al. [38]) to explain the MIT described in chapter two (valence transition and percolation), have to be compared with the following experimental results:

- The XANES spectra features does not change at the W-edge in the whole concentration range.
- At the Fe-edge and Mo-edges, the local structure remains that of the Sr_2FeMoO_6 end compound until the critical concentration. Then it rearranges to that of the other end compound: Sr_2FeWO_6 .
- In the insulating phase (low x values) a pre-edge peak appears in the XANES spectra at the Mo edges (fig. 6.6).

The first experimental observation is against the valence transition scenario because we do not observe any even small change in the W-edge XANES spectra in the whole concentration range; thus, we can exclude that W valence state changes from 6+ to 5+ while crossing the critical concentration. On the other hand, the second point seems to be against the percolation scenario, which would predict a trend of the weight parameter α that reproduces the nominal concentration values ($\alpha(x) = x$), in disagreement with the observed one (see fig. 6.7). In this sense, the observed evolution as a function of x gives evidence of a valence transition at the critical concentration.
The third result, gives an information on the valence state changes on the Mo and Fe sites. Looking at the evolution of the pre-edge shape of the Fe K-edge XANES spectra, we can note a "shoulder" appearing in the insulating phase. In many systems, this is a signature of the presence of Fe^{2+} charge states; therefore we attribute its appearance to the change of the valence state of

the Fe from 3+ to 2+. On the other hand, the Mo K-edge spectra show the appearance of a pre-edge peak in the insulating phase. This peak indicates the presence of free states in the Mo electronic levels; from this information we can conclude that the extra electron on the Fe^{2+} site, in the insulating region, comes from the Mo ion. This last conclusion goes in the direction of a valence transition driven MIT; nevertheless contrary to the model of Kobayashi et al. [38], the W ion does not have any role in this process. In these scenario, the MIT results from the localization on the iron site of a Mo 5d electron.

6.7 EXAFS

Up to three absorption spectra were collected for each sample and then interpolated (because the energy mesh is always different from one spectra to the other) and averaged using the FORTRAN programs described in chapter three. The signal to noise ratio resulted excellent for all the samples, with the exception of low molybdenum concentrations ($x = 0.15, 0.05$) at Mo K-edge, which had to be recorded in fluorescence mode using a 13-element Ge solid-state detector.

The high quality of the spectra can be noted by eye from figure 6.8, which also reports the fit curves and their transformation in the real space (R). Such an high quality permitted to push the k-range up to 19 AA^{-1} reaching a theoretical spatial resolution of:

$$\delta R \approx \frac{\pi}{2k_{max}} \cdot 0.2 \simeq 0.025\mathring{A}$$

The procedure described in chapter three have been followed to extract the EXAFS signal and fit the data. The atomic cluster have been created using the ATOMS code [66] and the crystallographic structures reported in 6.2. The energy shift, ΔE, and the many body loss factor, S_0^2, have been kept

fixed to values that have been optimized through a first shell analysis. The coordination numbers have also been kept fixed, since there was no reason to suppose discrepancies from their crystallographic values. In the final, the only parameters that have been let free to vary in the fitting procedure were the bond distances (R) and the Debye-Waller factors (σ^2). Considering the links imposed on the third shell paths, the maximum number of free parameters where limited to ten (the number of independent points being around 40). Moreover, correlation between parameters is further reduced because the parameters that we have let free are poorly correlated. Errors on the parameters are calculated using the MINOS subroutine from the MINUIT package as described in chapter three.

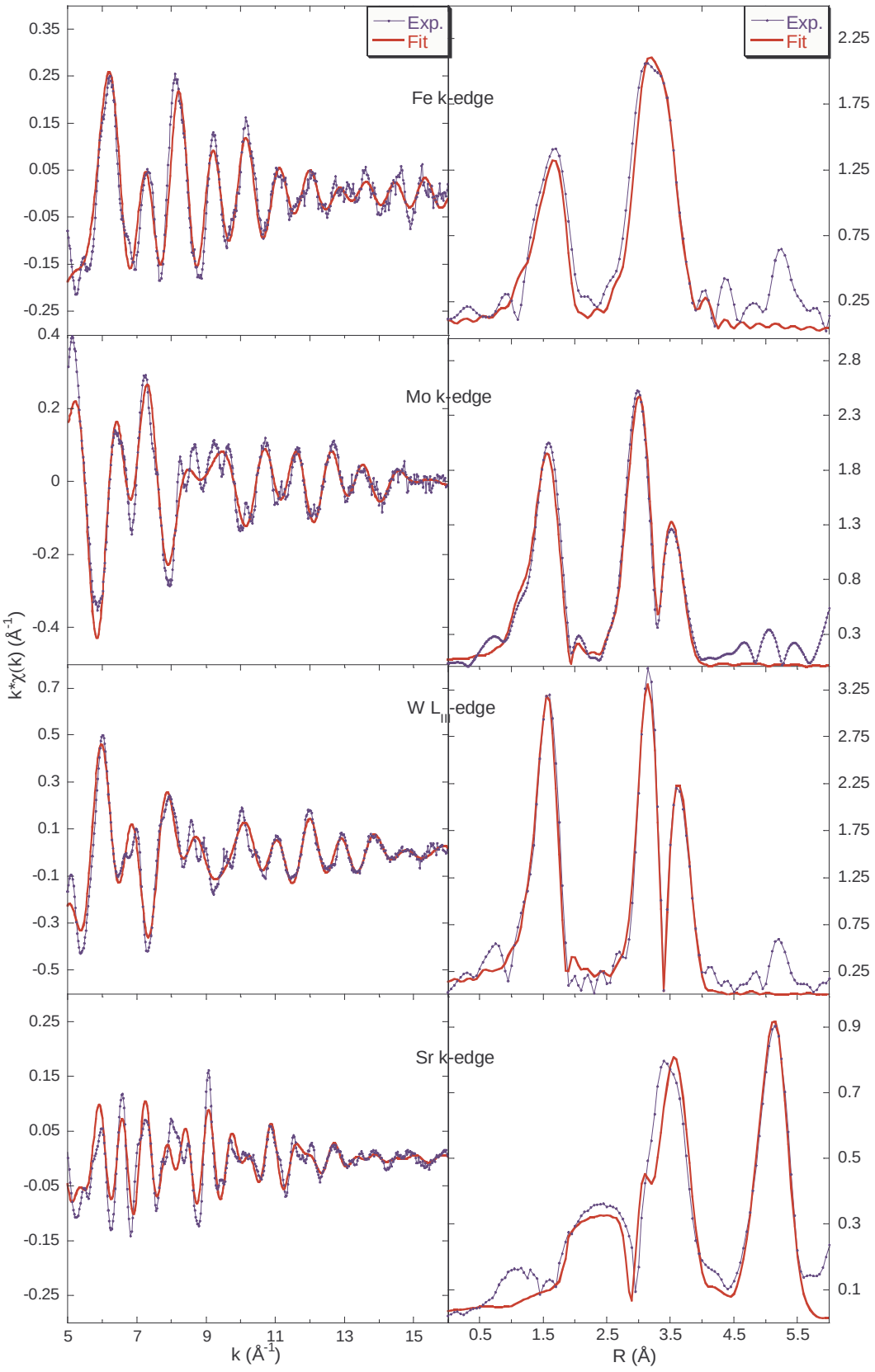

Figure 6.8: Left panels: EXAFS signal (solid line+points) of the $x = 0.3$ sample at different edges and fit curves (solid lines). Right panel: Fourier transforms of the EXAFS signal and of the fit curves.

6.7.1 Fe, Mo and W edges

Five contributes were necessary to obtain good fits. Since similar paths were used to fit spectra at the Fe, Mo and W edges (i.e. the B=Fe and B' =Mo/W sites of the $Sr_2BB'O_6$ double perovskite cell, fig. 6.9), they will be discussed together. In the following we will refer to the equivalent site ions, Mo and W, using the letter B'. The contributes used to fit the data are listed below:

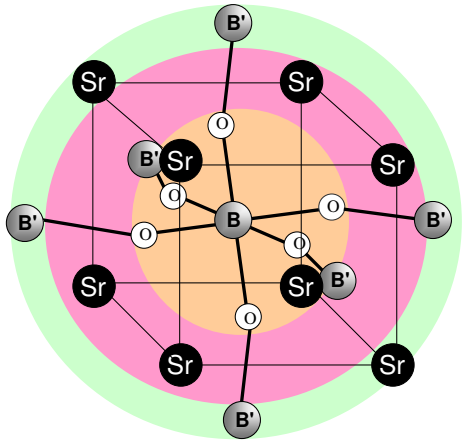

Figure 6.9: Atomic cluster centered on the B site and extending up to the third shell. In the case, instead, the central atom is B' the third shell ions must be replaced with B ions (Fe).

The first contribution (the first shell) originates from the six-fold degenerate Fe/B'-O single scattering paths (fig. 6.10) and represents the main contribution to the EXAFS signal. The crystallographic value is $a/2\sqrt{2}$, where a is the lattice parameter (fig. 6.9). The Fe and B' absorber atoms have six oxygen as nearest neighbor in octahedral configuration in the typical perovskite cell fashion.

A second contribution (second coordination shell) contains the eight-fold degenerate Fe/B'-Sr path (fig. 6.11). The crystallographic value is $\sqrt[3]{a/2}$.

A third contribution includes the six-fold degenerate Fe/B'-B'/Fe bond lengths, (i.e. the lattice parameter a). For intermediate compounds the situation is

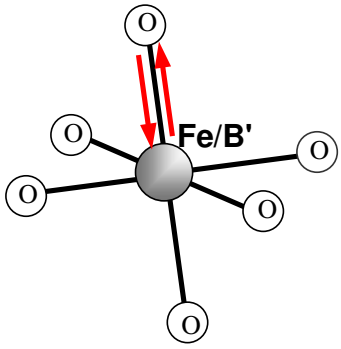

Figure 6.10: First coordination shell. The arrow indicates the one of the six degenerate photoelectron paths

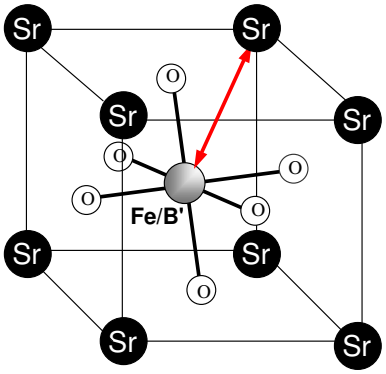

Figure 6.11: First and second coordination shells. The arrow indicate one of the eight degenerate photoelectron paths.

complicated by the simultaneous presence of Mo and W atoms on the B' sites in different concentrations. Since W is substitutional to Mo, when the absorber is Fe, the back-scatterer can be either Mo or W (while if the absorber is Mo or W the back-scatterer is always Fe). Therefore, to correctly fit intermediate compounds at the Fe K-edge, we have introduced both contributes (Fe-Mo and Fe-W) weighting them in the following way:

$$x \cdot R(\text{Fe-Mo}) + (1 - x) \cdot R(\text{Fe-W})$$

where x was kept fixed to the nominal concentrations values. Additional

contributions are due to the two multiple scattering superimposed to the (Fe/B')-(B'/Fe) single scattering paths; their inclusion in the fit is necessary to obtain good fits. These are the (B'/Fe)-(Fe/B')-O-(B'/Fe) three body (3b) and the B'-(Fe/B')-O-(B'/Fe)-O-(B'/Fe) four body (4b) paths reported in fig. 6.12. Since the bond lengths of the single and multiple scattering contributions are not independent, we have introduced some links to reduce the free parameters. These are:

$$R(3b) = R(2b) + \delta$$

$$R(4b) = R(2b) + 2\delta$$

where 2b, 3b and 4b stands for the Fe/B'-O single scattering path and the three and four body multiple scattering paths, respectively. δ is related to the bond angle of the 3b path by the law:

$$\delta \sim \frac{R(3b)}{2}\left(\frac{1}{\cos\theta} - 1\right)$$

Therefore, we may deduce the Fe/B'-O-B'/Fe bond angle from the value of δ.

6.7.2 Sr edge

The Sr K-edge is treated separately since, contrary to the Mo, Fe and W ions, which are placed on the vertexes of the pseudocubic cell, the Sr ion is placed in the center (fig. 6.13). Therefore, it "sees" a different surrounding, which reflects in different paths for the photoelectron.

The EXAFS signal has been fitted up to 6 Å in order to include the very strong signal coming from the long Sr-Sr single scattering path (fig. 6.8) corresponding to the lattice parameters a and b in the tetragonal and monoclinic cell (if $a \neq b$, EXAFS "sees" an average value).

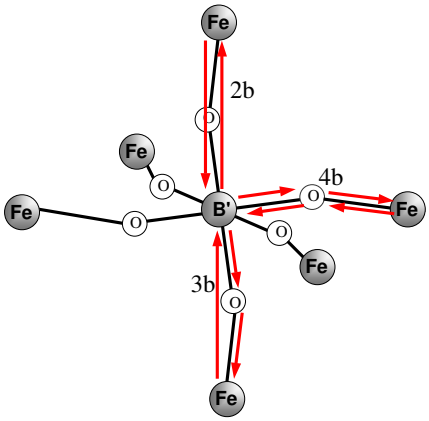

Figure 6.12: First and third coordination shells. The arrows indicate the six-fold degenerate photoelectron single scattering (1b) paths and the 12-fold (2b) and 6-fold (3b) degenerate multiple scattering paths.

The first shell (fig. 6.14) is composed of 12 oxygen nearest neighbor. The Sr-O bond distances are splitted in three groups in the tetragonal symmetry, while Sr-O bond distances are all different in the monoclinic one.

The second shell (fig. 6.14) contains the eight-fold degenerate paths having Fe, Mo and W ions as back-scatterer. The average bond length of this shell is $a/\sqrt{3}$. For intermediate compounds the situation is complicated by the simultaneous occurrence of Fe, Mo and W on the vertexes of the pseudocubic cell. Following the same considerations made for the third shell of the Fe, Mo and W edges, we have chosen to weight Sr-Fe, Sr-Mo and Sr-W paths accordingly to the nominal concentrations.

The third shell contains the six-fold degenerate Sr-Sr single scattering path ($a/\sqrt{2}$) and the fourth shell the longer Sr-Sr path (fig. 6.15), which has a very strong signal and is interesting since it is a direct measure of the lattice parameter a. Therefore, this last value can be directly compared with the diffraction values without any averaging.

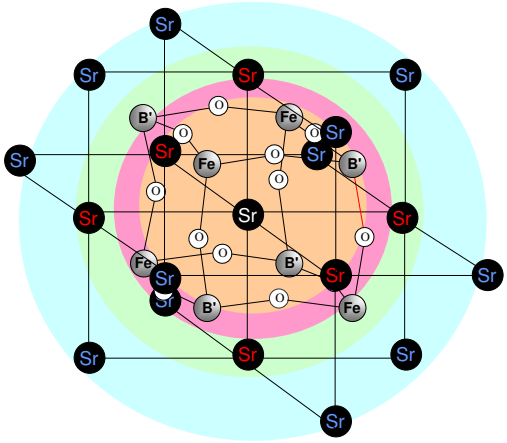

Figure 6.13: Atomic cluster centered on the Sr atom and extending up to the fourth shell.

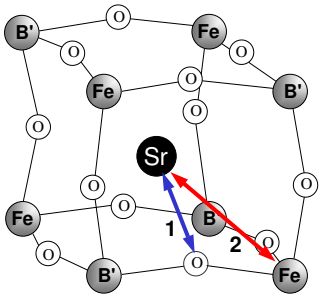

Figure 6.14: First and second coordination shells. The arrows indicate one of the 12-fold degenerate photoelectron first shell paths and a selected 8-fold degenerate second shell paths

6.8 EXAFS results

Tables 6.2-6.4 report the structural parameters (bond distances, R and Debye-Waller factors, σ^2) of the first three coordination shells at the Fe, Mo and W edges as a function of the Mo concentration (i.e. the value of x in $Sr_2FeMo_xW_{1-x}O_6$). Table 6.5 reports the same values for the first four coordination shells at the Sr edge.

It is evident that the local structure around iron undergoes a large (up to

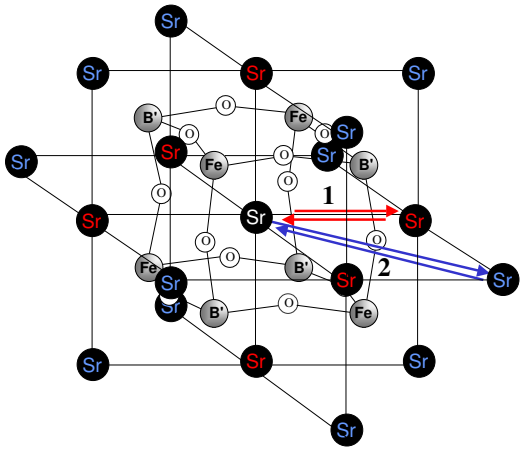

Figure 6.15: Representation of the first four coordination shells in the case of Sr absorber. 12-fold and 6-fold degenerate selected photoelectron paths are labeled 1 and 2 for the third and four shell respectively.

0.1 Å) and abrupt rearrangement crossing the critical concentration. This change is particularly relevant in the first shell, which undergoes an expansion of the FeO_6 octahedra. This confirms the Fe being the key ion in these materials. The structural change at the Sr edge can be interpreted as a consequence of the rearrangement occurring at the Fe site; in fact, the first shell bond distances (Sr-O), undergo a contraction of the same amount of the expansion observed in the Fe-O bond distance. Even if our data at the Mo edge below the critical concentration ($x < 0.25$) are less reliable, we can affirm that also the MoO_6 octahedra contract as a consequence of the expansion of the FeO_6 ones. On the other hand, no microstructural rearrangements are detected at the W edge, which values remain the same for all coordination shells even crossing the critical concentration. This result, together with the lack of any changes in the W-edge XANES spectra, definitively rules out any active role of W in determining the structural and transport properties of these materials.

The second shells show the same trend: a rearrangement at the critical concentration at the Fe and Sr edges and no changes at the W edge (no data

are available for the Mo edge shells higher than the first).

The structural rearrangement of the third shell is slightly less pronounced. The two multiple scattering paths (indicated with the notation 3b and 4b in the tables) have longer paths than the single scattering (2b). This is coherent with a rotation of the FeO_6 octahedra of about 15 ± 5 degrees (165^0)). This value is in rough agreement with the angles calculated from diffraction data by Sanchez et al. [73], which are greater ($167-177$); however, contrary to diffraction data, no rearrangement at the critical concentration is detected for the bond angles. If compared with manganites, the value of the angle found is coherent with an insulating phase. This could indicate a less sensitivity of the transport properties on this parameter.

Plots reported in figures 6.16, 6.17 and 6.18 underline the abrupt change in the local structure crossing the critical concentration. On the contrary, neutron diffraction data, superimposed to our data in the plots, show a continuous and smooth evolution as a function of the concentration. This underlines the sensitivity of EXAFS technique to the rearrangements of the microstructure, i.e. of the atomic bonds within the unit cell, which are usually not detected by diffraction.

On the other hand the Debye-Waller (DW) factors, remain almost unchanged crossing the critical concentration for all coordination shells and edges considered. This can be explained by assuming the absence of a large distortion of the octahedra in the insulating phase (as instead occurs in manganite). This is not surprising since none of the ions present in these compounds presents a Jahn-Teller effect.

Fe K-edge					
Path	Fe-O (2b)	Fe-Sr (2b)	Fe-B'(2b)	Fe-B'(3b)	Fe-B'(4b)
Degeneracy	6	8	6	12	6
Shell	1^{st}	2^{nd}	3^{rd}		
			R (Å)		
$x = 1$	2.003(6)	3.411(6)	3.955(8)	3.991(9)	4.03(2)
$x = 0.8$	2.010(5)	3.423(6)	3.953(4)	3.994(4)	4.038(8)
$x = 0.6$	2.021(5)	3.430(8)	3.962(9)	3.987(5)	3.99(2)
$x = 0.3$	2.015(9)	3.418(9)	3.956(8)	3.98(1)	4.00(3)
$x = 0.15$	2.110(9)	3.491(9)	4.05(3)	4.13(2)	4.17(6)
$x = 0.05$	2.084(9)	3.480(8)	4.033(8)	4.07(3)	4.12(2)
$x = 0$	2.089(7)	3.469(8)	4.01(4)	4.05(2)	4.09(4)
			σ^2 (Å^2)		
$x = 1$	0.0073(4)	0.008(2)	0.002(3)	0.004(1)	0.0048(8)
$x = 0.8$	0.0057(8)	0.0089(7)	0.001(2)	0.003(2)	0.0034(8)
$x = 0.6$	0.0059(8)	0.0058(4)	0.003(2)	0.004(1)	0.0047(8)
$x = 0.3$	0.0049(9)	0.0064(7)	0.0012(8)	0.0045(9)	0.0064(9)
$x = 0.15$	0.0058(9)	0.007(1)	0.0019(3)	0.0193(6)	0.0181(9)
$x = 0.05$	0.004(1)	0.0060(7)	0.0018(6)	0.011(5)	0.012(3)
$x = 0$	0.003(2)	0.0069(8)	0.0013(9)	0.013(1)	0.014(1)

Table 6.2: The table reports the first three coordination shell bond distances, R(Å), and Debye-Waller factors, σ^2(Å^2), at the Fe K-edge as a function of the Mo concentration x. Samples in the HMFM region ($x > 0.25$) are separated by a white space from the insulating ones ($x < 0.25$). 2b, 3b and 4b indicate the two body (single scattering) and the three and four bodies (multiple scattering) paths sketched in figure 6.9. The numbers inside brackets indicate the error on the last digit.

Mo K-edge					
Path	Mo-O (2b)	Mo-Sr (2b)	Mo-Fe(2b)	Mo-Fe(3b)	Mo-Fe(4b)
Degeneracy	6	8	6	12	6
Shell	1^{st}	2^{nd}	3^{rd}		
			R (Å)		
$x = 1$	1.937(7)	3.427(8)	3.95(2)	3.99(1)	4.03(2)
$x = 0.8$	1.944(9)	3.426(9)	3.96(2)	3.99(2)	4.03(4)
$x = 0.6$	1.944(7)	3.410(7)	3.97(2)	3.99(1)	4.03(3)
$x = 0.3$	1.949(7)	3.415(8)	3.98(4)	4.01(2)	4.04(4)
$x = 0.15$	1.91(3)	-	-	-	-
$x = 0.15$	1.90(4)	-	-	-	-
			σ^2 (Å^2)		
$x = 1$	0.0032(9)	0.0050(6)	0.002(2)	0.006(2)	0.012(4)
$x = 0.8$	0.0036(9)	0.0053(9)	0.002(2)	0.005(3)	0.010(4)
$x = 0.6$	0.0025(8)	0.0041(6)	0.002(1)	0.006(2)	0.012(4)
$x = 0.3$	0.0025(9)	0.0045(6)	0.004(2)	0.008(4)	0.013(4)
$x = 0.15$	0.003(2)	-	-	-	-
$x = 0.15$	0.004(3)	-	-	-	-

Table 6.3: The table reports the first three coordination shell bond distances, R (Å), and Debye-Waller factors, σ^2(Å^2), at the Fe K-edge as a function of the Mo concentration x. Low quality of lower Mo concentrations spectra ($x = 0.15$ and $x = 0.05$) prevented a multiple-shell refinement for these samples. Samples in the HMFM region ($x > 0.25$) are separated by a white space from the insulating ones ($x < 0.25$). 2b, 3b and 4b indicate the two body (single scattering) and the three and four bodies (multiple scattering) paths sketched in figure 6.9. The numbers inside brackets indicate the error on the last digit. Since we are at the Mo edge, the lowest Mo concentration sample ($x = 0$) cannot exist.

W L_{III}-edge					
Path	W-O (2b)	W-Sr (2b)	W-Fe(2b)	W-Fe(3b)	W-Fe(4b)
Degeneracy	6	8	6	12	6
Shell	1^{st}	2^{nd}		3^{rd}	
			R (Å)		
$x = 0.8$	1.903(4)	3.443(4)	3.95(3)	3.97(2)	3.99(4)
$x = 0.6$	1.903(3)	3.437(5)	3.94(5)	3.96(3)	4.01(5)
$x = 0.3$	1.906(5)	3.437(4)	3.95(3)	3.97(2)	3.99(3)
$x = 0.15$	1.905(6)	3.447(8)	3.96(5)	3.95(4)	4.03(5)
$x = 0.05$	1.894(7)	3.428(9)	3.95(4)	3.97(3)	4.00(6)
$x = 0$	1.902(5)	3.439(9)	3.946(9)	3.98(4)	4.02(4)
			σ^2 (Å^2)		
$x = 0.8$	0.0026(9)	0.0043(6)	0.005(4)	0.005(1)	0.011(9)
$x = 0.6$	0.0025(8)	0.0041(6)	0.002(1)	0.006(2)	0.012(4)
$x = 0.3$	0.0024(5)	0.0039(3)	0.005(4)	0.0047(9)	0.012(4)
$x = 0.15$	0.0027(9)	0.0065(8)	0.004(1)	0.005(2)	0.008(6)
$x = 0.05$	0.0034(9)	0.0073(8)	0.009(4)	0.007(2)	0.019(7)
$x = 0$	0.0027(6)	0.0067(6)	0.006(5)	0.0051(9)	0.009(3)

Table 6.4: The table reports the first three coordination shell bond distances, R (Å), and Debye-Waller factors, σ^2(Å^2), at the W L_{III} K-edge as a function of the Mo concentration x. Samples in the HMFM region ($x > 0.25$) are separated by a white space from the insulating ones ($x < 0.25$). 2b, 3b and 4b indicate the two body (single scattering) and the three and four bodies (multiple scattering) paths sketched in figure 6.9. The numbers inside brackets indicate the error on the last digit. Since we are at the W edge, the highest Mo concentration sample ($x = 1$) cannot exist.

Sr K-edge				
Path	Sr-O (2b)	Sr-Fe/B'(2b)	Sr-Sr (2b)	Sr-Sr(2)(2b)
Degeneracy	12	8	6	12
Shell	1^{st}	2^{nd}	3^{rd}	4^{th}
		R (Å)		
$x = 1$	2.69(4)	3.44(2)	3.94(2)	5.57(2)
$x = 0.8$	2.71(4)	3.42(2)	3.95(2)	5.58(2)
$x = 0.6$	2.71(5)	3.37(2)	3.94(1)	5.57(2)
$x = 0.3$	2.72(5)	3.36(2)	3.94(2)	5.56(2)
$x = 0.15$	2.60(6)	3.44(6)	4.01(7)	5.62(6)
$x = 0.05$	2.64(5)	3.45(5)	3.99(5)	5.65(5)
$x = 0$	2.63(4)	3.46(1)	4.00(2)	5.67(4)
		σ^2 (Å^2)		
$x = 1$	0.024(7)	0.003(1)	0.008(2)	0.009(2)
$x = 0.8$	0.027(9)	0.005(2)	0.009(2)	0.010(3)
$x = 0.6$	0.036(2)	0.004(2)	0.007(1)	0.008(2)
$x = 0.3$	0.036(1)	0.005(2)	0.007(2)	0.009(2)
$x = 0.15$	0.034(7)	0.0066(7)	0.005(2)	0.010(6)
$x = 0.05$	0.024(2)	0.0056(7)	0.015(9)	0.018(2)
$x = 0$	0.026(9)	0.006(1)	0.006(2)	0.015(4)

Table 6.5: The table reports the first four coordination shell bond distances, R (Å), and Debye-Waller factors, σ^2(Å^2), at the Sr K-edge as a function of the Mo concentration x. Samples in the HMFM region ($x > 0.25$) are separated by a white space from the insulating ones ($x < 0.25$). 2b indicates the two body (single scattering) paths. The numbers inside brackets indicate the error on the last digit.

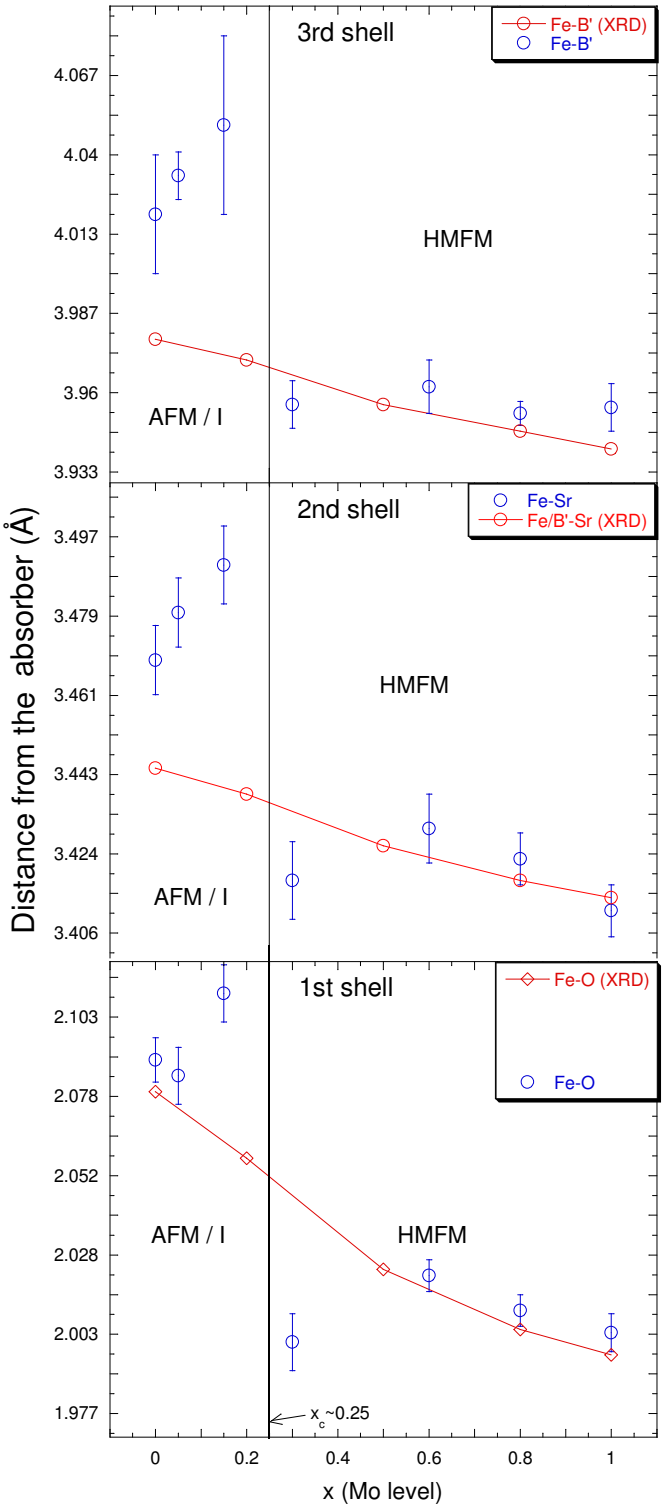

Figure 6.16: The plots show the trend of the average bond distances (reported in tables 6.2) of the first, second and third coordination shells extracted of the EXAFS data at the Fe edges. NPD calculated bond distances from Sanchez are also reported and have been averaged for comparison with EXAFS data. It is evident the structural rearrangement occurring at the crossover between the Half metallic ferromagnetic phase (HMFM) and the Insulating phase (I). The overall behavior is a lengthen of the Fe-X bonds in the insulating phase with respect to the HMFM region, where X indicates the back scatterer O, Sr and W/Mo (B') for the first, second and third shell, respectively. It can also be noted the smooth evolution of the diffraction data compared to the abrupt changes of the EXAFS ones at the critical concentration. For clarity, only single scattering distances are reported for the 3rd shell.

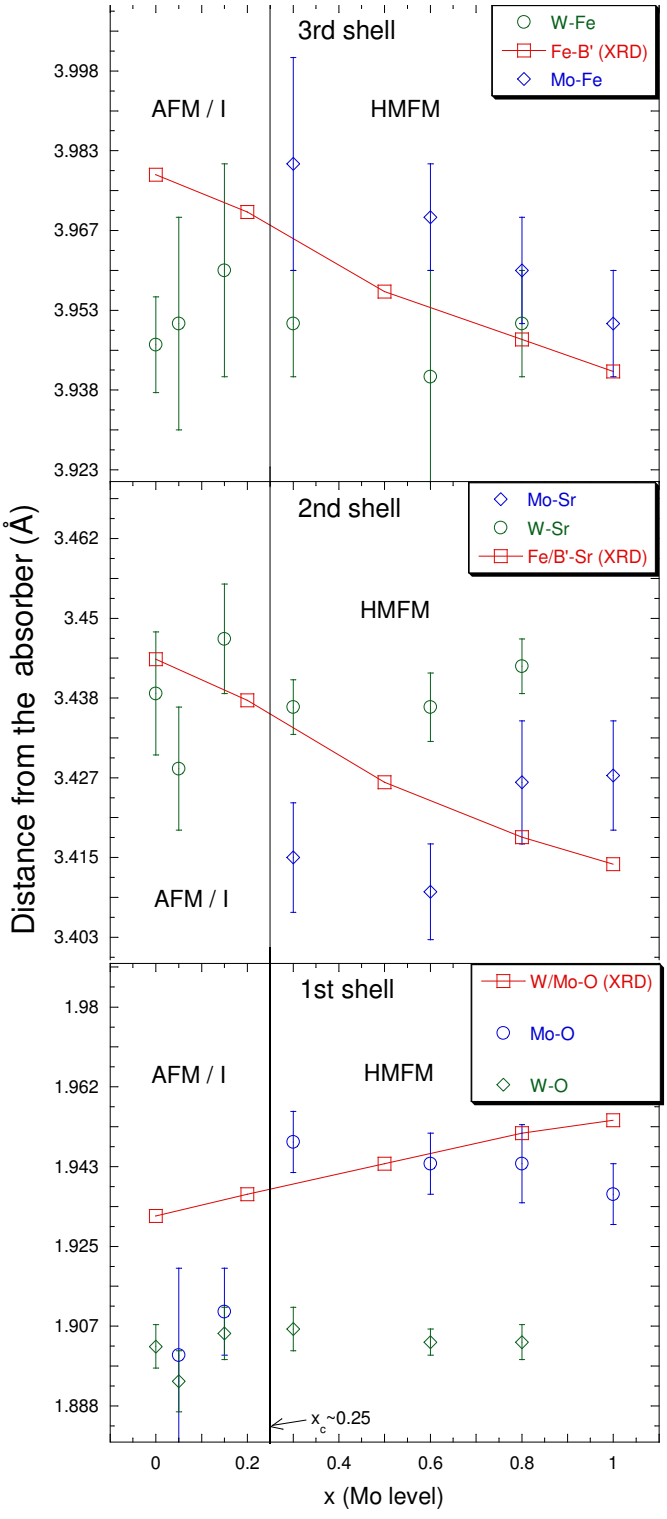

Figure 6.17: The graphs show the trend of the average bond distances (reported in tables 6.3 and 6.4) of the first, second and third coordination shells extracted of the EXAFS data at the Mo and W edges. NPD calculated bond distances from Sanchez are also reported and have been averaged for comparison with EXAFS data. It is evident the structural rearrangement occurring at the crossover between the Half metallic ferromagnetic phase (HMFM) and the Insulating phase (I). The Mo-O bonds show a contraction trend probably as a consequence of the expansion of the FeO_6 octahedra. Due to the low signal, information are available for higher shell Mo bonds in the insulating phase. W bonds remain almost unchanged (within the experimental errors) in all the coordination shells. It can be noted the smooth evolution of the diffraction data opposite to the abrupt changes of the EXAFS ones at the critical concentration. For clarity, only single scattering distances are reported for the 3rd shell.

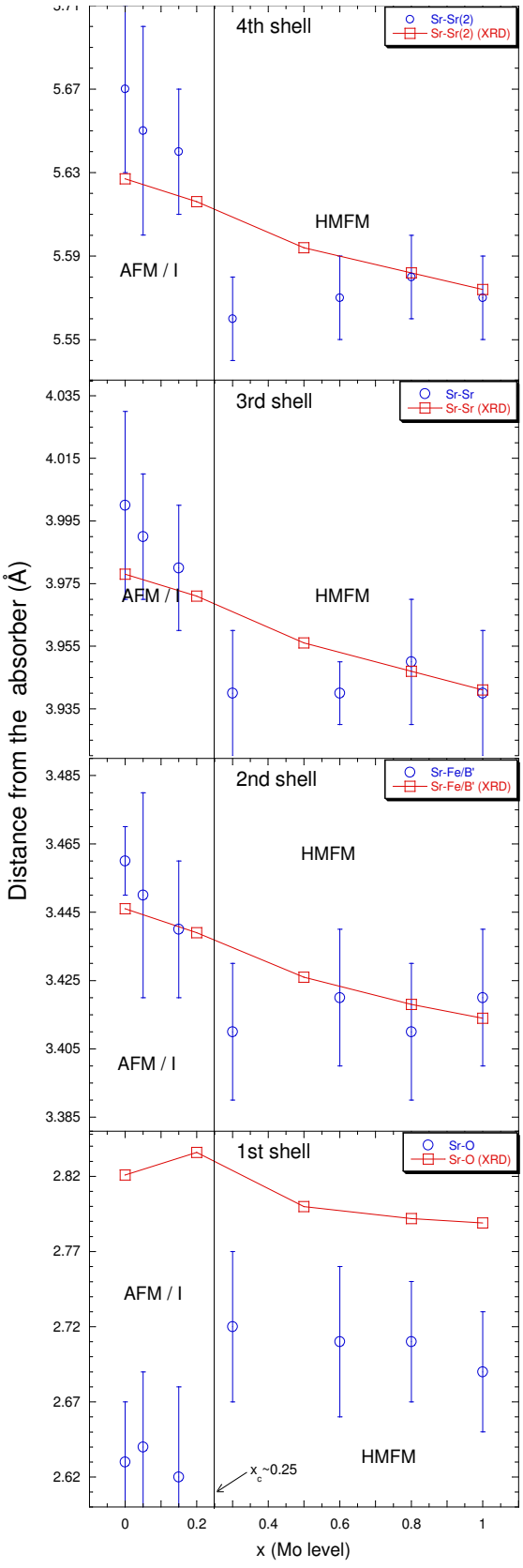

Figure 6.18: The plots show the trend of the average bond distances (reported in table 6.5) of the first, second, third and fourth coordination shells extracted from the EXAFS data at the Sr edge. The symbol B' indicates the Mo and W equivalent sites ions. NPD calculated bond distances from Sanchez are also reported and have been averaged for comparison with EXAFS data. As for the data shown in figures 6.16 and 6.17, it is evident the structural rearrangement occurring at the crossover between the HMFM and the insulating phase (I). The first shell bond distances, Sr-O, exhibit an abrupt decrease crossing the critical concentration x_c. This is a consequence of the expansion of the FeO_6 octahedra observed and reported in fig. 6.16. Diffraction data follow a different behavior and results shifted toward higher values. This could be ascribed to the higher sensitivity of the EXAFS to closer distances. Since the first coordination shell has a large splitting, longer and shorter distances could have opposite behaviors. For higher shells the overall behavior is a lengthen of the bond distances in the insulating phase with respect to the HMFM region. In particular, the fourth shell path, Sr-Sr(2) (fig. 5.12), which represents the average lattice parameter, follows the same trend, confirming an overall cell expansion in the insulating region. It is worth to note the smooth evolution of the diffraction data opposite to the abrupt changes of the EXAFS ones at the critical concentration.

6.9 Discussion

From the values reported in the tables and evidenced in the graphs of figure 6.16, 6.17 and 6.18, it can immediately be noted that a large change in the local structure occurs at the critical concentration ($x_c \sim 0.25$), that is, at the crossover between the half metallic ferromagnetic phase (HMFM) and the antiferromagnetic insulating phase (AFM-I). In strict accordance with XANES results, EXAFS data show that the local atomic structure remains that of one end compound up to the critical concentration, where the structure local rearranges to that of the other end compound. Our results are in agreement with the assumption, largely supported by the literature, that the Fe^{2+} W^{6+} configuration (localized charges) replaces the mixed valence configuration having $Fe^{2.5+}$ (itinerant charges), when the W content is risen above the critical concentration. Since the ionic radius of Fe^{2+} (0.78 Å in six-fold configuration) is significantly larger than that of the high spin Fe^{3+} cation (0.645 Å) an expansion of the cell, as observed from NPD measurement by Sanchez et al. [73] is expected. On the other hand, ionic radii of Mo^{5+} and W^{6+} are very similar (0.61 and 0.6 Å respectively) so that the substitution of W in place of Mo should not directly influence the structure. In other words, is the progressive localization of the carriers that induces a rearrangement of the local structure at the critical concentration.
Nevertheless, our data evidence that this rearrangement is *abrupt*, in contrast with NPD data by Sanchez et al. who observe a smooth and continuous evolution of the volume cell and lattice parameters as a function of the Mo concentration. Summarizing, the main results of this extensive XAFS analysis are:

- At a local scale (up to 10 Å) the rearrangement of the structure crossing the critical concentration occurs abruptly. This is in accordance to information obtained by our semi-quantitative XANES analysis.

- The main modification in the local structure occurs at Fe sites where the Fe-O bonds elongate of about 0.1 Å. The other changes in the structure can be interpreted as a rearrangement of the lattice in response to the expansion of the FeO_6 octahedra.

- Debye-Waller factors do not follow the modification observed for bond distances at any of the coordination shell or edge investigated.

6.10 Conclusions

We have observed modifications in the structural and electronic properties of $Sr_2FeMo_xW_{1-x}O_6$, which are closely related to the metal/insulator transition. At the transition, charges localize at the Fe site and induce a local structural order similar to that of Sr_2FeWO_6 ; on the other hand, in the metallic phase delocalized charges promote an atomic structure similar to that of Sr_2FeMoO_6 . Nevertheless, the observed structural changes are not proportional to the W doping. Therefore, they do not support the phase separation scenario, which implies the growth of insulating W-rich clusters proportionally to x. On the other hand, the W local structure and electronic properties do not change in the whole concentration range ($0 \leq x \leq 1$) in contrast with the valence transition model, which predicts a modification of its valence state ($W^{6+} \longrightarrow W^{5+}$). The absence of any abrupt change across x_c indicates that the W ions do not play any role in the MIT and, in particular, do not contribute to the electronic conduction. According to our results in the W-rich insulating samples, the charges are localized. As the Mo concentration exceeds the x_c threshold, charge localized on the Fe^{2+} sites, delocalize giving rise to the metallic regime. In this region even a weak excess of delocalized charges (less than 0.5 electron per Fe ion in $x = 0.3$ sample) is enough to provoke the rearrangement of the local atomic structure of the sample, which becomes equal to that of ferromagnetic metallic Sr_2FeMoO_6 .

Finally, XANES spectra indicate a partial localization of the charge carriers on the Mo sites in the half-metallic phase. These spectra also show that, in the insulating phase, these charges are transferred on the Fe ion, inducing a change of the valence states of both Mo and Fe.

General conclusions

In this work I investigated the local structure of Na doped manganite thin films as a function of the film thickness and of W doped double-perovskite bulk samples as a function of the doping level. Furthermore, I developed and characterized a total electron yield (TEY) detector.

Results on manganites thin films evidenced the evolution of the local structure as a function of the thickness of the films. In particular, they confirmed that the change in the transport properties of the thinnest film (50 Å), which remains insulating at all temperatures, cannot be directly attributed to the lattice mismatch with the substrate. In fact, the change in the local structure around the Mn ion with respect to bulk values, results almost one order of magnitude larger than strain induced by the lattice mismatch. Experimental results lead to the conclusion that, in the thinnest film, the long component of the JT distortion stabilizes in the plane of the film, favored by the expansion of the lattice induced by the lattice mismatch.

Our data are in agreement with the hypothesis that the structure of thinnest film is completely dead-layer like and hence insulating. Increasing the thickness, the structure of the films relaxes becoming similar to the bulk material.

The extensive study on the local structure of the double perovskite W doped series included complemental structural information on all the absorption edge of the metallic elements in the compounds. This study depicts the microstructural counterpart of the metal-to-insulator transition (MIT), occurring as a function of the doping level, which is associated to a magnetic

transition.

XANES and EXAFS data confirms that the transition is driven by the localization of the charge carriers on the iron site, which induce a large change in the local structure due to the very different ionic radius between Fe^{2+} and Fe^{3+}.

Moreover, contrary to previous XRD structural characterizations, the transition appears sharp: in each phase (the half-metallic/ferromagnetic and the antiferromagnetic/insulating) intermediate compounds maintain the very same local structure of the end compounds up to the critical concentration.

Further, these data suggest that the W ion does not have any role in the MIT, its structure and valence state remaining the same in the whole concentration range.

Finally, XANES spectra indicate a partial localization of the charge carriers on the Mo sites in the half-metallic phase. These spectra also show that, in the insulating phase, these charges are transferred on the Fe ion, inducing the change of the valence states of both Mo and Fe.

Test runs performed with the new TEY detector demonstrate its usefulness in obtaining structural information on thin films grown on a crystalline substrate.

Furthermore, comparative transmission measurements demonstrate the reliability of the data acquired and the ability of this equipment to work in a wide range temperatures and/or gas pressures. Nevertheless, more work is required to improve and characterize the detector.

[16] [6] [12] [17] [27] [26] [25] [43] [50] [71] [70] [65] [31]

Bibliography

[1] *http://seal. web. cern. ch/seal/workpackages/mathlibs/minuit/home. html.*

[2] P. Anderson and H. Hasegawa. *Phys. Rev.*, 100:675, 1955.

[3] A. L. Ankudinov, B. Ravel, J. J. Rehr, and S. D. Conradson. *Phys. Rev. B*, 7565:58, 1998.

[4] L. V. Azarov. *Rev. Mod. Phys.*, 35:1012, 1963.

[5] M. Benfatto, Y. Joly, and C. R. Natoli. *Phys. Rev. Lett.*, 82:2398, 1999.

[6] M. Benfatto, Y. Joly, and Calogero R. Natoli. *Phys. Rev. Lett.*, 83:636, 1999.

[7] M. Bibes, Ll. Balcells, S. Valencia, J. Fontcuberta, M. Wojcik, E. Jedrika, and S. Nadolski. *Phys. Rev. Lett.*, 87:067210, 2001.

[8] M. Bibes, Ll. Balcells, S. Valencia, B. Martinez, M. J. Casanove, J. C. Ousset, and J. Fontcuberta. *Appl. Sur. Sci.*, 188:202, 2002.

[9] M. Bibes, S. Valencia, Ll. Balcells, B. Martinez, J. Fontcuberta, M. Wojcik, S. Nadolski, and E. Jedrika. *Phys. Rev. B*, 66:134416, 2002.

[10] A. Biswas, M. Rajeswari, R. C. Srivastava, Y. H. Li, T. Venkatesan, R. L. Greene, and A. J. Millis. *Phys. Rev. B*, 61:9665, 2000.

[11] R. P. Borges, W. Guichard, J. G. Lunney, J. M. D. Coey, and F. Ott. *J. Appl. Phys.*, 89:3868, 2001.

[12] F. Bridges, C. H. Booth, M. Anderson, G. H. Kwei, J. J. Neumeier, J. Snyder, J. Mitchell, J. S. Gardner, and E. Brosha. *Phys. Rev. B*, 63:214405, 2001.

[13] F. Bridges, C. H. Booth, M. Anderson, G. H. Kwei, J. J. Neumeier, J. Snyder, J. Mithcell, J. S. Gardner, and E. Brosha. *Phys. Rev. B*, 63:214405, 2001.

[14] A. Chattopadhyay and A. Millis. *cond-mat/0006208*, 2000.

[15] O. Chmaissem, R. Kruk, B. Dabrowski, D. E. Brown, X. Xiong, S. Kolesnik, and J. D. Jorgensen. *Phys. Rev. B*, 62:14197, 2000.

[16] E. Dagotto. *New Journal of Phisics*, 7:010067, 2005.

[17] R. I. Dass and J. B. Goodenough. *Phys. Rev. B*, 63:064417, 2001.

[18] P. de Gennes. *Phys. Rev.*, 118:141, 1960.

[19] R. de Kronig. *Z. Phys.* , 70:317, 1931.

[20] Z. W. Dong, R. Ramesh, T. Venkatesan, M. Johnson, Z. Y. Chen, S. P. Pai, V. Talyansky, R. P. Sharma, R. Shreekala, C. J. Lobb, and R. L. Greene. *Appl. Phys. Lett.*, 71:1718, 1997.

[21] A. P. Douvalis, M. Venkatesan, J. M. D. Coey, M. Grafoute, J-M. Greneche, and R. Sryanaraynan. *J. of Phys. Cond. Mat.*, 14:12611, 2002.

[22] I. S. Elvimov, V. I. Anisimov, and G. A. Sawatzky. *Phys. Rev. Lett.*, 82:4264, 1999.

[23] A. Erbil, G. S. Cargill, R. Frahm, and R. F. Boehme. *Phys. Rev. B*, 37:2450, 1988.

[24] H. Q. Yin et al. *J. Appl. Phys.*, 87:6761, 2000.

[25] Joaquin Garcia, M. Concepcion Sanchez, Gloria Subias, and Javier Blasco. *J. of Phys. Cond. Mat.*, 13:3229–3241, 2001.

[26] M. Garcia-Hernandez, J. L. Martinez, M. J. Martinez-Lope, M. T. Casais, and J. A. Alonso. *Phys. Rev. Lett.*, 86:2443, 2001.

[27] B. Garcia-Landa, C. Ritter, M. R. Ibarra, J. Blasco, P. A. Algarabel, R. Mahendiran, and J. Garcia. *Solid State Commun.*, 110:435–438, 1999.

[28] P. Ghigna, A. Marzola, R. Amantea, L. Malavasi, G. Flor, F. D'Acapito, F. Bardelli, and M. C. Mozzati. *Nucl. Instr. Meth. Phys. Res. B*, 238:242, 2005.

[29] J. B. Goodenough. *Phys. Rev.*, 100:564, 1955.

[30] T. Holstein. *Ann. Phys.* , 343:8, 1959.

[31] A. Yu. Ignatov, N. Ali, and S. Khalid. *Phys. Rev. B*, 64:014413, 2001.

[32] M. H. Jo, N. D. Mathur, N. K. Todd, and N. G. Blamir. *Phys. Rev. B*, 61:R14905, 2000.

[33] G. Jonker and J. van Santen. *Physica*, 16:599, 1950.

[34] T. Kasuya and A. Yanase. *Rev. Mod. Phys.*, 40:684, 1968.

[35] H. Kawanaka, I. Hase, S. Toyama, and Y. Nishira. *Physica B*, 281+282:518, 2000.

[36] M. Kawasaki, K. Takahashi, T. Maeda, R. Tschiya, M. Shinohara, O. Ishiyama, T. Yonezawa, M. Yoshimoto, and H. Koinuma. *Science*, 266:1540, 1994.

[37] T. Kimura, H. Sawada, and K. Terakura. *Nature*, 395:677, 1998.

[38] K. I. Kobayashi, T. Okuda, Y. Tomioka, T. Kimura, and Y. Tokura. *J. Magn. Magn. Mater.*, 218:17, 2000.

[39] K. Kubo and N. Ohata. *J. Phys. Soc. Jpn.* , 33:21, 1972.

[40] A. Lanzara, N. L. Saini, M. Brunelli, F. Natali, A. Bianconi, P. G. Radaelli, and S. W. Cheong. *Phys. Rev. Lett.*, 81:878, 1998.

[41] P. A. Lee, P. H. Citrin, P. Eisenbergher, and B. M. Kincaid. *Rev. Mod. Phys.*, 53:769, 1981.

[42] J. Linden, T. Yamamoto, M. Karppinen, H. Yamauchi, and T. Pietari. *Appl. Phys. Lett.*, 76:2925, 2000.

[43] J. Linden, T. Yamamoto, J. Nakamura, H. Yamauchi, and M. Karppinen. *Phys. Rev. B*, 66:184408, 2002.

[44] Y. Lu, W. Li, C. Q. Gong, G. Xiao, A. Gupta, P. Lecouer, J. Z. Sun, Y. Y. Wan, and V. P. Dravid. *Phys. Rev. B*, 54:R8357, 1996.

[45] L. Malavasi and G. Flor. *J. Phys. Chem. B*, 107, 2003.

[46] L. Malavasi, M. C. Mozzati, I. Alessandri, L. E. Depero, C. B. Azzoni, and G. Flor. *J. Phys. Chem. B*, 108:13643, 2004.

[47] L. Malavasi, M. C. Mozzati, P. Ghigna, C. B. Azzoni, and G. Flor. *J. Phys. Chem. B*, 107:2500, 2003.

[48] C. Meneghini, R. Cimino, S. Pascarelli, and S. Mobilio. *Phys. Rev. B*, 56:3520, 1997.

[49] A. Millis, P. Littlewood, and B. I. Shraiman. *Phys. Rev. Lett.*, 74:5144, 1995.

[50] A. J. Millis, B. I. Shraiman, and R. Mueller. *Phys. Rev. Lett.*, 77:175, 1996.

[51] A. Moreo, M. Mayr A. Geiguin S. Yunoki, and E. Dagotto. *Phys. Rev. Lett.*, 84:5568, 2000.

[52] A. Moreo, S. Yunoki, and E. Dagotto. *Science*, 283:2034, 1999.

[53] N. Mott and E. Davis. *Electronic Processes In Non-Crystalline Materials.* Clarendon Press Oxford, 1971.

[54] T. Nagakawa. *J. Phys. Soc. Jpn.*, 27:880, 1969.

[55] T. Nakagawa, K. Yoshikawa, and S. Nomura. *Journ. of Phys. Soc. Jap.* , 27:880, 1969.

[56] S. Nakayama, T. Nagakawa, and S. Nomura. *J. Phys. Soc. Jpn.* , 24:219, 1968.

[57] D. Niebieskikwiat, R. D. Sanchez, A. Caneiro, L. Morales, M. Vasquez-Mansilla, F. Rivadulla, and L. E. Hueso. *Phys. Rev. B*, 62:3340, 2000.

[58] K. R. Nikolayev, A. Yu-Dobin, I. N. Krivorotov, W. K. Cooley, A. Bhattacharya, A. L. Kobrinski, L. I. Glazman, R. M. Wentzovitch, E. D. Dahlberg, and A. M. Goldman. *Phys. Rev. Lett.*, 85:3728, 2000.

[59] A. S. Ogale, R. Ramesh, and T. Venkatesan. *Appl. Phys. Lett.*, 75:537, 1999.

[60] L. G. Parrat, C. F. Hempsted, and E. L. Jossen. *Phys. Rev. B*, 105:1228, 1957.

[61] S. Pascarelli, F. Bosherini, F. D'Acapito, J. Hrdy, C. Meneghini, and S. Mobilio. *J. Synch. Rad.*, 3:147, 1996.

[62] T. Penney, M. Shafter, and J. Torrance. *Phys. Rev. B*, 5:3669, 1972.

[63] R. B. Praus, G. M. Gross, F. S. Razavi, and H. U. Habermeier. *J. Magn. Magn. Mater.*, 211:41, 2000.

[64] W. Prellier, Ch. Simon, A. M. Haghiri-Gosnet, B. Mercey, and B. Raveau. *Phys. Rev. B*, 61:R16337, 2000.

[65] Q. Qian, T. A. Tyson, C. C. Kao, M. Croft, S. W. Cheong, G. Popov, and M. Greenblatt. *Phys. Rev. B*, 64:024430, 2001.

[66] B. Ravel and M. Newville. *J. Synch. Rad.*, 12:537, 2005.

[67] Sugata Ray, Ashwani Kumar, Subham Majumdar, E. V. Sampathkumaran, and D. D. Sarma. *J. of Phys. Cond. Mat.*, 13:607, 2001.

[68] J. J. Rehr and R. C. Albers. *Rev. Mod. Phys.*, 72:621, 1979.

[69] D. Reinen. *Solid State Chem.* , 27:71, 1979.

[70] T. Saha-Dasgupta and D. D. Sarma. *Phys. Rev. B*, 64:064408, 2001.

[71] Myron B. Salomon and Marcelo Jaime. *Rev. Mod. Phys.*, 73:583, 2001.

[72] P. A. Salvador, T. D. Doan, B. Mercey, and B. Raveau. *Chem. Mater*, 10:2592, 1998.

[73] D. Sanchez, J. A. Alonso, M. Garcia-Hernandez, M. J. Nartinez-Lope, and M. T. Casais. *J. of Phys. Cond. Mat.*, 17:3673, 2005.

[74] D. D. Sarma. *Curr. Op. Sol. State Mat. Sc.*, 5:261, 2001.

[75] D. D. Sarma, Priya Mahadevan, T. Saha-Dasgupta, Sugata Ray, and Ashwani Kumar. *Phys. Rev. Lett.*, 85:2549, 2000.

[76] D. D. Sarma, E. V. Sampathkumaran, S. Ray, R. Nagarajan, S. Majumdar, A. Kumar, G. Nalini, and T. N. Guru-Row. *Solid State Commun.*, 114:465, 2000.

[77] D. D. Sarma, E. V. Sampathkumaran, Sugata Ray, R. Nagarajan, Subham Majumdar, Ashawani Kumar, G. Nalini, and T. N. Guru Row. *Solid State Commun.*, 114:465, 2000.

[78] D. D. Sarma, E. V. Sampathkumaran, Sugata Ray, R. Nagarajan, Subham Majumdar, Ashwani Kumar, G. Nalini, and T. N. Guru Row. *Solid State Commun.*, 114:465–468, 2000.

[79] D. E. Sayers, E. A. Stern, and F. W. Lytle. *Phys. Rev. Lett.*, 27:1204, 1971.

[80] H. Scher and R. Zallen. *J. Chem. Phys.*, 53:3759, 1970.

[81] S. L. M. Schroeder. *Total Electron-Yield XAS as an In Situ Probe for Studios of Catalyst and Other Materials in Reactive Gas Environments.* 1996. PhD Thesis.

[82] E. Sevillano, H. Muth, and J. J. Rehr. *Phys. Rev. B*, 28:3520, 1979.

[83] R. D. Shannon. *Acta Crystall. A*, 32:751, 1976.

[84] S. L. M. Shroeder, G. D. Moggridge, R. M. Ormerod, T. Rayment, and R. M. Lambert. *Surf. Sci. Lett.* , 324:L371, 1995.

[85] E. A. Stern. *Phys. Rev. B*, 10:3027, 1974.

[86] J. Z. Sun, D. W. Abraham, R. A. Rao, and C. B. Eom. *Appl. Phys. Lett.*, 74:3017, 1999.

[87] J. Tanaka, M. Umehara, S. Tamura, M. Tsukioka, and S. Ehara. *J. Phys. Soc. Jpn.* , 51:1236, 1982.

[88] Y. Tomioka, A. Asamitsu, Y. Moritomo, H. Kuwahara, and Y. Tokura. *Phys. Rev. B*, 53:1689, 1996.

[89] M. Viret, M. Drouet, J. Nassar, J. P. Contour, and A. Fert. *Europhys. Lett.*, 39:545, 1997.

[90] H. S. Wang, E. Wertz, Y. F. Hu, Q. Li, and D. G. Shlom. *J. Appl. Phys.*, 87:7409, 2000.

[91] E. O. Wollan and W. C. Koehler. *Phys. Rev.*, 100:545, 1955.

[92] H. W. Zandbergen, S. Fresien, T. Nojima, and J. Aarts. *Phys. Rev. B*, 60:10259, 1999.

[93] C. Zener. *Phys. Rev.*, 2:403, 1951.

[94] M. Ziese. *Phys. Rev. B*, 60:R738, 1999.

[95] M. Ziese, H. C. Semmelhack, K. H. Han, S. P. Sena, and H. J. Blythe. *J. Appl. Phys.*, 91:9930, 2002.